Modelling Energetics and Stability of Carbon Nanotubes: A Novel Approach

Dissertation
zur Erlangung des Doktorgrades
der Naturwissenschaften

vorgelegt beim Fachbereich Physik
der Goethe-Universität
in Frankfurt am Main

von
Maneesh Mathew
aus Iritty, Indien

Frankfurt am Main
2009

(D 30)

vom Fachbereich Physik der
Goethe-Universität als Dissertation angenommen.

Dekan: Prof. Dr. Dirk H. Rischke

Gutachter1: Prof. Dr. Andrey V. Solov'yov

Gutachter2: Prof. Dr. Dr. h.c. mult. Walter Greiner

Datum der Disputation: 16 October 2009

To,

My loving parents Mathew and Mary for their never ending love..

My teachers Dr. Devadhasan and C. V. Sandhya for the relentless support..

My dearest friend Leema for the constant inspirations..

My Anns, who believed in me more than I did..

Abstract

This thesis is devoted to the developement of a classical model for the study of the energetics and stability of carbon nanotubes. The motivation behind such a model stems from the fact that production of nanotubes in a well-controlled manner requires a detailed understanding of their energetics. In order to study this different theoretical approaches are possible, ranging from the computationally expensive quantum mechanical first principle methods to the relatively simple classical models. A wisely developed classical model has the advantage that it could be used for systems of any possible size while still producing reasonable results.

The model developed in this thesis is based on the well-known liquid drop model without the volume term and hence we call it liquid surface model. Based on the assumption that the energy of a nanotube can be expressed in terms of its geometrical parameters like surface area, curvature and shape of the edge, liquid surface model is able to predict the binding energy of nanotubes of any chirality once the total energy and the chiral indices of it are known. The model is suggested for open end and capped nanotubes and it is shown that the energy of capped nanotubes is determined by five physical parameters, while for the open end nanotubes three parameters are sufficient. The parameters of the liquid surface model are determined from the calculations performed with the use of empirical Tersoff and Brenner potentials and the accuracy of the model is analysed. It is shown that the liquid surface model can predict the binding energy per atom for capped nanotubes with relative error below 0.3% from that calculated using Brenner potential, corresponding to the absolute energy difference being less than 0.01 eV.

The influence of the catalytic nanoparticle on top of which a nanotube grows, on the nanotube energetics is also discussed. It is demonstrated that the presence of catalytic nanoparticle changes the binding energy per atom in

such a way that if the interaction of a nanotube with the catalytic nanoparticle is weak then attachment of an additional atom to a nanotube is an energetically favourable process, while if the catalytic nanoparticle nanotube interaction is strong , it becomes energetically more favourable for the nanotube to collapse. The suggested model gives important insights in the energetics and stability of nanotubes of different chiralities and is an important step towards the understanding of nanotube growth process.

Young modulus and curvature constant are calculated for single-wall carbon nanotubes from the paremeters of the liquid surface model and demonstrated that the obtained values are in agreement with the values reported earlier both theoretically and experimentally. The calculated Young modulus and the curvature constant were used to conclude about the accuracy of the Tersoff and Brenner potentials. Since the parameters of the liquid surface model are obtained from the Tersoff and Brenner potential calculations, the agreement of elastic properties derived from these parameters corresponds to the fact that both potentials are capable of describing the elastic properties of nanotubes. Finally, the thesis discuss the possible extension of the model to various systems of interest.

Zusammenfassung

Kohlenstoffnanoröhren (englisch *Carbon Nanotubes* kurz CNT), sind zylindrische Kohlenstoffallotrope, deren Durchmesser im Nanometerbereich liegen. Seit ihrer Entdeckung 1991 durch Sumio Iijima (NEC) [1] wurden viele außergewöhnliche Eigenschaften der CNT erforscht, die das Potential besitzen sowohl Technologie als auch Forschung in diesem Gebiet in großem Maße zu revolutionieren. Obwohl ein detailliertes experimentelles Verständnis von Kohlenstoffnanoröhren und ihren Eigenschaften vorhanden ist, konnten keine großen Fortschritte aus theoretischer Sicht erziel werden. Dies führt zu einem der meist diskutierten Probleme im Gebiet der Kohlenstoffnanoröhrenforschung: die kontrollierte Herstellung von Nanoröhren. Trotz großer Bemühungen der Experimentalphysiker Kohlenstoffnanoröhren hoher Qualität zu produzieren, ist das Problem noch ungelöst, da es ein tieferes Verständnis von Kohlenstoffnanoröhren aus einer theoretischen Perspektive voraussetzt.

Um die Charakteristiken von Kohlenstoffnanoröhren theoretisch zu untersuchen, werden verschiedene Methoden erwendet, die von *ab initio* first priciple Methoden über empirische Potentiale bis hin zu klassischen Modellen reichen. *Ab initio* Methoden sind rechnerisch teuer, so dass sie auf Systeme mit wenigen Atomen limitiert werden müssen. Empirische Potenziale können für größere Systeme verwendet werden, aber auch sie haben ihre Grenzen, wenn es um die Größe des betrachteten Systems geht. Um zum Beispiel ein System mit Millionen von Atomen zu analysieren, werden empirische Potentiale nicht gewählt. In solch einem Fall werden stattdessen klassische Modelle als sinnvoller Ersatz angewandt. Jedes Modell basiert auf einem Parametersatz, der mit *ab initio* Methoden oder mit empirischen Potentialen bestimmt worden ist. Sind die Parameter des Modells berechnet, kann das Modell dazu verwendet werden, die Eigenschaften des betrachteten Systems vorherzusagen.

Wie anfangs beschrieben, ist eine der großen Herausforderungen in der Forschung an Kohlenstoffnanoröhren ihre kontrollierte Herstellung. Um einen detaillierten theoretischen Einblick in dieses Problem zu bekommen, ist es wichtig, die Energetik, besonders im Hinblick auf Bindungsenergien und die Stabilität der Nanoröhren systematisch zu verstehen. In der vorliegenden Arbeit haben wir uns für die klassische Modellperspektive entschieden, um uns dieser Fragestellung zu nähern. Unser Ziel war es, ein klassisches Modell zu entwickeln, welches die Charakteristiken der Bindungsenergie und die Stabilität der Kohlenstoffnanoröhren erklären kann. Unser Modell haben wir in Anlehnung an das *liquid drop* Modell (Flüssigkeitstropfenmodell), welches in der Kern- und atomaren Cluster-Physik bekannt ist, das *liquid surface* Modell (Flüssigkeitsoberflächenmodell) genannt. Dem Modell liegt die Annahme zugrunde, dass sich die Energie der Nanoröhren in Abhängigkeit von geometrischen Parametern wie Oberfläche, Krümmung und Form des Randes ausdrücken lässt.

Das *liquid surface* Modell wurde für Kohlenstoffnanoröhren mit offenem und bedecktem Ende vorgeschlagen. Es wurde gezeigt, das die Energie bedeckter Nanoröhren von fünf physikalischen Parametern bestimmt wird, während für Kohlenstoffnanoröhren mit offenem Ende drei Parameter ausreichen. Die Parameter des *liquid surface* Modells wurden mit Hilfe des Tersoff und Brenner Potentials ermittelt. Die Genauigkeit des Modells wurde ebenfalls analysiert. Es konnte so gezeigt werden, dass das *liquid surface* Modell die Bindungsenergie pro Atom einer Nanoröhre mit einer relativen Fehlerrate von unter 0,3% vorhersagen kann, was einem absoluten Energieunterschied unter 0.01 eV entspricht.

Der Einfluss eines katalytischen Nanopartikels, auf dem eine Nanoröhre wächst, wurde ebenfalls diskutiert. Es wurde gezeigt, dass katalytische Nanopartikel verheerende Auswirkungen auf die Bindungsenergie pro Atom haben. Insbesondere wurde demonstriert, dass, wenn die Wechselwirkung einer Nanoröhre mit einem katalytischen Nanopartikel schwach ist (d.h. $\lesssim 1$ eV),

der Anbau eines zusätzlichen Atoms ein energetisch günstiger Prozess ist. Ist dagegen die Wechselwirkung stark (d.h. $\gtrsim$ 1 eV), ist der Zerfall der Nanoröhre energetisch günstiger. Das vorgeschlagene Modell gibt wichtige Einsichten in die Energetik und Stabilität von Nanoröhren unterschiedlicher Chiralität und liefert einen wichtigen Beitrag zum Verständnis des Wachstumsprozesses von Nanoröhren.

Des weiteren haben wir die Elastizität von Nanoröhren analysiert und Vergleiche mit verfügbaren experimentellen Messungen und früheren theoretischen Vorhersagen gemacht. Wir haben das Youngsche Modul und die Krümmungskonstante für einwandige Kohlenstoffnanoröhren aus den Parametern des *liquid surface* Modells berechnet und gezeigt, dass die resultierenden Werte in Einklang mit den früher publizierten Werten sind. Das berechnete Youngsche Modul und die Krümmungskonstante wurden verwendet, um Rückschlüsse über die Genauigkeit des Tersoff und Brenner Potentials zu ziehen. Die Elastizitätseigenschaften wurden von den Parametern des *liquid surface* Modells abgeleitet, folglich korrespondieren sie mit den berechneten Werten der Grundstruktur des Tersoff und Brenner Potentials. Es wurde gezeigt, dass die bestimmten Werte des Youngschen Moduls und die Krümmungskonstante innerhalb der voher publizierten Bereiche für beide Potentiale liegen. Dies deutet darauf hin, dass das Tersoff und Brenner Potential die Elastizitätseigenschaften von Nanoröhren adäquat beschreibt.

Obwohl in dieser Arbeit das Modell lediglich für offene und bedeckte, einwandige Kohlenstoffnanoröhren entwickelt wurde, könnte es erfolgreich auf eine Vielfalt von Systemen erweitert werden. Dies würde dadurch erreicht, dass zusätzliche Terme, die die Geometrie des betrachteten Systems beschreiben, in den Ausdruck der Gesamtenergie hinzugenommen werden. Zum Beispiel könnte durch Addition eines Terms für Volumenenergie, die Untersuchung der Energetik und Stabilität von mehrwandigen Nanoröhren ermöglicht werden. Eine andere wichtige Kategorie von Nanoröhren, die mit Hilfe des *liquid surface* Modells analyisert werden könnten, sind deformierte

(wie toroidale oder spirale) Nanoröhren. Deformierte Nanoröhren haben in letzter Zeit hohe Aufmerksamkeit erregt, da beobachtet wurde, dass mechanische Deformationen die elektrischen Eigenschaften von Nanoröhren erheblich beeinflussen können.

Eine andere wichtige Eigenschaft, die mit dem *liquid surface* Modell untersucht werden könnte, ist die Wechselwirkung mehrerer Nanoröhren, zum Beispiel in kristallinen Feldern. Bei der Herstellung wachsen CNT meist in Bündeln oder Wäldern, einzelne Nanoröhren werden aus dem Bündel durch verschiedene Purifikationsmethoden separiert. Die Wechselwirkung von Nanoröhren in einem Feld spielt eine wesentliche Rolle im Wachstum des gesamten Systems und kann mit Hilfe des *liquid surface* Modells analysiert werden.

Auch die Untersuchungen von elastischen Eigenschaften können auf viele verschiedene Systeme wie mehrwandige Nanoröhren, Nanoseile und Nanobündel, welche als potentielle Kandidaten für hoch feste Materialien gesehen werden, erweitert werden. Ein besseres Verständnis der elastischen Eigenschaften solcher Systeme würde helfen, leichtere und festere Materialien zu produzieren, was für die Industrie von besonderem Interesse ist.

Wachstumsmechanismen von Kohlenstoffnanoröhren sind ein viel diskutiertes Thema und es gibt viele sich widersprechende Aussagen. Tatsächlich ist eines der Hauptprobleme, dem sich Experimentalphysiker im Moment stellen, die Produktion von Nanoröhren mit gegebener Chiralität. Ein Schlüssel zu diesem Problem ist, das Verständnis über die Eigenschaften der Bindungsenergie und die Stabilität der Nanoröhren in der Gegenwart von katalytischen Nanopartikeln zu erweitern. Das *liquid surface* Modell könnte durch die Analyse des Verhaltens der Bindungsenergien von Nanoröhren verschiedener Chiralität einige Einsichten in diese Thematik liefern. Unsere Studien haben gezeigt, dass die Wechselwirkungen mit katalytischen Nanopartikeln einen großen Einfluss auf die Energetik und dadurch auf den Wachstumsmechanismus der CNT haben. Die Untersuchung kann durch Ver-

wendung spezieller Potentiale für diese Interaktion erweitert werden. Desweiteren sollte, um ein angemessenes Verständnis des Wachstumsmechanismuses von Kohlenstoffnanoröhren zu bekommen, die Interaktion von Nanoröhren und katalytischen Partikeln mit dem Substrat betrachtet und in zukünftigen Analysen und Studien mit einbezogen werden.

Contents

1

Introduction

Carbon is considered to be one of the few elements known to humans since antiquity which appears in a variety of forms It is the fourth most abundant element in the universe by mass after hydrogen, helium, and oxygen. It is present in all known life forms, and in the human body, carbon is the second most abundant element by mass (about 18.5%) after oxygen [2]. This abundance together with the unique diversity of organic compounds and their unusual polymer-forming ability at the temperatures commonly encountered on earth, make this element the chemical basis of all known life. Atomic carbon is a very short-lived species and therefore, carbon is stabilised in various multi-atomic structures with different molecular configurations called allotropes. In each allotrope, the atoms are bonded together in a totally manner.

The three relatively well-known allotropes of carbon are amorphous carbon, graphite, and diamond. Amorphous carbon has no crystalline structure. In diamond, the carbon atoms are bonded together in a tetrahedral lattice arrangement, while in graphite, they are bonded together in sheets of a hexagonal lattice. Because of these differences in arrangement of atoms, the physical properties of carbon vary widely with the allotropic form. Diamond is highly transparent, while graphite is opaque and black. Diamond is among the hardest materials known, while graphite is soft enough to form a streak on paper. Diamond has a very low electric conductivity, while graphite is a very good conductor. Also, diamond has the highest thermal conductivity of all known materials under normal conditions. All the allotropic forms

are solids under normal conditions but graphite is the most thermodynamically stable. During the previous decades, other allotropic forms of carbon are synthesised which include buckyballs [3], carbon nanotubes [1], carbon nanobuds [4], and nanofibres [5]. Several other exotic allotropes have also been discovered, such as aggregated diamond nanorods [6], lonsdaleite [7], glassy carbon [8] and carbon nanofoam [9]. A few of these allotropes are shown in Fig. 1.1.

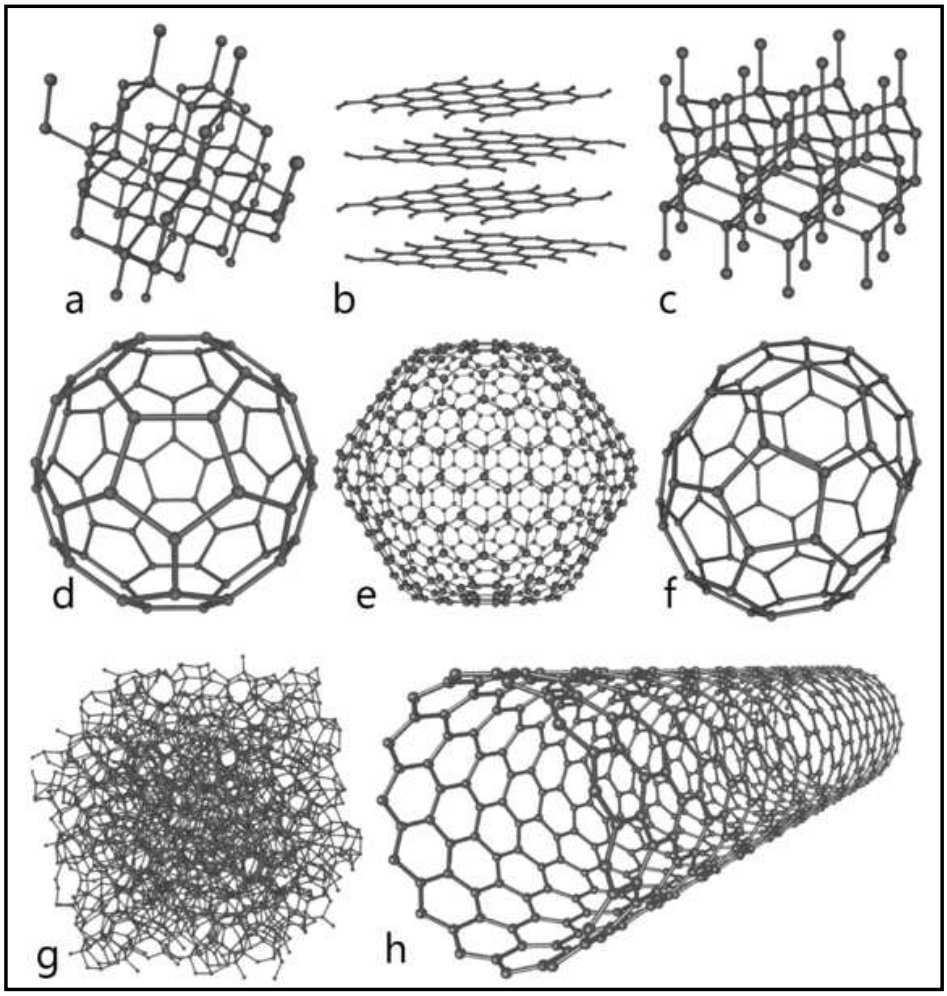

Figure 1.1: Figure illustrating eight different allotropes of carbon. a) Diamond, b) Graphite, c) Lonsdaleite, d) Buckminsterfullerene (C60), e) C540, f) Fullerene (C70), g) Amorphous carbon, h) single-walled carbon nanotube [10].

Carbon nanotubes (CNTs) are cylindrical shaped allotropes of carbon whose diameter lie in the range of nanometers. Ever since their discovery by Sumio Iijima of NEC in 1991 [1] huge amount of research is being done in this field and people realized their exceptional qualities which could revolutionise technology. Although a detailed understanding of carbon nanotubes and their properties are known experimentally, the researchers could not progress much in understanding them from a theoretical point of view. This leads to one of the most discussed issues in the field of carbon nanotubes research, namely, producing nanotubes in a well-controlled manner. Despite the huge amount of efforts by experimentalists to produce high quality carbon nanotubes in a desired manner, the issue remains still open. This demands a detailed understanding of carbon nanotubes from a theoretical point of view.

In order to study the properties of carbon nanotubes theoretically, research community uses all possible methods ranging from *ab initio* first principle methods, empirical potentials, and classical models. *Ab initio* first principle methods are computationally expensive and hence they are limited to systems of a few atoms. Empirical potentials can be used for bigger systems but they too have their own limitations on the size of the system to be studied. For example, in order to study a system with millions of atoms, empirical potentials are not favoured. In such cases, classical models could be used as a successful substitute. Every model is based on a set of parameters which could be obtained from first principle calculations or calculations using empirical potentials. Once the parameters of the model are obtained the model could be used to predict the characteristics of the system under consideration.

1.1 Aims of the thesis

The major problem facing in carbon nanotube research is production of nanotubes in a well-controlled manner. Unless they are produced in a controlled

manner, the commercialisation of nanotubes is impossible. In order to get a detailed theoretical understanding of this problem, one needs to understand the energetics, especially the binding energy characteristics, and stability of nanotubes in a systematic way. This problem could be approached from different theoretical points. In this thesis, we approach this problem from a classical model perspective. So, the aim of this work is to develop a classical model which can successfully explain the binding energy characteristics and stability of carbon nanotubes. We call this model as liquid surface model. The model assumes that the energy of a nanotube can be expressed in terms of its geometrical parameters like surface area, curvature and edge. The model is developed for both open end and capped carbon nanotubes and it is used for the study of elastic properties of nanotubes as well as the effect of catalytic particles on the stability of them.

Although in this thesis we developed the model only for open end and capped single-walled carbon nanotubes, it could be successfully extended for the study of a variety of systems. This is achieved by adding extra terms in the total energy which take into account the geometry of the systems under consideration. For example, adding a volume energy term would enable the model to be used as a tool for the study of the energetics and stability of multiwall nanotubes. Another important category of nanotubes which could be studied with the help of liquid surface model is deformed nanotubes like toroidal or spiral shaped. Deformed nanotubes are getting much attention recently because of the discovery that mechanical deformations can change the electrical properties of nanotubes tremendously.

One of the most debated topics in nanotube research is its growth mechanism. Although considerable achievement is gained in the experimental aspect of this problem, theoretical understanding remains relatively poor. The first and foremost requirement for the commercialisation of nanotube-based products is the ability to produce nanotubes of desired chirality. A

key to this problem is the understanding of the binding energy characteristics and stability of nanotubes in presence of catalytic nanoparticles. Liquid surface model is able to provide at least some qualitative understanding on this topic by analysing how the energetics of nanotubes changes depending on the presence of a catalytic nanoparticle.

The thesis is organised as follows. Chapter 2 gives an overview of carbon nanotubes. The historical development which led to the discovery of carbon nanotubes as well as the classification of nanotubes are presented in section 2.1. Section 2.2 is devoted for the theoretical description of carbon nanotubes, where the concept of chirality is introduced. The three major experimental methods used for the production of carbon nanotubes along with their advantages and disadvantages are described in Section 2.3. Section 2.4 overviews the possible applications of carbon nanotubes.

Various physical properties of carbon nanotubes obtained from experiments and theory are described in Chapter 3. In section 3.1 the mechanical properties including Young's modulus and tensile strength of carbon nanotubes are explained. Electronic properties are described in section 3.2.1 and thermal properties are explained in section 3.2.2. This follows with Section 3.2.3, which deals with the optical properties of nanotubes. Finally, section 3.3 of the chapter explains how various physical properties of a nanotube are influenced by defects on them.

Chapter 4 deals with different theoretical methods employed in general for the study of carbon nanotubes. Section 4.1 gives a brief overview on first principle, semi-empirical and empirical methods. This is followed by a detailed description of different force fields used in this thesis for obtaining parameters of our model in section 4.2. Theoretical framework of Brenner potential and Tersoff potential are detailed in this section.

Liquid surface model for open and capped carbon nanotubes and its the-

oretical framework are given in Chapter 5. This chapter starts with an introduction to the model and gradually explains the theoretical background of the model and the results obtained by this model.

The thesis is summarised in Chapter 6 and the possible extensions of the model are discussed.

2

Carbon Nanotubes: Structure, Synthesis and Applications

2.1 Introduction

Carbon nanotubes are tube shaped allotropes of carbon which have typical diameters of a few nanometers and aspect ratios greater than 100 [1]. Aspect ratio refers to the ratio between the diameter and the length of the tube. Their name is derived from their size, since the diameter of a nanotube is on the order of a few nanometers. Although there are other claims in the scientific world, Iijima of NEC is generally accepted as the discoverer of carbon nanotubes [1].

2.1.1 History of nanofibres

It appears that the first carbon filaments of nanometer dimensions were prepared in the 1970s by Morinobu Endo, as part of his PhD studies at the University of Orleans in France [11]. He grew carbon fibres about 7 nm in diameter using a vapour-growth technique, but these filaments were not recognised as nanotubes and were not studied systematically. It was not until 1991, when Sumio Iijima of the NEC Laboratory in Tsukuba used high-resolution transmission electron microscopy (HRTEM) to observe carbon nanotubes [1], that the field really started to take off. Researchers at the Institute of Chemical Physics in Moscow independently discovered car-

bon nanotubes and nanotube bundles at about the same time, but these generally had a much smaller length-to-diameter ratio [12]. The shape of these nanotubes led the Russian researchers to call them barrelenes. The history of carbon nanotube discovery is reviewed in detail elsewhere [13]. The discovery of fullerenes by Harold Kroto of Sussex University in the UK and Richard Smalley and co-workers at Rice University in the US [3] stimulated researchers to explore carbon filaments further. Indeed, the realization that the ends of carbon nanotubes must be fullerene-like caps explained the fact that the diameter of a carbon nanotube could only be as small as a fullerene molecule.

If one neglects the two ends of carbon nanotube and focus on the large aspect ratio of the cylinder, these nanotubes can be considered as one-dimensional nanostructures. Ever since the discovery of carbon nanotubes, considerable research has been devoted to the study of various properties of it. Nanotubes can be either electrically conductive or semiconductive, depending on their helicity, leading to nanoscale wires and electrical components. These one-dimensional fibres exhibit electrical conductivity as high as copper, thermal conductivity as high as diamond, strength 100 times greater than steel at one sixth the weight, and high strain to failure. In fact, they are considered to be the strongest fibres known.

2.1.2 Classification of carbon nanotubes

Carbon nanotubes are classified into various categories according to different criteria. One of the most important classification is as single-walled carbon nanotubes (SWCNTs) and multi-walled carbon nanotubes (MWCNTs). As the name suggests, this classification is based on the number of walls a nanotube possesses. A multi-walled nanotube has multiple numbers of concentric single-walled nanotubes whose radii are different. Fig. 2.1 illustrates this type of classification where the first figure shows a single-walled nan-

Figure 2.1: Figure illustrating single-walled (SW), double-walled (DW) and multi-walled (MW) carbon nanotubes (CNTs). Multi-walled nanotubes are formed by multiple single walled nanotubes of different radii. In general, any number of concentric cylinders are possible for a multi-walled nanotube [14].

otube, the second figure depicts a double-walled nanotube and the third one is a multi-walled nanotube.

As it is evident from Fig. 2.1, a single-walled carbon nanotube can be described as a graphene sheet rolled into a cylindrical shape so that the structure is one dimensional with axial symmetry, and in general exhibiting a spiral conformation, called chirality. Chirality defines how much twist a carbon nanotube has and it is this quantity which determines the symmetry of a nanotube. In accordance with their symmetry, carbon nanotubes are classified as chiral and achiral. An achiral carbon nanotube is defined by a carbon nanotube whose mirror image has an identical structure to the original one. There are only two cases of achiral nanotubes, namely zigzag and armchair. The details of this kind of classification is described in Sec. 2.2.1.

2.2 Structure of carbon nanotubes

All single-walled carbon nanotubes can be visualised as a conformal mapping of 2D graphite (graphene) onto the surface of a cylinder [1, 15]. The rolling of a graphene sheet can be done in many different ways and each of them

gives nanotubes of different twist. In general, the structure of a single-walled carbon nanotube is specified by a vector called chiral vector, which is perpendicular to the axis of the nanotube. When a graphene sheet is rolled into a nanotube, not only the carbon atoms have to line up around the circumference of the tube, but the quantum mechanical wavefunctions of the electrons must also match up. In quantum mechanics the electrons are smeared out; in a nanotube this electron smear must match up when going once around the tube. This matching requirement restricts the types of wavefunctions that the electrons can have, which then affects the motion of the electrons. Depending on exactly how the tube is rolled up, the nanotube can be either a semiconductor or a metal. The concept of chiral vector and other symmetry related concepts in a nanotube are discussed in the following subsections.

2.2.1 Chiral vector

The idea of obtaining a carbon nanotube from a graphene sheet as well as the concepts of zigzag, armchair and chiral nanotubes are discussed in Fig. 2.2. As mentioned before, the way of rolling the graphene sheet determines the chirality of a nanotube [15, 17, 18]. The chirality is specified by two integer numbers, n and m, where $0 \leq m \leq n$. This condition arises because of the hexagonal symmetry of the honeycomb lattice. The hexagonal symmetry of the lattice makes sure that corresponding to every nanotube with $m > n$ there exists an equivalent nanotube with $0 \leq m \leq n$. If $m = 0$, the nanotube is called zigzag while if $m = n$, it is called armchair. The names armchair and zigzag arise from the shape of the cross-sectional ring. All other nanotubes are called chiral nanotubes [17]. Fig. 2.3 shows an armchair and a zigzag nanotubes where the shape of the cross-sectional ring is marked red. A chiral nanotube with chirality $n = 7$, $m = 4$ is depicted in Fig. 2.4.

The vector in the graphene sheet, defined by n and m is called the chirality vector. In Fig. 2.2 it is denoted as $\vec{C_h}$. To define the chirality vector, two basis

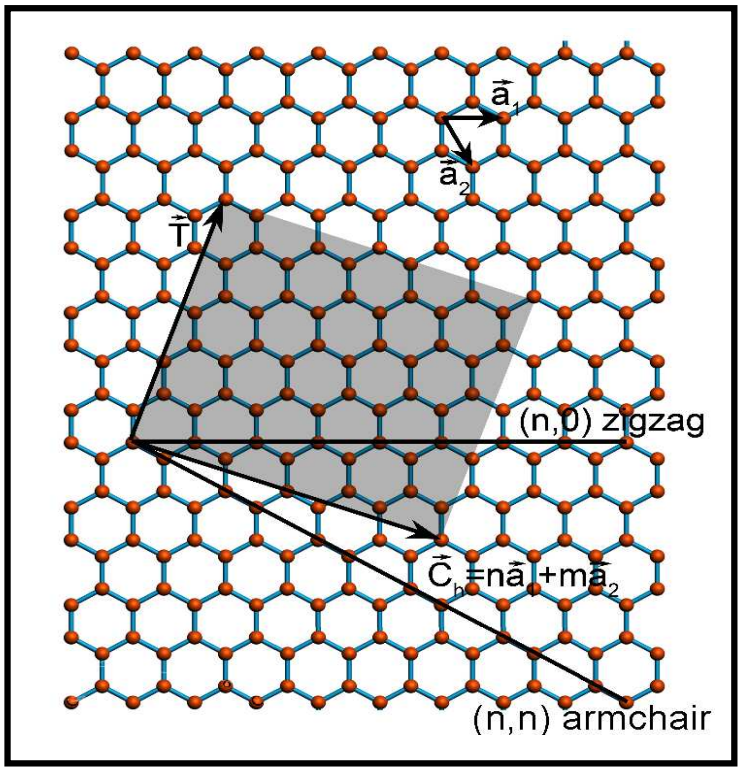

Figure 2.2: Construction of a nanotube from a graphene sheet. The vectors $\vec{a_1}$, $\vec{a_2}$ are the basis vectors in the graphene sheet. The chiral index n is the number of steps in the $\vec{a_1}$ direction and the chiral index m is that in the $\vec{a_2}$ direction. $\vec{C_h} = n\vec{a_1} + m\vec{a_2}$ is the chirality vector, and $\vec{T}$ is the translation vector which is in the direction of the tube axis. The chiral vector directions for both zigzag (m=0) and armchair (m=n) nanotubes are indicated [16].

vectors $\vec{a_1}$ and $\vec{a_2}$ are introduced. The chiral indices n and m are the number of steps that should be taken along the $\vec{a_1}$ and $\vec{a_2}$ directions respectively in order to reach the tip of the chirality vector.

$$\vec{C_h} = n\vec{a_1} + m\vec{a_2} \tag{2.1}$$

If a is the distance between two adjacent carbon atoms in the graphene sheet, $\mid \vec{a_1} \mid = \mid \vec{a_2} \mid = \sqrt{3}a$. Hence the chirality vector becomes:

$$\vec{C_h} = \sqrt{3}a\sqrt{n^2 + m^2 + nm} \tag{2.2}$$

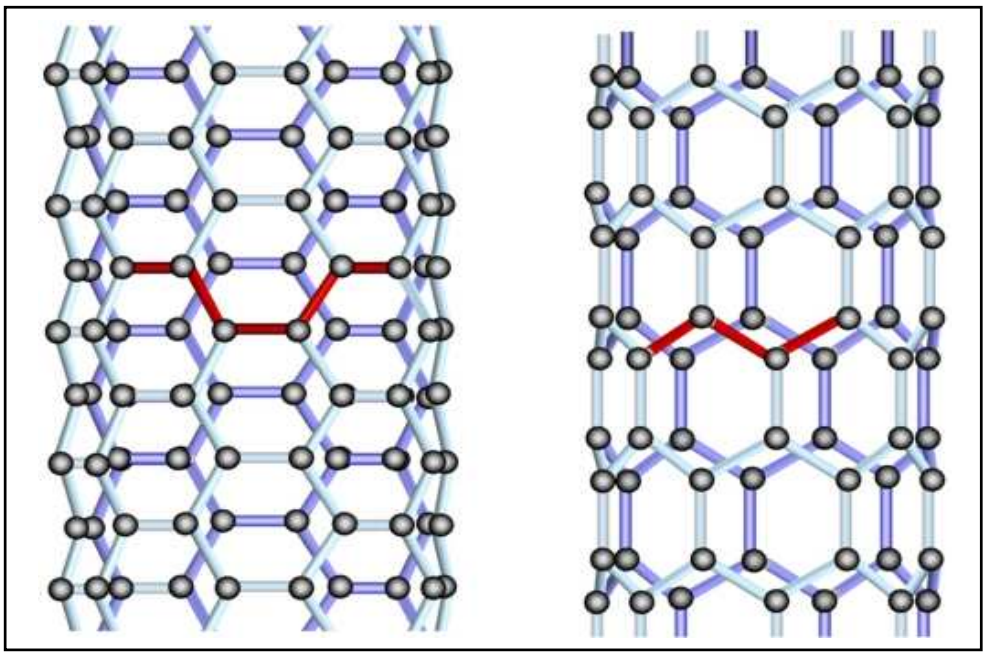

Figure 2.3: Figure illustrating armchair ($m = n$) and zigzag ($m = 0$) nanotubes. The names armchair and zigzag arise from the shape of the cross-sectional ring which is marked red in the figure [19].

To construct a nanotube, the graphene sheet is folded along the chirality vector, which in turn defines the perimeter ($2\pi R$) of the nanotube. This gives the radius of the nanotube as [15, 17, 18]:

$$R = \frac{\sqrt{3}a\sqrt{n^2 + m^2 + nm}}{2\pi} \tag{2.3}$$

The chirality of a nanotube can be expressed using a chiral angle too. The chiral angle θ is defined as the angle between the vectors $\vec{C_h}$ and $\vec{a_1}$ (see Fig. 2.2), with values of θ in the range $0^\circ \leq \mid \theta \mid \leq 30^\circ$, because of the hexagonal symmetry of the honeycomb lattice. The chiral angle θ denotes the tilt angle of the hexagons with respect to the direction of the nanotube axis and it specifies the spiral symmetry. The chiral angle θ can be obtained

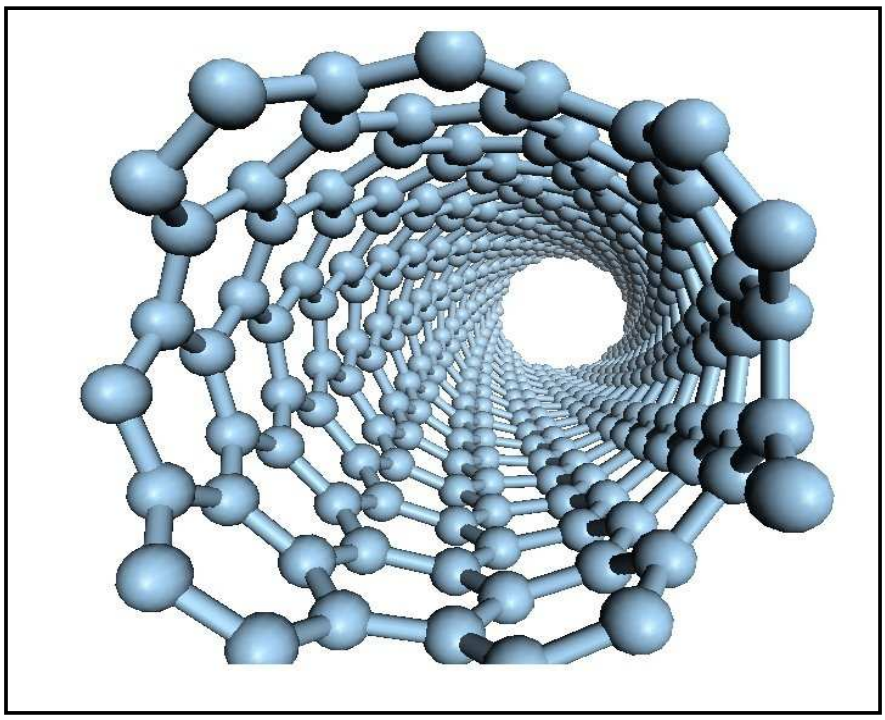

Figure 2.4: A chiral nanotube with chirality $n = 7$, $m = 4$. The chirality of a nanotube refers to the twist of the hexagons with respect to the axis of the tube.

by taking the inner product of $\vec{C_h}$ and $\vec{a_1}$, to yield an expression for $cos\theta$:

$$cos\theta = \frac{\vec{C_h} \cdot \vec{a_1}}{\mid \vec{C_h} \mid\mid \vec{a_1} \mid} = \frac{2n + m}{2\sqrt{n^2 + m^2 + nm}} \tag{2.4}$$

In particular, zigzag and armchair nanotubes correspond to $\theta = 0°$ and $\theta = 30°$, respectively.

2.2.2 Translational vector

Because of the honeycomb symmetry of the hexagonal lattice from which a nanotube is formed, every nanotube has a periodicity in the axial direction.

Translational vector represents this periodicity of a nanotube. It is perpendicular to the chirality vector and in Fig. 2.2 it is denoted as $\vec{T}$. It is clear from Fig. 2.2 that the lattice vector $\vec{T}$ can be expressed in terms of the basis vectors $\vec{a_1}$ and $\vec{a_2}$ as:

$$\vec{T} = t_1\vec{a_1} + t_2\vec{a_2} \tag{2.5}$$

Here t_1 and t_2 are integers. The tip of the translation vector $\vec{T}$ coincides with the first lattice point in the direction perpendicular to the chiral vector $\vec{C_h}$. From this fact, it is clear that t_1 and t_2 do not have a common divisor except for unity. Using the property: $\vec{C_h} \cdot \vec{T} = 0$, one can obtain expressions for t_1 and t_2 given by:

$$t_1 = \frac{2m+n}{d}, \quad t_2 = -\frac{2n+m}{d} \tag{2.6}$$

where d is the greatest common divisor (gcd) of $(2m+n)$ and $(2n+m)$. For a nanotube of chiral indices n, m and inter atomic distance a, the magnitude of translational vector can be expressed as:

$$|\vec{T}| = \frac{3a\sqrt{n^2+m^2+nm}}{d} \tag{2.7}$$

The region defined by the vectors $\vec{T}$ and $\vec{C_h}$ is called the unit cell of the 1D carbon nanotube. In Fig. 2.2, the rectangular shaped shaded region is the unit cell. For any nanotube, the number of carbon atoms in the unit cell can be obtained as follows:

$$N = 2\frac{|\ \vec{C_h} \times \vec{T}\ |}{|\ \vec{a_1} \times \vec{a_2}\ |} = \frac{4(n^2+m^2+nm)}{d} \tag{2.8}$$

Since each hexagon contains two carbon atoms, there are $2N$ carbon atoms in each unit cell of the carbon nanotube.

2.3 Synthesis of carbon nanotubes

Ever since the discovery of carbon nanotubes, considerable amount of research has been done in this field which revealed that the various exceptional properties of carbon nanotubes can be utilised in a wide range of novel applications [18, 20]. This has motivated much research in nanoscience and nanotechnology. However, the realization of most of the proposed applications requires not only scalable methods of synthesising high-purity nanotubes, but also control over their location and orientation. New methods have developed for the synthesise of carbon nanotubes [21–26] which succeeded in significantly increasing the overall yield, but improvements in quality and control over chirality are still not achieved completely. In general, the synthesis of carbon nanotubes can be divided into two broad categories: physical methods, which rely on big energies to release the carbon atoms from their precursors, such as arc discharge [1, 27–29] and laser ablation [30–35], and chemical methods, which catalytically decompose the carbon precursors to release the atoms, such as chemical vapour deposition (CVD) [21, 36–41]. Chemical methods can be further classified into substrate based CVD methods and the floating catalyst, or aerosol, method [22–26, 42]. All these methods are described in details in the following sections.

2.3.1 Arc discharge method

This is the earliest method for the synthesis of carbon nanotubes and it is what Iijima *et al.* [1] used to discover randomly arranged multi-walled carbon nanotubes for the first time. Arc discharge method produces structurally sound but relatively impure carbon nanotubes. A schematic diagram of the settings for arc discharge method is given in Fig. 2.5. Nanotube generation with this technique involves striking a dc arc discharge in an inert gas (such as argon or helium) between a set of graphite electrodes [1, 27–29]. This is

done by the passage of a direct current through two high purity graphite electrodes. DC current is preferred over alternate current (AC) because it provides the highest yield of nanotubes. This process produces a hard grey shell which many refer to as "soot" at a rate of 1 mm/min on the negative electrode (cathode), whereas the positive electrode (anode) is continuously consumed. The inner core of the soot contains carbon nanotubes and nested polyhedral graphene particles. The inert gas flow is maintained at 50-600 Torr. Nominal conditions involve 2000-3000° C, 100 amps and 20 volts.

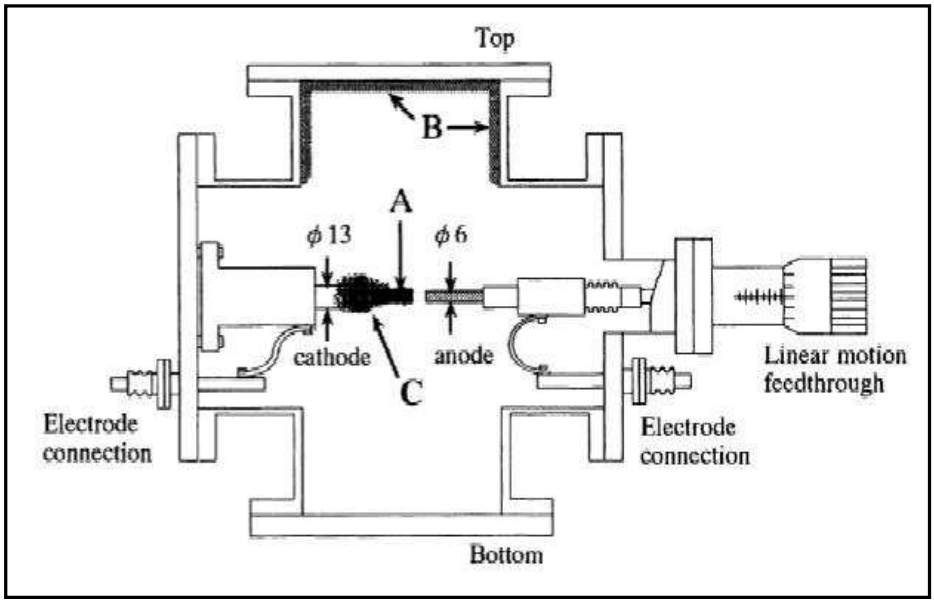

Figure 2.5: Schematic diagram showing the set up for arc discharge method for the production of carbon nanotubes as developed by Saito in 1995 [43].

In order to produce single-walled carbon nanotubes, a metal catalyst is used in this process. Iijima was also able to produce SWNTs by arcing Fe-graphite electrodes in a methane-argon atmosphere. A few years later, Bethune produced SWNTs with this arc method using Fe-Co-Ni-graphite mixtures in a He atmosphere. By using this set of electrodes, the nanotubes were found in bundle arrangements with average diameters of 1.2 nm. Nowa-

days, the most effective catalysts to produce SWNTs are Y-Ni_2, Fe-Ni_3, and Rh-Pt_4. These graphite mixtures that are used as the electrode are capable of yielding up to 70 % of SWNTs. Recent studies using the arc discharge method has been on improving the crystallinity of the SWNTs.

There are several problems associated with the electric arc-discharge method. Perhaps the biggest problem with this technique is the overall cost. If one wants to produce SWNTs with this technique, one needs to have high-purity graphite electrodes, high purity metallic mixtures, and high-purity He and Ar gases. Other problems with this technique are that there is very little control over the diameter of the nanotubes and by-products are always present within the "soot" which makes it cumbersome (or impossible) to separate the carbon nanotubes from the polyhedral graphite particles (in the case of MWNTs) or from the encapsulated metal particles (in the case of SWNTs). In addition to these "impurities", there is always a portion of amorphous carbon that is found within the "soot" which is highly undesired and difficult to remove after the formation of nanotubes. The gas pressure, flow rate, and metal concentration can be varied to change the yield of nanotubes, but these parameters do not seem to change the diameter distribution. Typical diameter distribution of SWCNTs by this process appears to be 0.7-2 nm.

Although arc discharge is not amenable to the application of precise quantities such as those required in nanoelectronics, it is a relatively high-volume production method. A recent refinement of this technique developed at NASA has resulted in much higher yield rates than the usual 30%, approaching the 70% range [44]. Large-scale synthesis of SWCNT by the arc discharge method yielded quantities of tens of grams a day under arc conditions of $40 \sim 60$ A d.c. and helium pressures of 500 to 700 torr. Recent results show that helium atmosphere strongly affects the yield of SWNTs, and that the diameter distribution of the SWNTs is affected by the catalyst.

2.3.2 Laser ablation method

In 1996, Smalley's group at Rice University reported the synthesis of carbon nanotubes by laser vapourisation [31]. In this method, a pulsed or continuous laser is used to vapourise a graphite target in an oven at nearly 1200°C. The main difference between continuous and pulsed laser is that the pulsed laser demands a much higher light intensity (100 kWcm^2 compared with 12 kWcm^2 for continuous laser). The oven is filled with helium or argon gas in order to keep the pressure at 500 Torr. A schematic diagram of the experimental set up for laser ablation method is shown in Fig. 2.6. A YAG [34] or CO_2 [33] laser impinges on a carbon composite target situated in the centre of a quartz tube which is placed inside a tube furnace. The target normally comprises graphite mixed with a small amount of transition metal particles as catalyst. A typical target used to fabricate nanotubes is made out of graphite-Co-Ni. The laser beam has sufficient energy density to convert the graphite into amorphous carbon.

Once the target is irradiated with the laser pulse, a very hot vapour plume forms, then expands and cools rapidly. As the vapourised species cool, small carbon molecules and atoms quickly condense to form larger clusters, possibly including fullerenes. Argon flow through the reactor carries the vapour, carbon clusters and nucleated nanotubes which continue to grow and deposit them on the cooler walls of the quartz tube downstream from the furnace. This produces a high percentage of single-walled carbon nanotubes (70 %) with the rest being catalyst particles and soot. The catalysts also begin to condense, but more slowly at first, and attach to carbon clusters and prevent their closing into cage structures. Catalysts may even open cage structures when they attach to them. From these initial clusters, tubular molecules grow into single-walled carbon nanotubes until the catalyst particles become too large, or until conditions have cooled sufficiently that carbon no longer can diffuse through or over the surface of the catalyst particles. It is also

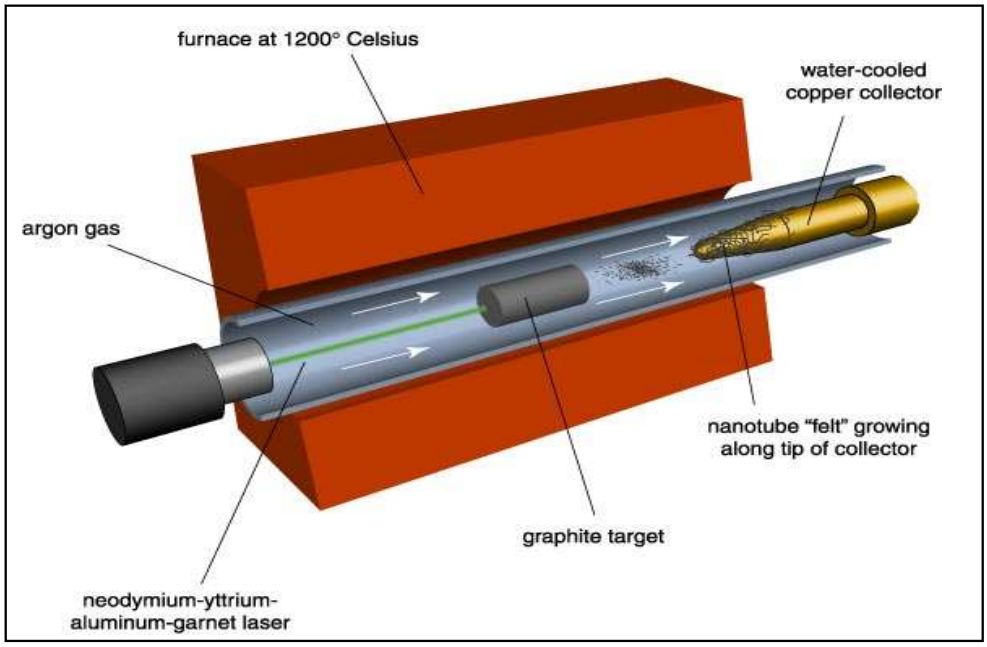

Figure 2.6: Schematic diagram showing the experimental set up of laser ablation method for CNT production. Nanotubes grown this way self-organize into ropes with promise for engineering applications. In this technique, a laser is aimed at a block of graphite, vaporizing the graphite. Contact with a cooled copper collector causes the carbon atoms to be deposited in the form of nanotubes. The nanotubes deposited can then be harvested [45].

possible that the particles become that much coated with a carbon layer that they cannot absorb more and the nanotube stops growing. The single-walled nanotubes formed in this case are bundled together by van der Waals forces.

There are some striking, but not exact similarities, in the comparison of the spectral emission of excited species in laser ablation of a composite graphite target with that of laser-irradiated C_{60} vapour [32]. This suggests that fullerenes are also produced by laser ablation of catalyst-filled graphite, as is the case when no catalysts are included in the target. However, subsequent laser pulses excite fullerenes to emit C_2 that adsorbs on catalyst particles and feeds SWNT growth. However, there is insufficient evidence to conclude this with certainty. It is also important to note that multi-walled

nanotubes can be grown with this technique by using high-power laser vaporisation (YAG or Nd-YAG type) of pure graphite targets inside a furnace at 1200°C, in an Ar atmosphere.

Laser ablation products from fullerene materials have been studied by transmission electron microscopy and Raman spectroscopy. Using nickel and cobalt as a catalyst, single-walled carbon nanotubes were produced at an ambient temperature of 400° C. The results were compared with those using graphite as starting materials. It is suggested that the formation of single-walled carbon nanotubes is controlled by both the availability of proper precursors and the activity of the metal catalyst. The main problem with this technique is reproducibility. It is also difficult to control the chirality, length, and diameter of the nanotubes. Over the past few years, the diameter has been able to be controlled better by increasing the power of the laser. As the laser pulse power is increased, the diameter of the tubes become narrower. Perhaps the biggest problem associated with this technique is that the maximum output of carbon nanotubes that can be formed is very less (1.5 g/hr) which makes this method economically ineffective. Some research groups have been able to increase the yield of CNTs by using extremely fast pulses and by using porous targets opposed to the standard metal targets. Laser ablation requires costly apparatus to produce small quantities of high-quality SWCNT with purity ranging from 70% to 90%.

Laser ablation is almost similar to arc discharge, since the optimum background gas and catalyst mix is the same as in the arc discharge process. This might be due to very similar reaction conditions needed, and the reactions probably occur with the same mechanism. This method has proven successful at producing nanotubes with low density of defects [35].

2.3.3 Chemical vapour deposition method

Chemical vapour deposition (CVD) for the production of carbon nanotubes was developed by Z.F Ren in 1998 [46]. This process involves the decomposition of hydrocarbons over metal catalysts. Depending on the way the catalysts are use, CVD methods can be further classified into substrate based methods [22–26, 42] and the floating catalyst, or aerosol, method [47]. In CVD method, the carbon atoms that form the nanotube are introduced as a feedstock such as CO, ethane or other carbon-rich gases (e.g. methane, benzene, acetylene, naphthalene, ethylene, etc) [37, 40]. This feedstock is pumped to a chamber where catalyst particles are located either in a floating state or on top of a substrate. The catalyst particles are mostly metal clusters (e.g. Co, Ni, Fe, Pt, Pd). The typical temperature of the chamber varies from 800 K to 1300 K. Growth of carbon nanotube on top of the catalyst particle is observed at this temperature range both in experiments [37, 41] and in molecular dynamics simulations [48]. In the floating catalyst method, catalyst particles are suspended in a flow of carbon containing gas, both being continuously fed into the reactor. This presents a viable way for continuous production of single-walled carbon nanotubes and avoids catalyst-poising issues. A schematic diagram of the experimental set-up of CVD is shown in Fig. 2.7.

It has been shown that CVD is amenable for nanotube growth on patterned surfaces, suitable for fabrication of electronic devices, sensors, field emitters and other applications where controlled growth over masked areas is needed for further processing. More recently, plasma enhanced CVD (PECVD) has been investigated for its ability to produce vertically aligned nanotubes [50]. Production of carbon nanotubes through CVD methods is especially well suited to electronic manufacturing applications in which nanotube structures must be grown in precise quantities and locations. Fig. 2.8 shows a patterned array of carbon nanotubes produced using CVD method.

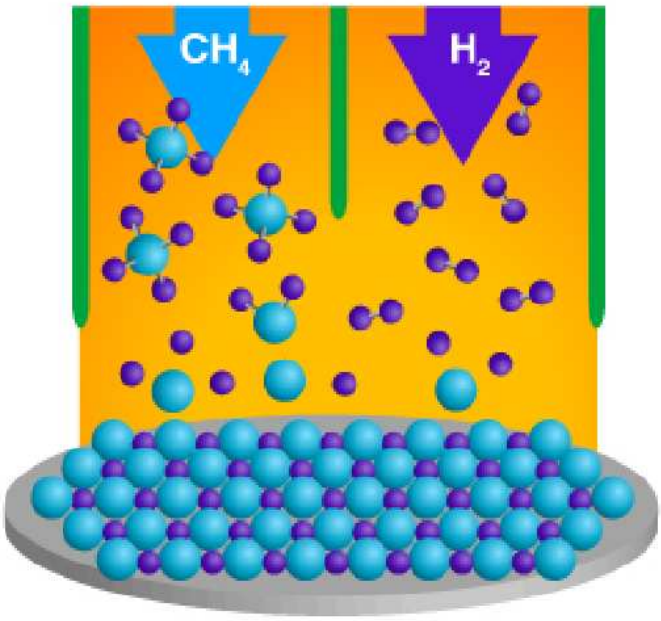

Figure 2.7: Schematic diagram showing the experimental set-up of Chemical Vapour Deposition (CVD) method for CNT production [49].

CVD methods can also be harnessed to the production of long strands of carbon nanotube, typically of the multi-walled rather than single-walled variety, for use in ultra-strong rope and similar products.

Recently, experimentalists have succeeded in developing various forms of CVD methods. A thermal CVD reactor is simple and inexpensive to construct, and consists of a quartz tube enclosed in a furnace [52]. Typical laboratory reactors use a 1 or 2 inch quartz tube, capable of holding small substrates. The substrate material may be Si, mica, quartz, or alumina. The setup needs a few mass flow controllers to meter the gases and a pressure transducer to measure the pressure. The growth may be carried out at atmospheric pressure or slightly reduced pressures using a hydrocarbon or CO feedstock. The growth temperature is in the range of 700-900° C. A

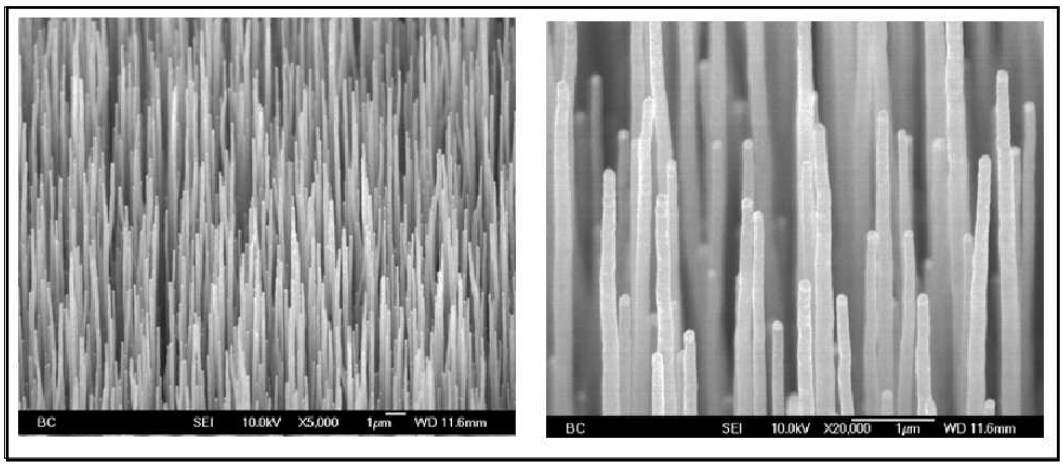

Figure 2.8: Patterned array of carbon nanotubes produced using CVD method. CVD method is well suited for the production of nanotubes in precise quantities and locations [51].

theoretical study of carbon nanotube formation suggests that a high kinetic energy (and thus a high temperature) and limited, low supply of carbon are necessary to form SWCNTs [48].

The plasma enhancement in CVD first emerged in microelectonics because certain processes cannot tolerate the high wafer temperatures of the thermal CVD operation. The plasma CVD allows an alternative at substantially lower wafer temperatures (room temperature to 100° C) for many processes and hence has become a key step in IC manufacturing [50]. The low temperature operation is possible because the precursor dissociation (necessary for the deposition of all common semiconductor, metal and insulator films) is enabled by the high-energy electrons in an otherwise cold plasma.

2.3.4 Advantages and disadvantages of various production methods

As already discussed in the previous sections, the three principal approaches to carbon nanotube fabrication are chemical vapour deposition, laser abla-

tion, and arc discharge. All currently known methods consist of some variant of one of these approaches. When considering which of the three carbon nanotube fabrication methods is best suited, one must be very clear about the criteria. It heavily depends on the application involved. Large-scale manufacturing requires that apparatus procured at a reasonable price be capable of producing significant quantities of carbon nanotubes. This rules out laser ablation, which requires significant expenditures to produce small quantities of carbon nanotubes.

For similar outlay, both CVD and arc discharge methods have been shown to be capable of producing tens or hundreds of grams of carbon nanostructures daily in each enclosure. However, the criterion of product quality demands that we strike CVD methods for the time being. Although CVD yields can be very pure, meaning that the proportion of non-carbon nanotube contaminant is low compared to the number of carbon nanotube particles, the nanostructures themselves tend to be compromised by extensive defects.

Since large-scale production requires consistent structural properties, CVD does not at present appear to be as suitable an approach as arc discharge. Therefore, the best currently known fabrication technique for large-scale nanotube manufacturing is the arc discharge process. On the other hand, if one's criteria is getting well-aligned nanotubes, the most suitable method is CVD. As it is clear from the discussion, the efficiency of a method depends heavily on the type of application for which a nanotube is intended to be produced.

Apart from the production methods discussed previously, experimentalists use variations and combinations of these methods as well to obtain high yield and purity. NASA scientists have developed a single-walled nanotube manufacturing process that does not use a metal catalyst, resulting in simpler, safer, and much less expensive production [44]. Researchers used a helium arc welding process to vapourise an amorphous carbon rod and then form nanotubes by depositing the vapour onto a watercooled carbon cathode.

Analysis showed that this process yields bundles, or ropes of single-walled nanotubes at a rate of 2 grams per hour using a single setup.

NASAs process offers several advantages over metal catalyst production methods. For example, traditional catalytic arc discharge methods produce a sample a 30% to 50% single-walled nanotube yield at a cost of approximately $100 per gram. NASAs method increased the SWCNT yield to an average of 70% while significantly reducing the per-gram production cost.

2.4 Applications of carbon nanotubes

Many potential applications have been proposed for carbon nanotubes, including conductive and high-strength composites; energy storage and energy conversion devices; sensors; field emission displays and radiation sources; hydrogen storage media; and nanometer-sized semiconductor devices, probes, and interconnects [20, 53–66]. Some of these applications are now realized in products. Others are demonstrated in early to advanced devices, and one, hydrogen storage, is clouded by controversy. Nanotube cost, polydispersity in nanotube type, and limitations in processing and assembly methods are important barriers for some applications of single-walled nanotubes.

Nanotubes have very high axial Young's modulus and tensile strength. These properties combined with the low weight and fibre-like form make nanotubes enticing candidates for composite reinforcement. Composites of nanotubes are made by dispersing nanotubes into a matrix of material that acts as the main body of the composite. The nanotubes acts as the reinforcement fibres and improve the overall mechanical strength of the composite [55]. A new advancement in this area is the production of nanotube-polymer composites [67–69].

It has been demonstrated that the mechanical properties of nanotubes can be changed significantly by filling it with other materials which has got the

added advantage that the size and shape of a nanotube remains unaffected. Molecular dynamics simulations have shown that the buckling force of single-walled carbon nanotubes is increased when filled with C_{60}, CH_4 and Ne [70].

Carbon nanotubes possess many unique properties which make them ideal AFM probes [58, 63, 65]. Their high aspect ratio provides faithful imaging of deep trenches, while good resolution is retained due to their nanometer-scale diameter. These geometrical factors also lead to reduced tip-sample adhesion, which allows gentler imaging. Nanotubes elastically buckle rather than break when deformed, which results in highly robust probes. Some of the nanotubes are electrically conductive, which allows their use in STM and EFM (electric force microscopy), and they can be modified at their ends with specific chemical or biological groups for high resolution functional imaging.

Carbon Nanotube transistors exploit the fact that nanotubes are ready-made molecular wires and can be rendered into a conducting, semiconducting, or insulating state, which make them valuable for future nanocomputer design [53,66]. Carbon nanotubes are quite popular now for their prospective electrical, thermal, and even selective-chemistry applications [57]. Interest from the research community first focused on their exotic electronic properties, since nanotubes can be considered as prototypes for a one-dimensional quantum wire [56]. In fact, if there is a special kind of defect in the honeycomb pattern of a nanotube, a single nanotube can change from being a semiconductor to being a metal as one travels along its length. This forms a Shottky barrier, a fundamental component of electrical devices.

These properties, coupled with the lightness of carbon nanotubes, gives them great potential in applications such as aerospace. It has even been suggested that nanotubes could be used in the space elevator, an Earth-to-space cable first proposed by K. E. Tsiolkovski and later scietifically investigated by Jerome Pearson [71, 72]. The electronic properties of carbon nanotubes are also extraordinary. Especially notable is the fact that nanotubes can

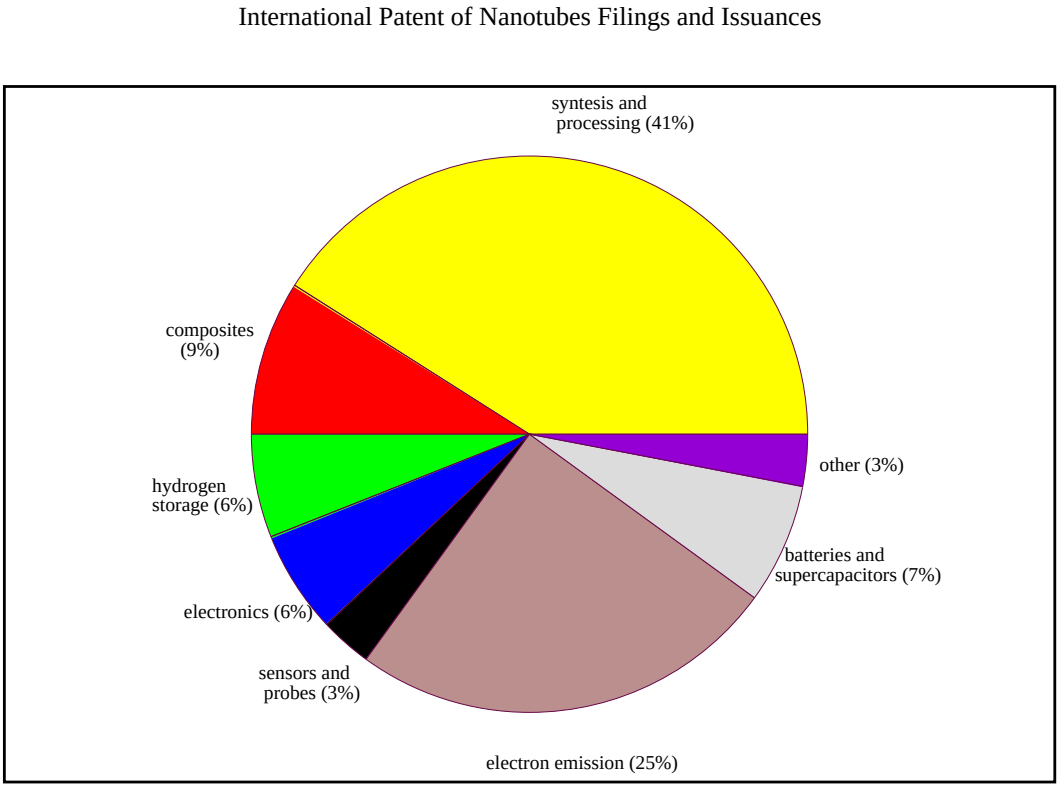

Figure 2.9: Patents filed and issued for different applications of carbon nanotubes. This figure indicates the huge variety of applications possible with carbon nanotubes [20].

be metallic or semiconducting depending on their structure. Thus, some nanotubes have conductivities higher than that of copper, while others behave more like silicon. There is great interest in the possibility of constructing nanoscale electronic devices from nanotubes, and some progress is being made in this area. However, in order to construct a useful device we would need to arrange many thousands of nanotubes in a defined pattern, and we do not yet have the degree of control necessary to achieve this.

There are several areas of technology where carbon nanotubes are already being used. These include flat-panel displays [56], scanning probe microscopes and sensing devices [54]. The unique properties of carbon nanotubes will undoubtedly lead to many more applications. Fig. 2.9 shows a list of

patents filed and issued for different applications of nanotubes. This shows the wide range of applications possible with carbon nanotubes.

3

Physical Properties of Carbon Nanotubes

Carbon nanotubes posses a wide range of interesting mechanical, electrical, thermal and chemical properties which make them unique candidates for a variety of applications. For the sake of completeness, this chapter explains most of these features in a nutshell. Since the model developed in this thesis deals with the energetics, stability and mechanical properties of carbon nanotubes, different mechanical properties are described in detail compared to other physical properties.

3.1 Mechanical properties

Carbon nanotubes possess remarkable mechanical properties, which are less sensitive to chirality than the electronic properties and hence are more easily exploited experimentally. The mechanical properties of carbon nanotubes are closely related to the properties of a graphite sheet even though the tubular anisotropy affects the behaviour of carbon nanotubes. The special properties of a graphene sheet arises from a unique feature of carbon, which is hybridization of atomic orbitals [18].

Carbon is the sixth element of the periodic table and each carbon atom has six electrons which occupy $1s^2$, $2s^2$, and $2p^2$ atomic orbitals. The four electrons in the $2s^2 2p^2$ orbitals are weakly bound valence electrons. In the free carbon atom, the energy difference between the upper $2p$ energy levels and

the lower $2s$ energy levels is approximately 4.18 eV while for a carbon-carbon double bond the binding energy is 6.36 eV [73]. Becuase of this difference in energy, the electronic wave functions for the four electrons in $2s^2 2p^2$ orbitals can readily mix with each other, thereby changing the occupation of the $2s$ and three $2p$ atomic orbitals so as to enhance the binding energy of the carbon atom with its neighbouring atoms. This mixing of $2s$ and $2p$ atomic orbitals is called hybridization, whereas the mixing of a single $2s$ electron with $n = 1, 2, 3$ $2p$ elecrons is called sp^n hybridization. Hence, in carbon three possible hybridizations occur: sp, sp^2 and sp^3.

In graphite, the carbon atoms are bonded together with sp^2 hybridization. Nanotubes are nothing but rolled graphene sheets and hence they also posses sp^2 hybridization even thought they are not pure sp^2 in nature. The extra-ordinary mechanical properties of a graphite sheet and nanotube arise from these sp^2 bonds, which are one of the strongest chemical bonds. In nanotubes the overall density of defects can be extremely low depending on the synthesising method and prevailing synthesising conditions. This has led to predictions of a very high axial strength. In fact, they are considered to be one of the strongest materials discovered so far. Different mechanical properties of carbon nanotubes are discussed in the following subsections.

3.1.1 Young's modulus (E)

Knowledge of the Youngs modulus (E) of a material is the first step towards its use as a structural element for various mechanical applications. In mechanics, Young's modulus (E) is a measure of the stiffness of an isotropic elastic material which is directly related to the cohesion of the solid and therefore to the chemical bonding of the constituent atoms. It is defined as the ratio of the uniaxial stress over the uniaxial strain in the range of stress in which Hooke's Law holds [74].

$$E = \frac{\sigma}{\epsilon} = \frac{F/A}{\Delta L/L_0} = \frac{FL_0}{A\Delta L} \tag{3.1}$$

where E is the Young's modulus, σ and ϵ are the tensile stress and tensile strain. F is the force applied to the object, A is the original cross-sectional area through which the force is applied, ΔL is the amount by which the length of the object changes and L_0 is the original length of the object. Experimentally, Young's modulus is determined from the slope of a stress-strain curve created during tensile tests conducted on a sample of the material. The Young's modulus of the best nanotubes can be as high as 1000 GPa which is approximately 5 times higher than high-carbon steel.

The fundamental atomic forces on a single-walled carbon nanotube consist of strong σ-bonding and π-bonding forces between intralayer C-C bonds. Although these forces differ from one another regarding their orders of magnitude, they are essential for describing the elastic properties of nanotubes. Elastic continuum theory has successfully been used to describe Young's modulus as well as other elastic properties of nanotubes by considereing them as elastic thin films [75]. When a single-walled carbon nanotube is considered as elastic thin film, the strain energy E_σ is inversely proportional to the diameter of of the tube, d_t: [76],

$$E_\sigma = \frac{\pi E T d_f^3}{6 d_t}, \tag{3.2}$$

where E is the Young's modulus of the sheet, T is the length of the carbon nanotube symmetry vector in the direction of tube axis (Eq. (2.7)), and d_f is the thickness of the thin film, which is normally considered as the interplanar distance between two turbostratic graphene layers (3.44 Å). The number of carbon atoms per unit cell is given by:

$$N = \frac{2\pi d_t T}{\sqrt{3}a^2} \tag{3.3}$$

Hence one obtains that the strain energy per carbon atom is inversely proportional to the square of the nanotube diameter:

$$\frac{E_\sigma}{N} = \frac{\sqrt{3}Ed_f^3a^2}{24d_t^2}. \tag{3.4}$$

This simple argument using continuum elastic theory for a dependence of E_σ/N on d_t^{-2} is confirmed by more detailed first principles calculation of the strain energies of many carbon nanotubes with different chiralities [77] which reaffirms the fact that one can assume nanotube to be an elastic thin film.

In order to obtain the Young's modulus in the perpendicular direction of tube axis, nanotube is considered to be a cantilever beam of length l. When a force is applied perpendicular to such a beam, the deflection d of the beam with a force F at its free end is given by [77, 78]:

$$d = \frac{Fl^3}{3EI} \tag{3.5}$$

where I is the moment of inertia of the cross-section of the nanotube about its axis, $I = \pi(r_o^4 - r_i^4)/4$, in which r_o and r_i are the outer and inner radii of an elastic cylinder.

Another approach towards measuring the Young's modulus of an individual nanotube is by observing the amplitude of thermal vibrations as a function of temperature [79]. At high temperature T where a classical Boltzmann distribution of probabilities, $P \infty e^{-E/k_BT}$, can be used, the average of the vibrational energy, $\langle W_n \rangle$, for a vibrational mode, n, becomes k_BT, where k_B is Boltzmann's constant. Since the averaged value of $\langle W_n \rangle$ is proportional

to the square of the amplitude u_n^2, one can write:

$$\langle W_n \rangle = \frac{1}{2} c_n \langle u_n^2 \rangle = k_B T, \tag{3.6}$$

where c_n is a spring constant. The spring constant is estimated by directly observing the amplitude of the thermal vibration as a function of temperature within the standard deviation given by statistical physics,

$$\sigma^2 = k_B T \sum_n \frac{1}{c_n} \tag{3.7}$$

The relationship between c_n and the Young's modulus E is given by use of elastic theory for continuum media [74]:

$$c_n = \frac{\pi \beta_n^4 E (r_o^4 - r_i^4)}{16 L_l^3}. \tag{3.8}$$

where the values β_n are solutions to the equation, $\cos \beta_n \cosh \beta_n + 1 = 0$.

Although the small size of carbon nanotubes present challenges for experimental characterisation, researchers have performed plenty of measurements for their mechanical characteristics. The Young's modulus and shear modulus of a typical nanotube are calculated and is found to be comparable to those of diamond [80, 81]. The first Young's modulus measurement by Treacy and coworkers [79] confirmed this. They related thermal vibration amplitudes of multi-walled nanotubes to their Young's modulus and obtained an average value of 1.8 TPa with a large spread. After that, measurements using AFM techniques obtained values 1.28 ± 0.59 TPa for nanotubes produced using arc-discharge method [63]. Poncharal *et al.* induced vibrations on multi-walled nanotubes by alternating electric potential and measured the vibrational frequencies and hence obtained values for Young's modulus between 0.7 TPa and 1.3 TPa for tubes with diameter less than 12nm and between 0.1 TPa and 0.3 TPa for thicker tubes [82]. This large drop is ex-

plained by an onset of a wavelike bending mode of the nanotube. Because of their small diameter and their tendency to bundle, performing measurements on single-walled nanotubes are more complicated. Krishnan *et al.* report in Ref. [83] a measurement of individual single-walled carbon nanotube using thermal vibration method of Ref. [79] and they obtain an average value of 1.25 TPa. Salvetat *et al.* studied the stress-strain curve of multi-walled carbon nanotubes using atomic force microscopy [84] and Fig. 5.46 shows the force deflection characteristics they obtained. From the slope of this curve, they calculated the value of Young's modulus as 0.8 TPa. Although the current measurements suffer from inaccuracies due to vibration amplitude measurement and assumptions made on AFM tip characteristics, the current agreement is that both single-walled and multi-walled nanotubes have a Young's modulus value around 1 TPa.

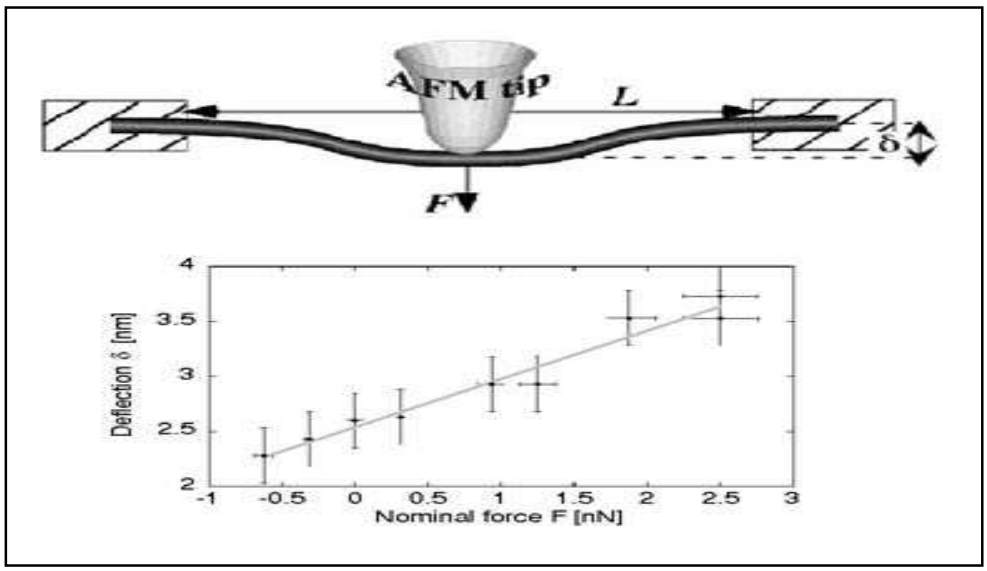

Figure 3.1: Force-deflection curve obtained by atomic force microscopy for a multi-walled carbon nanotube. The slope of this curve gives a Young's modulus of 0.8 TPa [84].

Theoretical studies of axial Young's modulus are done mostly on single-walled nanotubes because the intertube interactions are very weak in multi-

walled nanotubes and thus less important in estimating axial mechanical properties. Theoretical calculations for individual single walled nanotubes have been performed and they reported around 1 TPa or slightly higher for axial Young's modulus [80, 85]. In Ref. [80] Lu estimates the axial Young's modulus values for both single-walled and multi-walled nanotubes as 0.97 TPa to 1.11 TPa. All theoretical calculations are performed on pristine nanotubes but the measurements are performed on real nanotubes with defects. Still there is excellent agreement between theoretical estimates and actual measurements. This can be understood from the fact that the point defects have little influence on the Young's modulus [86].

3.1.2 Tensile strength

Tensile strength denotes the ability to bear strain without undergoing plastic deformation. As the size of the system reduces the measurement of this quantity suffer from difficulties and inaccuracies and hence in the case of nanotubes this measurement is hard to achieve. Nevertheless, people have already measured this and reported values ranging from 11 GPa to 63 GPa [87] for multi-walled nanotubes which is around 50 times higher than high-carbon steel. In this measurement [87], the contact was only to the outmost layer of the multi-walled tube and a sword and sheath type of failure of this layer was reported. The experimental value of tensile strength of individual single-walled nanotubes is still an open question but for bundles of single-walled nanotubes, tensile strength values ranging between a few GPa and several tens of GPa depending on the bundle and measurement characteristics, have been reported [88–90]. Fig. 3.2 compares the tensile strengths of some engineering materials with that of carbon nanotube. This figure shows that the tensile strength of carbon nanotubes are very high compared to other day to day engineering materials which makes them a promising candidate as reinforcements.

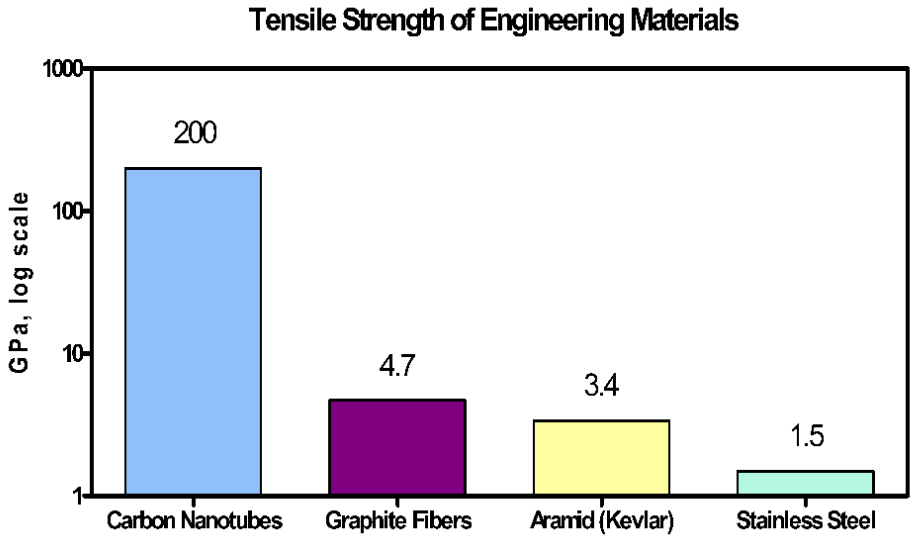

Figure 3.2: Comparing tensile strengths of different engineering materials. The tensile strength of carbon nanotubes greatly exceeds that of other high-strength materials. Note that each increment on the vertical axis is a power of 10 [91].

The measured values of tensile strengths for nanotubes fall short of the theoretical predictions which are very high [92–95]. This discrepancy arises both from the limitations in the theoretical description and from the presence of imperfections in the structure. The limitations in the theoretical descriptions include restricted time scales of simulation and model-related limitations, such as cut off [93]. Sammalkorpi *et al.* show that even a single point-like structural imperfection in an otherwise perfect nanotube can deteriorate the mechanical strength to a fraction [86].

For comparison purpose, average values of the Young's modulus, density and tensile strength of both single-walled and multi-walled carbon nanotubes are listed with that of some other materials like diamond, steel and wood in Tab. 3.1. The uniqueness of the mechanical properties of carbon nanotubes are evident from this table.

Material	Young's Modulus (GPa)	Tensile Strength (GPa)	Density (g/cm^3)
Single-wall nanotube	1054	150	1.4
Multi-wall nanotube	1200	150	2.6
Diamond	600	130	3.5
Kevlar	186	3.6	7.8
Steel	208	1.0	7.8
Wood	16	0.008	0.6

Table 3.1: Comparison of the mechanical properties of single-walled and multi-walled carbon nanotubes with some engineering materials. Nanotubes are found to be the strongest materials ever discovered [96].

3.1.3 Structural phase transitions

Another very important feature of carbon nanotubes is their softness to lateral forces. There are studies using molecular dynamics methods which show that under axial compression, a single-walled nanotube buckles and eventually undergoes shape changes [97]. These shape changes results in an abrupt release of energy and a singularity in the stress-strain curve [75], which can be treated as a structural phase transition in carbon nanotubes.

Fig. 3.3 shows the strain energy curve as a function of the deformation parameter ϵ for a nanotube of length $L = 6$ nm, diameter $d = 1$ nm and chirality $n = 7, m = 7$ obtained by molecular dynamics simulations. Each figure on the left hand side of the graph stands for the structure of the nanotubes at the marked singularity in the energy curve, which in turn clearly shows that a structural transition of the nanotube takes place at each singularity. High-pressure x-ray-diffraction experiments on pristine nanotubes show that these nanotubes become partially amorphous when compressed above 8 GPa [98]. The structural phase transitions can be enhanced by filling the nanotubes with metals like Fe. Karmkar *et al.* [99] studied the pressure induced phase

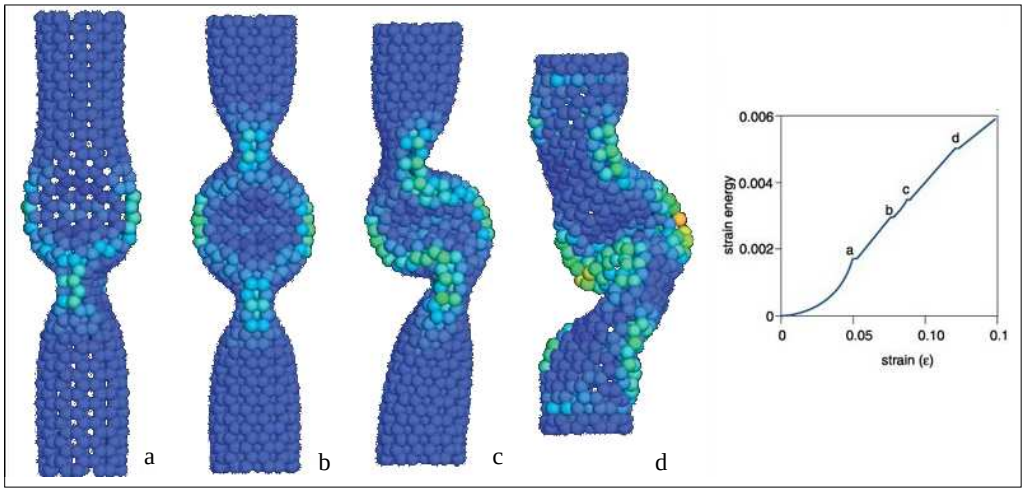

Figure 3.3: Molecular dynamics simulation of a nanotube of length $L = 6$ nm, diameter $d = 1$ nm, and chirality $n = 7, m = 7$ under axial compression. Here ϵ is the deformation parameter. The strain energy displays four singularities corresponding to shape changes. At $\epsilon = 0.05$ the cylinder buckles into the pattern (a), displaying two identical flatteningsfins perpendicular to each other. Further increase of ϵ enhances this pattern gradually until at $\epsilon = 0.076$ the tube switches to a three-fin pattern (b), which still possesses a straight axis. In a buckling sideways at $\epsilon = 0.09$ the flattenings serve as hinges, and only a plane of symmetry is preserved (c). At $\epsilon = 0.13$, an entirely squashed asymmetric configuration forms (d) [75].

transitions in iron-filled multi-walled carbon nanotubes using x-ray diffraction method and observed a sharp change in the average intertubular distance at ~ 9 GPa. They also reported that there are no such structural changes observed for a pristine multi-walled carbon nanotube. Similar studies have been performed in single-walled nanotubes as well. Peters *et al.* [100] did high-pressure Raman spectroscopy study of single-walled carbon nanotube bundles and found that they undergoes a structural phase transition at approximately 1.7 GPa. The bundles they used composed of nanotubes with chiralities $(10, 10)$ and $(17, 0)$. Molecular dynamic simulations performed with the same group confirmed this phase transition.

Although structural phase transitions in nanotubes has been studied with

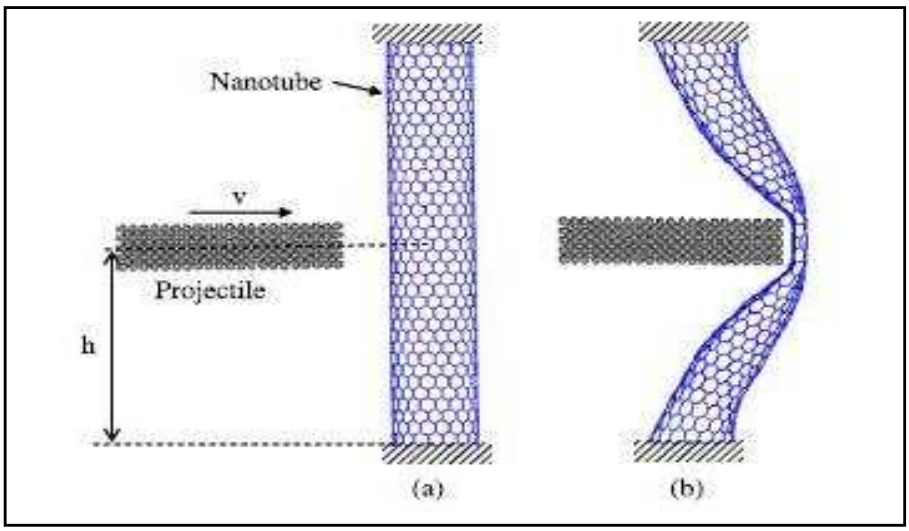

Figure 3.4: Figure illustrating the elastic flexibility of carbon nanotubes. (a) Initial state, (b) deformed nanotube after ballistic impact at its maximum energy absorption. This property makes carbon nanotubes potential candidates for ballistic resistance materials [101].

a variety of experimental techniques and they agree in some form of change in the phase, there is remarkable disagreement in the proposed transition pressures as well as the nature of the new phase [99, 100, 102, 103]. To clarify this, theoretical studies are performed using empirical [100, 104] and semi-empirical [105, 106] to first-principles methods [107–109]. However, the results of the theoretical studies varied greatly with the specific nanotube under study and the applied method. Reich *et al.* studied chiral and achiral single-walled nanotubes using *ab-initio* calculations and found that the pressure corresponding to the structural phase transition heavily depends on the chirality of the tube, which in part explained the contradicting results [110].

Carbon nanotubes have high elastic flexibility for a wide range of practical conditions and hence show substantial promise for structural and fibre applications [63,112]. Fig. 3.4 and Fig. 3.5 illustrates this elastic flexibility of carbon nanotubes. In Fig. 3.4, ballistic resistivity, a special property based on the elastic flexibility of carbon nanotubes is illustrated. This property enables

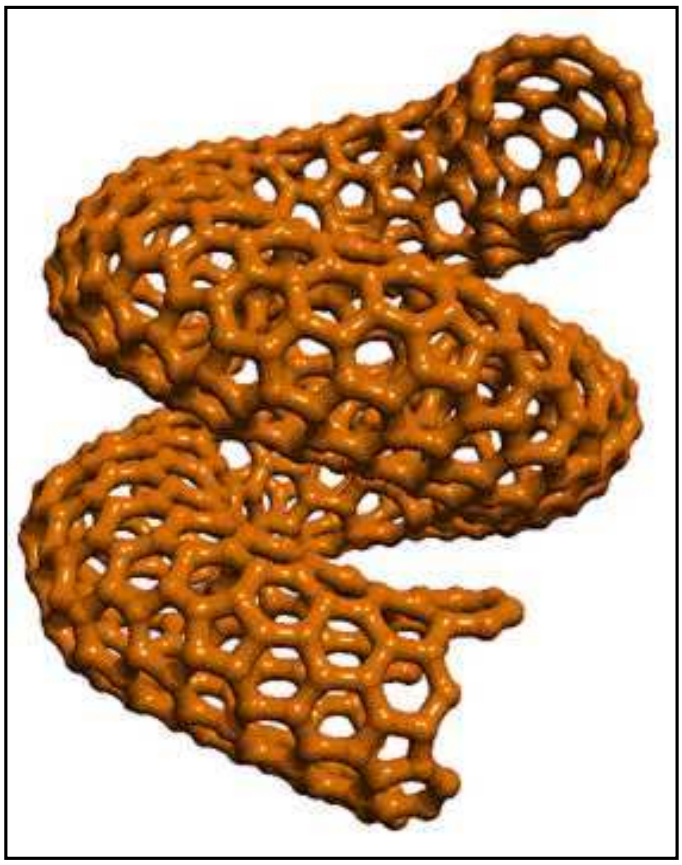

Figure 3.5: A helical carbon nanotube which illustrates the elastic flexibility of nanotubes. The model developed in this thesis could be extened to study such systems [111].

carbon nanotubes to be used as a bullet proof material. Fig. 3.5 illustrates a helical nanotube. Such systems are getting wider attention these days because of the discovery that mechanical strain leads to considerable changes in the the electrical properties of carbon nanotubes [113]. The energetics of such systems can be studied by extending the model developed in this thesis. By high resolution electron microscopy (HREM) and using molecular dynamic simulations, Iijima and coworkers observed fully reversible bending of carbon nanotubes to very large bending angles, despite the occurrence of kinks and highly strained tube regions. They reported that this arises due to the remarkable flexibility of the hexagonal network in the nanotube, which

resists bond breaking and bond switching up to very high strain values [112]. Although carbon nanotubes have high elastic flexibility, under extreme stress, they fail. The failure mechanism is studied in both the slow and fast stress application limits. In slow stress limit, local defects are found to be formed, where four neighbouring hexagons on the surface of the tube are replaced by two pentagons and two heptagons [114]. Under fast deformations, the hexagons in the tube elongate until the breaking point and a crack forms circumferentially around the tube wall [114]. On increasing the stress, two or more single carbon strands are found to appear [94].

3.1.4 Low friction surfaces

Multi-walled nanotubes have a very special property which make them potential candidates as constituents of nanometer-scale mechanical devices. It is the ability of their surfaces to rotate or slide with respect to each other almost frictionless. This has already been demonstrated theoretically [115–119] and experimentally [120–122]. The reason for these frictionless rotation and sliding is the very weak van der Waals type interaction between them [123]. Experimentalists have succeeded in using this property to develop linear bearings with ultra-low friction [121] and nanoscale electromechanical devices [124]. These properties can also be utilised in multi-walled nanotube based oscillators [116, 117, 119, 125] with operating frequencies up to several gigahertz.

3.2 Other properties

The model developed in this thesis is applicable to the mechanical properties of single-walled carbon nanotubes. Previous section describes mechanical properties of nanotubes in a detailed manner. Although these unusual mechanical properties played a major role for carbon nanotubes in getting their

wide attention from the research community, they were not the only reason. In fact nanotubes posses a wide range of unusual interesting properties. For the sake of completeness, other interesting properties of carbon nanotubes are described below.

3.2.1 Electronic properties

The electronic structure of carbon nanotubes is unique in material science. It arise directly from the properties of graphite constrained in two dimensions. Graphite possesses valence and conduction bands that are very close to each other in energy [126,127]. Hence, the electronic structure that results when such a sheet is rolled is highly sensitive to the manner in which it is rolled. Depending on the way of rolling, the nanotubes can be metallic or semiconducting [18,128–130] which means the conductivity of a single-walled nanotube is governed by its electronic structure which is determined by the chiral indices (n, m). A very minor change in the structure can determine whether the tube is semiconducting or metallic.

For multi-walled nanotubes, the situation is more complex because the multiple layers contribute to the conductivity. Currently, most of the interest in the nanotube electronic transport focuses on individual tubes and the main interest is in devices based on individual tubes. The tubes show both ballistic and diffusive transport character depending on the level of perfection of the tubes. Single-walled nanotubes are more ballistic while multi-walled nanotubes are diffusive because of higher defect concentration. The theoretical prediction [18, 130] of both metallic and semiconducting tubes is consistent with several experiments [129, 131, 132].

Carbon nanotubes exhibit electron localisation caused either by contacts or by defects in tubes. Hence they are of much interest for basic studies of quantum transport [133]. There are studies done which predicts

that nanotubes can be used as high temperature super conducting materials [134]. Experimentalists have already produced nanotube transistors exhibiting current-voltage characteristics resembling that of silicon based metal oxide semiconductor field effect transistor (MOSFET) [128]. Although it is rather difficult to dope a carbon nanotube, there are theoretical and experimental studies performed on nanotubes doped with Si, B, Ni, Co and N [135–139]. It is found that doping a semiconducting nanotube with Si introduces a localised level located approximately 0.6 eV above the top of the valence band, whereas for the metallic nanotube, it introduces a resonating level close to 0.7 eV above the Fermi level [135]. Experiments show that the resistance of a nanotube lowers as it is doped with B [136].

Electronic structure

The electronic structure of a single-walled carbon nanotube can be derived by a simple Slater-Koster or Hükel tight-binding calculation for the π-electrons of carbon atoms [17]. This is obtained from that of two-dimensional graphene sheet by using periodic boundary conditions in the circumferencial direction denoted by the chirality vector $\vec{C_h}$. The basis functions for two-dimensional graphene is obtained by two Bloch functions, constructed from atomic orbitals for two in equivalent carbon atoms. The diagonal elements of the Hamiltonian are given by:

$$H_{AA} = H_{BB} = \epsilon_{2p} \tag{3.9}$$

where ϵ_{2p} is the orbital energy of the 2p level. If $\mathbf{R_1}$, $\mathbf{R_2}$ and $\mathbf{R_3}$ are the position vectors of three nearest-neighbour carbon atoms of a given atom, then the off-diagonal matrix elements of the Hamiltonian are given by:

$$H_{AB} = t(e^{i\mathbf{k}.\mathbf{R_1}} + e^{i\mathbf{k}.\mathbf{R_2}} + e^{i\mathbf{k}.\mathbf{R_3}}) = tf(k). \tag{3.10}$$

where t is given by:

$$t = \langle \phi_A(r - R)|H|\phi_B(r - R \pm a/2)\rangle. \tag{3.11}$$

where a is the distance between two carbon atoms in the graphene sheet. Since $f(k)$ is a complex function and the Hamiltonian forms a Hermitian matrix, $H_{BA} = H^*_{AB}$. One can define the overlap integral matrix, S, as:

$$s = \langle \phi_A(r - R)|\phi_B(r - R \pm a/2)\rangle. \tag{3.12}$$

The explicit forms of H and S can be written as:

$$H = \begin{pmatrix} \epsilon_{2p} & tf(k) \\ tf(k)^* & \epsilon_{2p} \end{pmatrix}, S = \begin{pmatrix} 1 & sf(k) \\ sf(k)^* & 1 \end{pmatrix} \tag{3.13}$$

Using H and S in Eq. (3.13) and solving the secular equation $det(H - ES) = 0$, the eigenvalues $E(\mathbf{k})$ are obtained as a function of $\omega(\mathbf{k})$, k_x and k_y.

$$E_g(\mathbf{k}) = \frac{\epsilon_{2p} \pm t\omega(\mathbf{k})}{1 \pm s\omega(\mathbf{k})} \tag{3.14}$$

where the + sign in the numerator and denominator go together giving the bonding π energy band, and likewise for the $-$ signs, which give the anti-bonding π^* band, whie the function $\omega(\mathbf{k})$ is given by:

$$\omega(\mathbf{k}) = \sqrt{|f(\mathbf{k})|^2} = \sqrt{1 + 4\cos\frac{\sqrt{3}k_x a}{2}\cos\frac{k_y a}{2} + 4\cos^2\frac{k_y a}{2}} \tag{3.15}$$

Using the periodic boundary conditions for the dispersion relation for two-dimensional graphene, one arrives at the energy dispersion relation for single-walled carbon nanotube as:

$$E_{cnt}(k) = E_g(k\frac{\mathbf{K_2}}{|\mathbf{K_2}|} + \mu\mathbf{K_1}) \tag{3.16}$$

where $\mu = 0, 1, ..., N-1$ and $\frac{-\pi}{T} < k < \frac{\pi}{T}$.

The electronic structures of single-walled carbon nanotubes are chiefly characterized by their chiral indices n and m [140,141]. Besides the chirality, curvature also influences the electronic structures of single-walled carbon nanotubes. The π electron states of single-walled nanotubes are rehybridized with the σ electron states. This rehybridization gives rise to a curvature dependent downward shift of the π states: the greater the curvature, the greater the downward shift. Due to this stronger $\pi - \sigma$ rehybridization, thin single-walled nanotubes becomes metallic [142].

One of the earliest theoretical studies on the electronic properties of carbon nanotubes is done by Tanaka *et al.* [143] using one-dimensional tight-binding crystal orbital method, where they found that depending on the chirality of the nanotube it can either be semiconducting or metallic in nature. A nanotube of chirality (n, m) is metallic if $(2n + m)$ is a multiple of 3. Fig. 3.6 shows which carbon nanotubes are semiconducting and which are metallic, denoted by dots and circled dots, respectively. From figure, it follows that approximately one third of the carbon nanotubes are metallic and the other two thirds are semiconducting. Wildöer *et al.* confirmed the theoretical predictions on the electronic structure of carbon nanotubes. They used scanning tunnelling microscopy and spectroscopy to obtain atomically resolved images of individual single-walled nanotubes and using these examined the electronics properties as a function of tube diameter and chiral angle. They also observed sharp van Hove singularities in the density of states at the onset of one-dimensional energy bands, confirming the strongly one-dimensional nature of conduction within nanotubes.

The energy gap for a semiconducting nanotube is directly observed by scanning tunnelling microscopy and is found of the order of ~ 0.5 eV. This gap is inversely proportional to the diameter of the tube and is given by

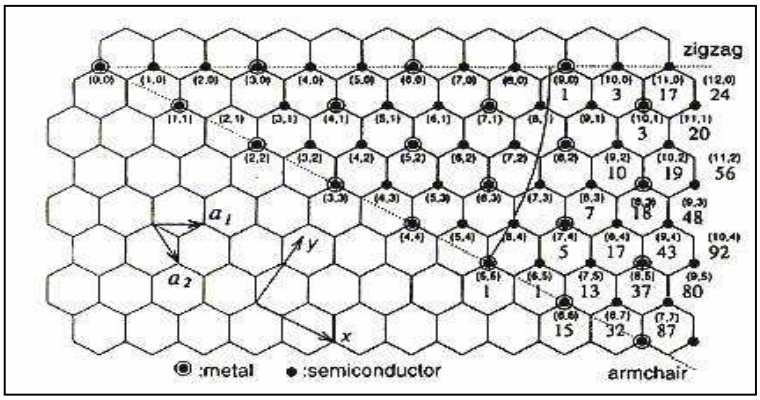

Figure 3.6: Distribution of metallic and semiconducting nanotubes with respect to chiral indices [18]. Dots represent semiconducting tubes and circled dots represent metallic tubes.

[18, 144]:

$$E_{gp} = \frac{2a\gamma}{d} \tag{3.17}$$

where γ is the carbon-carbon tight-binding overlap energy, a is the nearest neighbour carbon-carbon distance and d is the diameter of the tube. Recently, it has been established that energy levels, energy gap and the density of states of a multi-walled nanotube strongly depend on the symmetry configurations, the nanotube length and the transverse electric field applied. Moreover, it has been shown that the intertube interactions in a multi-walled nanotube vary the level spacing and energy gap [145].

3.2.2 Thermal properties

The thermal conductivity of carbon nanotubes is dependent on the temperature and the large phonon mean free paths. On the graph of thermal conductivity vs temperature (Fig. 3.7), the slope of the line at low temperatures can be modelled using the heat capacity, sound velocity, and relaxation time of the tube.

Although there is disagreement about the exact nature of the thermal

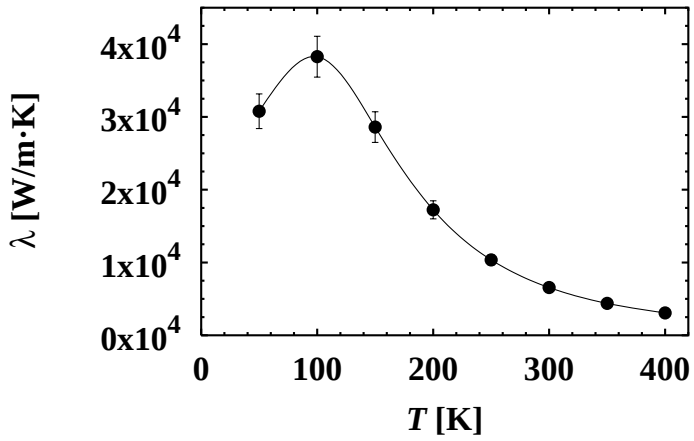

Figure 3.7: Temperature dependends of the thermal conductivity λ for a $n = 10$, $m = 10$ carbon nanotube for temperatures below 400 K [146].

conductivity of nanotubes, most researchers agree it is temperature based, and possibly current and vacancy concentration based. In 1999, J. Hone, M. Whitney, and A. Zettle discovered that the thermal conductivity was related to temperature and was almost linear from 7 K to 25 K, although the relationship sloped slightly from 25K to around room temperature [147]. However, a later group studied the same relationship and instead of confirming a linear relationship, found the slope to drop dramtically from 100 K to 400 K. Also that year, Che, Cagin, and Goddard [148] numerically calculated the thermal conductivity of a (10, 10) nanotube to approach 2980 W/m-K as the current applied to it is increased. In 2000, Berber, Kwon, and Tomanek [146] determined the thermal conductivity of carbon nanotubes and its dependence on temperature. They confirmed the suggestion of Hone *et al.* in 1999 by suggesting an unusually high value of 6,600 W/m-k for the thermal conductivity at room temperature. They theorised that these high values would be due to the large phonon mean free paths, which would concur with Hone's model. Both groups stated that these values for thermal conductivity are comparable to diamond or a layer of graphite. However, Berber *et al.* suggested that

the graphs of the temperature dependence of thermal conductivity looked much less linear than previously proposed by Hone *et al.* Instead of a near-linear graph with a positive slope, their graph showed a positive slope from low temperatures up to 100K, where it peaks around 37,000 W/m-K. Then, the thermal conductivity drops dramatically down to around 3000 W/m-k when the temperature approaches 400 K. However, both groups found the thermal conductivity of nanotubes to be unusually high at room temperature and confirmed that the values for nanotubes are comparable to those for diamonds and graphite.

3.2.3 Optical properties

In 1998, Wildöer *et al.* [144] conducted research into the fundamental gap of carbon nanotubes. The study by Wildöer *et al.* showed that nanotubes of type $n - m = 3l$, where l is zero or any positive integer, were metallic and therefore conducting. The fundamental gap (HOMO-LUMO) would therefore be 0.0 eV. All other nanotubes, they showed, behaved as a semiconductor. The fundamental gap, they showed, was a function of diameter, where the gap was in the order of about 0.5 eV. This shows that the fundamental gap ranged from around 0.4 eV - 0.7 eV, which they said was in good agreement with the values obtained from one-dimensional dispersement relations. They concluded that the fundamental gap of semi-conducting nanotubes was determined by small variations of the diameter and bonding angle.

In a study published at the same time by Odom, Huang, and Lieber they suggested that a small gap would exist at the Fermi level in metallic nanotubes. This would be because of the bonding orbitals and anti-bonding orbitals mixing due to the curvature in the graphene sheet of a single-walled nanotube. They noted, however, that they had not observed any evidence to support this as of the time of publishing (1998). More interesting to note,

in the study by Wildöer *et al.*, they reported that the conducting nanotubes shows E_{gap} to range from 1.7 - 2.0 eV, which could be the evidence Odom *et al.* was predicting. At the Fermi Energy (the highest occupied energy level), the density of states is finite for a metallic tube (though very small), and zero for a semi-conducting tube. As energy is increased, sharp peaks in the density of states, called Van Hove singularities, appear at specific energy levels.

3.3 Defects and their influence on physical properties

Extensive studies has been performed on the defects in nanotubes and their influence on various properties of nanotubes [18, 86, 149–153]. There are various sources behind the generation of defects in nanotubes. Generally, they are generated in the synthesising process. Other possible causes are irradiation of the tube with ion or electron beam and mechanical manipulation. Although methods are developed to synthesis high quality nanotubes, it is extremely difficult to produce a defectless nanotube. The most typical structural defects are pentagonal and heptagonal rings in the hexagonal lattice of the nanotube. Other types of typical defects are vacancies, interstitial and miscellaneous bonding configurations such as locally amorphous structure. There may arise non-carbon based defects, in which substitutional atoms or atom groups appear. Defects may alter the straightness of a tube and can result in a curvature, bulging, kinked, spiral form [18]. See Fig. 3.8, where a pentagonal and septagonal defect in a nanotube introduces curvature to the whole tube.

From a purely mechanical point of view, defects are rarely desirable as they make the tube less strong. At the same time, defects help in manipulating the mechanical properties of nanotubes. It has been already shown that

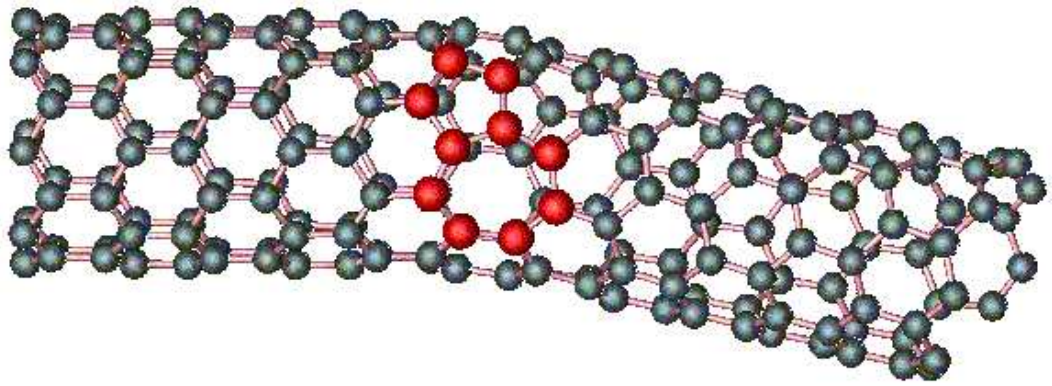

Figure 3.8: Figure illustrating the effect of a defect in the geometry of a nanotube [154]. Here, a pentagonal and septagonal defects are marked in red colour. These defects introduce curvature to the whole tube.

defects can be employed to improve load transfer between the low-friction surfaces of the nanotubes [86, 149, 150]. This enables improved mechanical properties for applications such as nanoelectromechanical devices or polymer composites in which the tube-tube-slippage may be detrimental.

The effects of defects in carbon nanotubes on their conductivity is studied extensively [151–153, 155]. Defects in all carbon nanotubes act as local scattering centres for charge carriers. The scattering effects of isolated point-defects decreases with an increasing diameter of the nanotube because they are averaged over the circumference [151]. Hence, their influence is small for all but very thin nanotubes. However, if the defects or deformations accumulate locally, a tunnelling barrier may form [155]. Two tunnelling barriers close to each other in a thin wire such as a nanotube form a single electron transistor. This has been exploited in experiments where sharp bends [156, 157] and ion [155] irradiation have been employed for forming tunnelling barriers.

4

Theoretical Approaches to the Energetics of CNTs

A rigorous calculation of the properties of any system at the atomic scale is based on solving the many body time dependent Schrödinger equation and obtaining the many body wave function $\Psi(r_1, ..., r_n, t)$. Unfortunately, exact analytical solutions exist only for a handful of cases such as the hydrogen atom and the harmonic oscillator. Numerically the problem is intractable for systems containing more than a few hundred particles. The exponentially rising demand of computational resources ensures that exact quantum mechanics is not to be considered as a way to solve such problems. Research community has to rely on approximations of various orders of the Schrödinger equation and even on totally classical empirical approaches.

This chapter contains an overview of the approximations on materials simulation methods at atomic scale. This overview is presented in Section 4.1. In this thesis the emphasis is on empirical carbon modelling by the Tersoff and Brenner interaction potentials [158, 159]. Therefore these two potentials are discussed in detail in the later section.

4.1 Introduction

The methods of modelling the atomic interaction can roughly be divided into three categories: The first principle, or *ab initio,* methods are the most rigorous ones. Only a few well controlled approximations to exact quantum

mechanics are made. Semiempirical methods contain more drastic approximations and may also contain empirically defined parameters. Empirical methods are a group of methods that are tuned to reproduce an empirically defined fitting set. The three categories, their drawbacks and benefits, and the most popular methods of each are briefly described in this section.

4.1.1 First principles methods

The most rigorous approach to problems of condensed matter physics are the first principles methods. They do not employ any empirical parameters in the calculation. The results are based on quantum mechanics and well controlled approximations. The essence of first principle methods is solving the many body Schrödinger equation. For a many electron system the corresponding Schödinger equation is given by:

$$\hat{H}\Psi = \sum_{i=1}^{N}(\frac{-\hbar^2}{2m}\nabla_i^2\Psi - e^2\sum_R \frac{1}{|\mathbf{r_i}-\mathbf{R}|}\Psi) + \frac{1}{2}\sum_{i\neq j}\frac{e^2}{|\mathbf{r_i}-\mathbf{r_j}|}\Psi = E\Psi \quad (4.1)$$

where $\Psi = \Psi(\mathbf{r_1}, \mathbf{r_2}, ..., \mathbf{r_N})$ is the N-particle wave function of all the electrons in the system, the negative potential energy term represents the attractive electrostatic potential of the nuclei fixed at the points R, and the last term represents the interaction of the electrons with each other.

The two most used first principle methods are Hartree-Fock method [160] and the density functional theory [161,162]. A short review of these methods are given in the following paragraphs. Since first principle methods rely on quantum mechanics, they are highly accurate but the system size that can be handled is restricted to at most a couple of hundred atoms.

Solving an equation such as Eq. (4.1) is impossible without making some simplifying physical ideas. In Hartree approach the quantum mechanical N-electron many body wave function ($\Psi(\mathbf{r_1}, \mathbf{r_2}, ..., \mathbf{r_N})$) is approximated by a

product of single electron wave functions, *i.e.*,

$$\Psi(\mathbf{r_1}, \mathbf{r_2}, ..., \mathbf{r_N}) = \psi_1(\mathbf{r_1})\psi_2(\mathbf{r_2})...\psi_N(\mathbf{r_N}). \tag{4.2}$$

Given this assumption, the Hartree equation for the N-electron many body system is obtained by getting a proper choice of the potential $U(\mathbf{r})$ appearing in the one-electron Schrödinger equation:

$$\frac{-\hbar^2}{2m}\nabla^2\psi(\mathbf{r}) + U(\mathbf{r})\psi(\mathbf{r}) = \varepsilon\psi(\mathbf{r}) \tag{4.3}$$

Evidently, $U(\mathbf{r})$ should include the potentials of the ions in the system:

$$U^{ion}(\mathbf{r}) = -e^2 \sum_R \frac{1}{|\mathbf{r} - \mathbf{R}|}. \tag{4.4}$$

In addition, $U(\mathbf{r})$ must incorporate the fact that each electron feels the electric fields of all other electrons in the system. Hartree treated the remaining electrons as a smooth distribution of negative charges with charge density ρ. Now, the potential energy of a given electron in the field of all other electrons is given by:

$$U^{el}(\mathbf{r}) = -e \int d\mathbf{r}'\rho(\mathbf{r}')\frac{1}{|\mathbf{r} - \mathbf{r}'|}. \tag{4.5}$$

To actually calculate the Hartree potential $U(\mathbf{r})$, it is necessary to know the electronic charge distribution of the system. If the electrons are assumed to be independent of each other, then it is straightforward to construct $\rho(\mathbf{r})$ from the single electron eigenstates:

$$\rho(\mathbf{r}) = -e \sum_i |\psi_i(\mathbf{r})|^2. \tag{4.6}$$

where the sum extends over all occupied one-electron levels in the system. Placing Eq. (4.6) in Eq. (4.5) and letting $U = U^{ion} + U^{el}$, we arrive at the

one-electron equation:

$$\frac{-\hbar^2}{2m}\nabla^2\psi_i(\mathbf{r}) + U^{ion}(\mathbf{r})\psi_i(\mathbf{r}) + \left[e^2\sum_j \int d\mathbf{r}'|\psi_j(\mathbf{r}')|^2\frac{1}{|\mathbf{r}-\mathbf{r}'|}\right]\psi_i(\mathbf{r}) = \varepsilon_i\psi_i(\mathbf{r}). \tag{4.7}$$

The set of equations Eq. (4.7) is known as the Hartree equations. These non-linear equations for the one-electron wave functions and energies are solved by iteration as follows. A form is guessed for U^{el} (the term in brackets in Eq. (4.7)) and on the basis of which the equations are solved. From the resulting wave functions, $\psi_i(\mathbf{r})$, a new U^{el} is computed and a new Schrödinger equation is solved. The iteration is continued until further iterations do not alter the potential.

The Hartree wave function (Eq. (4.2)) is incompatible with the Pauli exclusion principle, which states that the total wavefunction for the system must be antisymmetric under particle exchange. This means that when two arguments are swapped the wavefunction changes sign as follows:

$$\Psi(\mathbf{r_1}, \mathbf{r_i}, ..., \mathbf{r_j}, \mathbf{r_N}) = -\Psi(\mathbf{r_1}, \mathbf{r_j}, ..., \mathbf{r_i}, \mathbf{r_N}). \tag{4.8}$$

where $\mathbf{r_i}$ includes coordinates of position and spin. Hartree-Fock approximation is an extension of the Hartree approximation to include the permutation symmetry of the wavefunction which leads to the exchange interaction. This is done by adding Fermi-Dirac statistics by replacing the product of the wave functions by the Slater determinant of one-electron wave functions [160]. Thus the new wave function includes the linear combination of the products pf one-electron wave functions as in Eq. (4.2) and all other products obtained from it by permutation of the $\mathbf{r_j}$ among themselves added together

with weights +1 or -1 so as to guarantee condition Eq. (4.8).

$$\Psi(\mathbf{r_1}, \mathbf{r_2}, ..., \mathbf{r_N}) = \begin{vmatrix} \psi_1(\mathbf{r_1}) & \psi_1(\mathbf{r_2}) & . & . & . & \psi_1(\mathbf{r_N}) \\ \psi_2(\mathbf{r_1}) & \psi_2(\mathbf{r_2}) & . & . & . & \psi_2(\mathbf{r_N}) \\ . & . & & & & . \\ . & . & & & & . \\ \psi_N(\mathbf{r_1}) & \psi_N(\mathbf{r_2}) & . & . & . & \psi_N(\mathbf{r_N}) \end{vmatrix}. \quad (4.9)$$

Assuming that the single electron wave functions, $\psi_1, ...\psi_N$, are orthonormal, the expectation value of the Hamiltonian in this state is obtained as:

$$\begin{aligned} \langle H \rangle_\Psi &= \sum_i \int d\mathbf{r} \psi_i^*(\mathbf{r}) \left(\frac{-\hbar^2}{2m} \nabla^2 + U^{ion}(\mathbf{r}) \right) \psi_i(\mathbf{r}) \\ &+ \frac{1}{2} \sum_{i,j} \int d\mathbf{r} d\mathbf{r}' \frac{e^2}{|\mathbf{r} - \mathbf{r}'|} |\psi_i(\mathbf{r})|^2 |\psi_j(\mathbf{r}')|^2 \\ &- \frac{1}{2} \sum_{i,j} \int d\mathbf{r} d\mathbf{r}' \frac{e^2}{|\mathbf{r} - \mathbf{r}'|} \delta_{s_i s_j} \psi_i^*(\mathbf{r}) \psi_i(\mathbf{r}') \psi_j^*(\mathbf{r}') \psi_j(\mathbf{r}). \quad (4.10) \end{aligned}$$

Minimising Eq. (4.10) with respect to ψ_i^* leads to the Hartree-Fock equations:

$$\begin{aligned} \frac{-\hbar^2}{2m} \nabla^2 \psi_i(\mathbf{r}) &+ U^{ion}(\mathbf{r}) \psi_i(\mathbf{r}) + U^{el}(\mathbf{r}) \psi_i(\mathbf{r}) \quad (4.11) \\ &- \sum_j \int d\mathbf{r}' \frac{e^2}{|\mathbf{r} - \mathbf{r}'|} \psi_j^*(\mathbf{r}') \psi_i(\mathbf{r}') \psi_j(\mathbf{r}) \delta_{s_i s_j} = \varepsilon_i \psi_i(\mathbf{r}) \end{aligned}$$

These equations differ from the Hartree equations, Eq. (4.7), by an additional term on the left side, known as the exchange term. The exchange term is nonlinear in ψ and is an integral operator which makes the complexity introduced by the exchange term considerable. In its most rigorous form, the Hartree-Fock method can be used on systems of a few hundreds of atoms. Even though the Hartree-Fock method is not always extremely accurate, it is much used. The accuracy can be enhanced but this increases the consumption of CPU-time [163].

Density Functional Theory (DFT) [161,162] is based on using the electron probability density $n(\mathbf{r})$ of the system as the basic variable. The Hohenberg-Kohn theorem [161] serves as the base of DFT. According to this theorem, the ground-state energy and all other ground-state electronic properties of a system are uniquely determined by the electron probability density $n(\mathbf{r})$. Unfortunately, the Hohenberg-Kohn theorem does not tell us the form of the functional dependence of energy on the density: it proves only that such a functional exists. The next major step in the development of DFT came with the derivation of a set of one-electron equations from which the electron density $n(\mathbf{r})$ could be obtained [162]. W. Kohn and L. J. Sham showed that the exact ground-state electronic energy $E(n(\mathbf{r}))$ of an N-electron system can be written as:

$$E(n(\mathbf{r})) = \frac{-\hbar^2}{2m}\sum_{i=1}^{N}\int \psi_i^*(\mathbf{r})\nabla^2\psi_i(\mathbf{r})d\mathbf{r} - \sum_{I=1}^{N_{nucl}}\frac{Z_I}{r_I}n(\mathbf{r})d\mathbf{r} + \frac{1}{2}\int\frac{n(\mathbf{r})n(\mathbf{r}')}{|\mathbf{r}-\mathbf{r}'|}d\mathbf{r}d\mathbf{r}' + E_{XC}(n(\mathbf{r})) \qquad (4.12)$$

The first term on the right in Eq. (4.12) represents the kinetic energy of the electrons; the second term represents the electron-nucleus attraction where the sum is over all N_{nucl} nuclei with index I and atomic number Z_I; the third term represents the Coulomb interaction between the total charge distribution at $\mathbf{r}$ and $\mathbf{r}'$; the last term is the exchange-correlation energy of the system, which is also a functional of the density and takes into account all non-classical electron-electron interactions. Of the four terms, E_{XC} is the one we do not know how to obtain exactly. Although the Hohenberg-Kohn theorem tells that E and therefore E_{XC} mut be functionals of the electron density, we do not know the latter's exact analytical form and so are forced to use approximate expressions for it.

The exact ground-state electron density is given by:

$$n(\mathbf{r}) = \sum_{i=1}^{n} |\psi_i(\mathbf{r})|^2 \tag{4.13}$$

where the sum is over all the occupied one-electron orbitals called Kohn-Sham (KS) orbitals; once these orbitals have been computed, $n(\mathbf{r})$ is known.

The KS orbitals are found by solving the Kohn-Sham equations, which are derived by applying the variational principle to the electronic energy $E(n(\mathbf{r}))$ with the charge density given by Eq. (4.13). The Kohn-Sham equations for the one electron orbitals $\psi_i(\mathbf{r_i})$ have the form:

$$\left[\frac{-\hbar^2}{2m}\nabla^2 - \sum_{I=1}^{N_{nucl}} \frac{Z_I}{r_I} + \int \frac{n(\mathbf{r}')}{|\mathbf{r}-\mathbf{r}'|} d\mathbf{r}' + V_{XC}(\mathbf{r})\right] \psi_i(\mathbf{r}) = \varepsilon_i \psi_i(\mathbf{r}) \tag{4.14}$$

where ε_i are the Kohn-Sham orbital energies and the exchange-correlation potential, V_{XC}, is the functional derivative of the exchange-correlation energy:

$$V_{XC}[n(\mathbf{r})] = \frac{\delta E_{XC}[n(\mathbf{r})]}{\delta n(\mathbf{r})} \tag{4.15}$$

If E_{XC} is known, then V_{XC} can be obtained. The Kohn-Sham equations are solved in a self-consistent manner. Initially, we guess the electron density $n(\mathbf{r})$, typically by using a superposition of atomic densities. By using some approximate form (which remains fixed during all iterations) for the functional E_{XC}, we next compute V_{XC} as a function of $\mathbf{r}$. The set of Kohn-Sham equations is then solved to obtain an initial set of KS orbitals. This set of orbitals is then used to compute an improved density from Eq. (4.13), and the process is repeated until the density and exchange-correlation energy have converged to within some tolerance. The electronic energy is then computed by Eq. (4.12).

Currently DFT is a very accurate method and its accuracy can be en-

hanced by the use of methods combining Hartree-Fock and DFT descriptions, for example, B3LYP [1] functional description [163]. The computation time required for a DFT calculation formally scales as the third power of the number of basis functions, as a result, DFT methods are computationally more efficient than Hartree-Fock based formalisms, which scale as the fourth power of the number of basis functions. However, for large systems, even this third power scaling makes computational investigations impractical and hence researchers depend on semi-empirical methods for such systems.

4.1.2 Semiempirical methods

The power of semiempirical methods with respect to the first principle methods lies in a smaller consumption of CPU-time but they must be employed more carefully to obtain reliable results. In general, these methods use various approximations and may include experimentally fitted parameters. One of the limitations to the accuracy of the semiempirical methods in addition to the approximations inherent in their formulation is the accuracy of the experimental data used to obtain these parameters. However, because adjustable parameters are optimised to reproduce a number of important chemical properties, semiempirical methods have become widely popular. Semiempirical methods include interaction schemes like the tight binding method (TB) [164] and various molecular orbital methods of computational chemistry [163].

The tight binding method avoids most of the heavy calculation of the *ab initio* methods. They have in common a number of simplifications such as minimal basis set compared to the first-principles methods and elimination of difficult integrals, that are either made small by mathematical transformations or used as parameters to be fit to experimental data. In the tight binding model for a solid-state lattice of atoms, it is assumed that the full

[1] B3LYP is short form form **B**ecke's **3**-parameter formula, B3, which describes the exchange functional, and LYP for **L**ee, **Y**ang, **P**arr who developed the correlation functional [163].

Hamiltonian H of the system may be approximated by the Hamiltonian of an isolated atom centred at each lattice point [160]. The atomic orbitals ψ_n, which are eigenfunctions of the single atom Hamiltonian H_{at}, are assumed to be very small at distances exceeding the lattice constant, so that the lattice sites can be treated independently. The actual crystal Hamiltonian H is given by adding a correction potential to H_{at}:

$$H = H_{at} + \Delta U(\mathbf{r}) \tag{4.16}$$

It is further assumed that any corrections to the atomic potential ΔU, which are required to obtain the full Hamiltonian H of the system, are appreciable only when the atomic orbitals are small. A solution to the time-independent single electron Schrödinger equation Φ is then assumed to be a linear combination of atomic orbitals ψ_n:

$$\Phi(\mathbf{r}) = \sum_n b_n \psi_n(\mathbf{r}) \tag{4.17}$$

where n refers to the n-th atomic energy level. Using this approximate form for the wavefunction, and assuming only the m-th atomic energy level is important for the m-th energy band, the Bloch energies ε_m are of the form:

$$\varepsilon_m(\mathbf{k}) = E_m - \frac{\beta_m + \sum_{\mathbf{R}\neq 0} \gamma_m(\mathbf{R}) e^{i\mathbf{k}\cdot\mathbf{R}}}{b_m + \sum_{\mathbf{R}\neq 0} \alpha_m(\mathbf{R}) e^{i\mathbf{k}\cdot\mathbf{R}}} \tag{4.18}$$

where β_m, $\gamma_m(\mathbf{R})$ and $\alpha_m(\mathbf{R})$ are the overlap integrals which are defined by:

$$\beta_m = -\int \psi_m^*(\mathbf{r}) \Delta U(\mathbf{r}) \Phi(\mathbf{r}) d^3\mathbf{r}, \tag{4.19}$$

$$\gamma_m(\mathbf{R}) = \int \psi_m^*(\mathbf{r}) \Phi(\mathbf{r} - \mathbf{R}) d^3\mathbf{r}, \tag{4.20}$$

$$\alpha_m(\mathbf{R}) = -\int \psi_m^*(\mathbf{r}) \Delta U(\mathbf{r}) \Phi(\mathbf{r} - \mathbf{R}) d^3\mathbf{r}. \tag{4.21}$$

In principle, everything that can be calculated by the *ab initio* methods can be calculated by an appropriate tight binding method and with less CPU-time. The keyword above is the 'appropriate': the generality and the transferability of a tight binding method depends on the approximations. Although valid for thousands of particles, the method used must be assessed case-specifically.

In computational physics and chemistry the methods similar to tight binding are called the neglect of diatomic differential overlap methods [163]. Also these methods simplify the involved integrals but retain the molecular orbital description. The group involves various methods such as AM1 [2] and PM3 [3] [163].

4.1.3 Empirical methods

The category of empirical methods contains a wide set of parametrised classical force fields that reproduce more or less accurately the fitting set that is determined either from experimental data or from *ab initio* simulations. Force-field methods have the benefit of being computationally simple and thus fast. They allow the simulation of large systems (up to hundreds of millions of atoms) over a greater time-span (up to microseconds) than the methods presented above.

The simplest approximation for the interaction potential takes into account only two-particle interactions. Potentials like this are called pair potentials. The Lennard-Jones potential [165] and the Morse potential [166] are two very well known examples of pair potentials. Although pair potentials are not ideal for the study of the energetics and mechanical properties

[2] **A**ustin **M**odel **1** is named after the place of its origin, that is, University of Texas, Austin, USA.

[3] **P**arametrized **M**odel **3** is named so because it was the third parametrised model released by the person in charge of its development.

of materials, they are very much used because they are simple to implement and algorithms based on pair potentials are kind on computational resources. There are, however, some severe shortcomings which should be taken into account whenever pair potentials are used. For example, an interaction described by a pair potential model can depend only on the distance between two particles. Thus the potential cannot model directional bonding. Pair potentials often predict wrong vacancy formation energies and melting temperatures [165, 166].

The construction of an accurate force-field encounters often system and material based difficulties, and often even fundamental limitations. Difficult media are metals, alloys, semiconductors, and oxide-based insulators. In this thesis the emphasis is, of course on carbon. Describing carbon accurately requires a lot of caution and is difficult because the $2s$ electrons participate in molecular bonding and together with $2p$ electron orbitals hybridise to form a wide variety of potential bonding configurations that depend on the environment and on the ambient conditions. Even by itself, carbon can form structures as diverse as the isotropic diamond crystal or the anisotropic planar graphite and nanostructures. If the consideration is extended to organic molecules, even only hydrocarbons, the bonding variety, and at the same time the complexity of describing it accurately, becomes vast.

If covalently bonding materials, like sp^2-carbon, are simulated, the modelling of directional bonding is essential in order not to obtain outright wrong results. In general this means that the interaction potential used must include at least a three-body interaction term. Because carbon is the basis of all organic materials and because diamond and graphite have various applications in materials science, numerous attempts to create accurate classical interaction potential have been made but only a few of the proposed schemes are widespread. For example, carbon interaction potential developed by Tersoff in Refs. [158, 167, 168] and Brenner in Ref. [159] are widely used in

the modelling of carbon. The Brenner model is considered more versatile because of additional conjugated bond description while the structures modelled by the Tersoff model suffer from an over binding of radicals and the description of systems involving bonds that exhibit a mixture of sp^3 and sp^2 hybridizations is inaccurate. Both models are short ranged cover only the nearest neighbours to speed up the calculations. For description of graphite or multi-walled nanotubes, much longer range interactions are required. Various long-range extensions that are most often based on Lennard-Jones type additional term to describe the π-bonding have been proposed. Stuart *et al.* [169] have aimed at maintaining the reactivity description of the Brenner [159] model while introducing the long-range interactions.

In general the force-field methods can give information on the structure and dynamics of a system, the total energies, entropies, free energies, and diffusive process in the system. By their construction the methods are incapable of predicting any properties related to the electronics structure such as electrical conductivity, optical, or magnetic properties. In short, the classical force field methods are structure control tools. The general accuracy of results obtained by classical force field methods is far from the level of accuracy obtained by *ab initio* simulations but so are the feasible system size and the attainable time scale as well.

4.1.4 Molecular dynamics studies

As described in detail in the previous sections, first principle calculations which include quantum mechanical details are the best method for the study of any system. But from theoretical calculation point of view, it is usually not practical to carry out first principle calculations for larger systems (> 100 atoms). In such cases, molecular dynamics simulation is one of the widely used theoretical methods to calculate various mechanical, thermodynamical and even chemical properties of large systems.

Molecular dynamics (MD) method is a computer simulation technique where the time evolution of a set of interacting atoms is followed by integrating their equations of motion [170,171]. In molecular dynamics, we follow the laws of classical mechanics, and most notably Newton's law for each atom i in a system constituted by N particles:

$$\mathbf{F}_i = m_i \mathbf{a}_i \tag{4.22}$$

Here, m_i is the mass of the particle, $\mathbf{a}_i = d^2\mathbf{r}_i/dt^2$, its acceleration, and $\mathbf{F}_i$ is the force acting upon it, due to the interactions with other atoms. Given an initial set of positions and velocities, the subsequent time evolution is in principle completely determined and hence it is a deterministic technique. The main ingredient of a molecular dynamics simulation is a model for the physical system under consideration. This requires the definition of a potential function $V(\mathbf{r}_1, \ldots, \mathbf{r}_N)$, or a description of the terms by which the particles in the simulation will interact. This function is translationally and rotationally invariant, and is usually constructed from the relative positions of the atoms with respect to each other, rather than from the absolute positions. In chemistry and biology this is usually referred to as a force field. Forces are then derived as the gradients of the potential with respect to atomic displacements:

$$\mathbf{F}_i = -\nabla_{\mathbf{r}_i} V(\mathbf{r}_1, \ldots, \mathbf{r}_N) \tag{4.23}$$

This form implies the presence of a conservation law of the total energy $E = K + V$, where K is the instantaneous kinetic energy. The simplest choice for V is to write it as a sum of pairwise interactions:

$$V(\mathbf{r}_1, \ldots, \mathbf{r}_N) = \sum_i \sum_{j>i} \phi(|\mathbf{r}_i - \mathbf{r}_j|) \tag{4.24}$$

The clause $j > i$ in the second summation has the purpose of considering each atom pair only once. In the past most potentials were constituted by

pairwise interactions, but this is no longer the case. It has been recognised that the two-body approximation is very poor for many relevant systems.

The engine of a molecular dynamics program is its time integration algorithm, required to integrate the equation of motion of the interacting particles and follow their trajectory. Time integration algorithms are based on finite difference methods, where time is discretized on a finite grid, the time step Δt being the distance between consecutive points on the grid. Knowing the positions and some of their time derivatives at time t (the exact details depend on the type of algorithm), the integration scheme gives the same quantities at a later time $t + \Delta t$. By iterating the procedure, the time evolution of the system can be followed for long times. Two popular integration methods for MD calculations are the Verlet algorithm and predictor-corrector algorithms [170, 171]. They are quickly presented in the sections below.

In molecular dynamics, the most commonly used time integration algorithm is probably the so-called Verlet algorithm [172, 173]. The basic idea is to write two third-order Taylor expansions for the positions $\mathbf{r}(t)$, one forward and one backward in time. Calling $\mathbf{v}$ the velocities, $\mathbf{a}$ the accelerations, and $\mathbf{b}$ the third derivatives of $\mathbf{r}$ with respect to t, one has:

$$\mathbf{r}(t + \Delta t) = \mathbf{r}(t) + \mathbf{v}(t)\Delta t + ...(t)\Delta t^2 + (1/6)\mathbf{b}(t)\Delta t^3 + O(\Delta t^4) \quad (4.25)$$

$$\mathbf{r}(t - \Delta t) = \mathbf{r}(t) - \mathbf{v}(t)\Delta t + ...(t)\Delta t^2 - (1/6)\mathbf{b}(t)\Delta t^3 + O(\Delta t^4) \quad (4.26)$$

Adding the two expressions gives:

$$\mathbf{r}(t + \Delta t) = 2\mathbf{r}(t) - \mathbf{r}(t - \Delta t) + \mathbf{a}(t)\Delta t^2 + O(\Delta t^4) \quad (4.27)$$

This is the basic form of the Verlet algorithm. Since we are integrating Newton's equations, $\mathbf{a}(t)$ is just the force divided by the mass, and the force

is in turn a function of the positions $\mathbf{r}(t)$:

$$\mathbf{a}(t) = -(1/m)\nabla V\left(\mathbf{r}(t)\right) \tag{4.28}$$

A problem with this version of the Verlet algorithm is that velocities are not directly generated. While they are not needed for the time evolution, their knowledge is sometimes necessary. Moreover, they are required to compute the kinetic energy K, whose evaluation is necessary to test the conservation of the total energy $E = K + V$. This is one of the most important tests to verify that a MD simulation is proceeding correctly. One could compute the velocities from the positions by using

$$\mathbf{v}(t) = \frac{\mathbf{r}(t + \Delta t) - \mathbf{r}(t - \Delta t)}{2\Delta t}. \tag{4.29}$$

Predictor-corrector algorithms constitute another commonly used class of methods to integrate the equations of motion and it consists of three steps [174]. The predictor does the following; From the positions and their time derivatives up to a certain order q, all known at time t, one predicts the same quantities at time $t + \Delta t$ by means of a Taylor expansion. Among these quantities are, of course, accelerations $\mathbf{a}$. The second step is the force evaluation. The force is computed taking the gradient of the potential at the predicted positions. The resulting acceleration will be in general different from the predicted acceleration. The difference between the two constitutes an error signal. Third step involves the corrector. Here, the error signal obtained from previous step is used to correct positions and their derivatives. All the corrections are proportional to the error signal, the coefficient of proportionality being a magic number determined to maximize the stability of the algorithm.

The outcomes of molecular dynamics simulations are mainly determined by the interaction potentials (force fields) that are used in the calculations. It

is crucial to know the validation regime of a certain potential function. While several standard potential functions have emerged for particular classes of systems, at present there is no definitive functional form that adequately describes all types of multi-atom bonding. Instead, potentials are often developed for specific applications with functions and parameters determined on an *ad hoc* basis. This process leads to considerable and justified uncertainty with regard to the reliability of quantitative results produced by analytic potentials.

4.2 Force fields employed in this thesis

In this thesis, the emphasis is on developing a simple and computationally inexpensive model for studying the energetics of carbon nanotubes. Classical methods are used for obtaining the parameters of the model and this choice allows studying structures that have dimensions comparable to experimentally observed ones. These include Brenner and Tersoff potentials. Following section contains a detailed explanation of these potentials along with a brief introduction to the developing of analytic potentials for studying specific phenomena.

4.2.1 Introduction

Analytical potential energy functions (sometimes referred to as empirical or classical potentials) are simplified mathematical expressions that attempt to model interatomic forces arising from the quantum mechanical interaction of electrons and nuclei. Their use is generally necessitated either by the desire to model systems with sizes and/or timescales that exceed available computing resources required for quantum calculations, or to gain qualitative insight into things like bonding preferences that may not be immediately obvious from the results of numerical calculations.

The development of an analytic interatomic potential energy expression includes two aspects. The first is the derivation of relatively simple but sound functional form that captures the essence of quantum mechanical bonding. The second aspect is making the potential function practical for specific applications by incorporating additional empirically-derived functions and parameters. A potential energy function with flexibility, accuracy, transferability and computational efficiency is considered to be an effective one.

To study the structure and energetics of carbon nanotubes, in this thesis we used the bond-order Tersoff potential and Brenner empirical potential, which were developed for covalent systems and parametrised for carbon. Both these potentials are developed from the formalism introduced by Abell [175]. This formalism models the local attractive electronic contribution to the binding energy E_i of an atom i using an interatomic bond-order that modulates a two-centre interaction,

$$E_i = -\sum_{j \neq i} B_{ij} V^A(r_{ij}), \tag{4.30}$$

where the sum is over nearest neighbours j of atom i, B_{ij} is the bond-order function between atoms i and j, $V^A(r_{ij})$ is the pair term and r_{ij} is the scalar distance between the atoms i and j. The function $V^A(r_{ij})$, which represents bonding from valence electrons, is assumed to be transferable between different atomic hybridizations. All many-body effects such as changes in the local density of states with varying local bonding topologies are included in the bond-order function. Abell suggested that the major contribution to the bond-order function (B_{ij}) is local coordination z, and using a Bethe lattice he derived the approximation $B_{ij} = z^{-1/2}$. By balancing the attractive local bonding contributions with a pair sum of repulsive interactions, Abell was able to show that the wide range of stable bonding configurations can be rationalised by different ratios of slopes of the repulsive to attractive pair terms, while maintaining the approximate bonding universality suggested by

Rose and coworkers [176]. Assuming exponentials for the repulsive and attractive pair interactions, the analytic interatomic potential energy form for the cohesive energy E_{coh} of a collection of atoms becomes:

$$E_{coh} = \sum_i E_i; \qquad E_i = \sum_{j \neq i} [Ae^{-\alpha r_{ij}} - B_{ij} Be^{-\beta r_{ij}}], \tag{4.31}$$

where E_i is the binding energy of individual atoms.

4.2.2 Tersoff potential

A practical implementation of Abell's bond-order formalism was developed by Tersoff for modelling group IV materials. He introduced an empirical functional form for the bond-order that incorporates angular interactions while still maintaining coordination as the dominant feature determining structure. A subtle but crucial feature of Tersoff's bond-order function is that it did not assume different forms for the angular terms for different hybridizations. Instead, it uses an angular function that is determined by a global fit to structures with various coordinations. This feature, together with a physically-motivated functional form provides the function with an extraordinary degree of transferability.

To study the structure and energetics of carbon nanotubes, we used the Tersoff empirical potential [158], which was developed for covalent systems and parametrised for carbon [177]. The Tersoff potential is a many body potential, which depends on the nearest neighbours of atoms and has the following form:

$$V_{ij} = f_C(r_{ij})[a_{ij} f_R(r_{ij}) + b_{ij} f_A(r_{ij})]. \tag{4.32}$$

Here, $f_C(r_{ij})$ is the cut-off function which limits the interaction of an atom

to its nearest neighbours:

$$f_C(r_{ij}) = \begin{cases} 1, \ r_{ij} \leq R - D \\ \frac{1}{2} - \frac{1}{2}\sin[\frac{\pi}{2}(r_{ij} - R)/D], \ R - D < r_{ij} \leq R + D \\ 0, \ r_{ij} > R + D, \end{cases} \tag{4.33}$$

where r_{ij} is the distance between the i^{th} and the j^{th} atoms, R and D are parameters taken from Ref. [177], which determine the range of the potential. $f_R(r_{ij})$ and $f_A(r_{ij})$ in Eq. (4.32) are the repulsive and the attractive terms of the potential respectively, which are defined as follows:

$$f_R(r_{ij}) = A\exp(-\lambda_1 r_{ij}) \tag{4.34}$$

$$f_A(r_{ij}) = -B\exp(-\lambda_2 r_{ij}). \tag{4.35}$$

Here, A, B, λ_1 and λ_2 are the positive parameters of the potential, which were derived for carbon in Ref. [177]. The factor b_{ij} in Eq. (4.32) is the so-called bond order term, which is defined as follows:

$$b_{ij} = (1 + \beta^n \zeta_{ij}^n)^{-1/2n}, \tag{4.36}$$

where β and n are parameters of the potential, while ζ_{ij} is defined as:

$$\zeta_{ij} = \sum_{k \neq i,j} f_C(r_{ik}) g(\theta_{ijk}) \exp\left[\lambda_3^3 (r_{ij} - r_{ik})^3\right]. \tag{4.37}$$

Here, $f_C(r_{ik})$ is the cut-off function introduced in Eq. (4.33), λ_3 is another parameter of the potential. The function $g(\theta_{ijk})$ is defined as:

$$g(\theta_{ijk}) = 1 + \frac{c^2}{d^2} - \frac{c^2}{d^2 + (h - \cos\theta_{ijk})^2}, \tag{4.38}$$

where θ_{ijk} is the angle between bonds formed by pairs of atoms (i, j) and

(i, k). The function a_{ij} in Eq. (4.32) reads as:

$$a_{ij} = (1 + \alpha^n \eta_{ij}^n)^{-1/2n} \tag{4.39}$$

with α and n being parameters, while η_{ij} is defined as:

$$\eta_{ij} = \sum_{k \neq i,j} f_C(r_{ik})\, exp\left[\lambda_3^3 (r_{ij} - r_{ik})^3\right]. \tag{4.40}$$

A (eV)	B (eV)	λ_1 (Å^{-1})	λ_2 (Å^{-1})	λ_3 (Å^{-1})	α	$\beta \times 10^{-7}$
1393.6	346.74	3.488	2.212	0.0	0.0	1.572
n	c	d	h	R (Å)	D (Å)	
0.7275	38049	4.3484	-0.5706	1.95	0.15	

Table 4.1: Parameters of the Tersoff potential used in the calculations [177].

The Tersoff potential was used earlier for the studies on the stability and structural properties of many carbon systems including fullerenes [178–180] and nanotubes [181–183] and it is proved to be reliable. The parameters of the Tersoff potential are slightly different in different articles. In Tab. 4.1, we compile the parameters used in the present thesis.

4.2.3 Limitations of Tersoff potential

The procedure used by Tersoff to develop classical potentials for silicon, carbon and germanium is to fit the pair terms and an analytic expression for B_{ij} to a number of properties of the diatomic and solid-state structures (e.g., bond energies and lengths, bulk moduli , vacancy formation energies, etc.). His expression developed in this way appears to be relatively transferable to other solid-state structures not used in the fitting procedure such as surface reconstructions on silicon and interstitial defects in carbon. However,

further analysis shows that this expression is unable to reproduce a number of properties of carbon such as a proper description of radicals and conjugated versus non-conjugated double bonds. Donald Brenner [159] extended Tersoff potential by adding additional terms in the bond order term which enabled him to explain many properties that were not explainable by Tersoff potential. Following section contatins a detailed description of Brenner potential.

4.2.4 Brenner potential

Brenner potential is an empirical many-body potential, which was originally developed for hydrocarbons, that can model intramolecular chemical bonding in a variety of small hydrocarbon molecules as well as graphite and diamond lattices. This potential function is based on Tersoff's covalent-bonding formalism with additional terms that correct for an inherent overbinding of radicals and that include nonlocal effects and was developed in 1990 by Donald W. Brenner [159]. The potential function is short ranged and quickly evaluated so it should be very useful for large-scale molecular dynamics simulations of reacting hydrocarbon molecules.

The binding energy in Brenner formalism is written exactly like that in the Abell-Tersoff formalism as a sum over atomic sites i,

$$E_b = \frac{1}{2}\sum_i E_i \tag{4.41}$$

where each contribution E_i is written as

$$E_i = \sum_{j \neq i} [V_R(r_{ij}) - B_{ij} V_A(r_{ij})] \tag{4.42}$$

In Eq. 4.42, the sum is over nearest neighbours j of atom i, $V_R(r_{ij})$ and $V_A(r_{ij})$ are pair-additive repulsive and attractive interactions, respectively,

and B_{ij} represents a many-body coupling between the bond from atom i to atom j and the local environment of atom i. As discussed by Abell and Tersoff, if Morse-type functions are used for the repulsive and attractive pair terms, then B_{ij} can be considered a normalised bond order because the Pauling relationship between bond order and bond length is realized. Putting Eq. 4.42 into Eq. (4.41), one obtains an expression for the binding energy as:

$$E_b = \frac{1}{2}\sum_i \sum_{j \neq i} [V_R(r_{ij}) - \overline{B}_{ij} V_A(r_{ij})], \tag{4.43}$$

where the empirical bond-order function is given by:

$$\overline{B}_{ij} = \frac{1}{2}[B_{ij}^{\sigma-\pi} + B_{ji}^{\sigma-\pi}] + B_{ij}^{\pi} \tag{4.44}$$

The local coordination and bond angles for atoms i and j determine the values for the functions $B_{ij}^{\sigma-\pi}$ and $B_{ji}^{\sigma-\pi}$. Brenner has written the function B_{ij}^{π} as a sum of two terms:

$$B_{ij}^{\pi} = \Pi_{ij}^{RC} + B_{ij}^{DH} \tag{4.45}$$

The value of the first term Π_{ij}^{RC} depends on whether a bond between atoms i and j has radical character and is part of a conjugated system. The value of the second term B_{ij}^{DH} depends on the dihedral angle for carbon-carbon double bonds. This expression combined with Eq. (4.43) is used to define the binding energy due to covalent bonding of any collection of hydrogen and carbon atoms. As in the case of traditional valence-force fields, Brenner potential assumes no predetermined atomic hybridizations; instead, atomic bonding is determined strictly from local bonding neighbours and non-local conjugation. Because the local bonding environment determines the effective interatomic interactions, and not the other way around, the influence of atomic rehybridization on the binding energy can be modelled as covalent bonds break and reform within a classical potential.

Tersoff potential used Morse-type terms for the pair interactions. However, it was not capable of simultaneously fitting equilibrium distances, energies, and force constants for carbon-carbon bonds. Moreover, Morse-type terms have the further disadvantage that both terms go to infinite values as the distance between atoms decreases, limiting the possibility of modelling processes involving energetic atomic collisions. By taking all these drawbacks into consideration, Brenner developed new forms for the repulsive and attractive terms in the potential as:

$$V^R(r) = f^c(r)(1 + Q/r)Ae^{-\alpha r} \tag{4.46}$$

and

$$V^A(r) = f^c(r)\sum_{n=1}^{3} B_n e^{-\beta_n r} \tag{4.47}$$

Here r is the scalar distance between atoms. The screened Coulomb function used for the repulsive pair interaction (Eq. (4.46)) goes to infinity as interatomic distances approach zero, and the attractive term (Eq. (4.47)) has sufficient flexibility to simultaneously fit the bond properties that could not be fitted with the Morse-type terms used in Tersoff potential. Like in the case of Tersoff potential, the function $f^c(r)$ limits the range of the covalent interactions. The value of this function is defined by a switching function of the form:

$$f_{ij}^c(r) = \begin{cases} 1, \ r \leq D_{ij}^{min} \\ \frac{1}{2} + \frac{1}{2}\cos[\pi(r - D_{ij}^{min})/(D_{ij}^{max} - D_{ij}^{min})], \ D_{ij}^{min} < r \leq D_{ij}^{max} \\ 0, \ r > D_{ij}^{max}, \end{cases} \tag{4.48}$$

where $D_{ij}^{max} - D_{ij}^{min}$ defines the distance over which the function goes from one to zero. The bond-order term has got the form:

$$B_{ij}^{\sigma-\pi} = [1 + \sum_{k(\neq i,j)} f_{ik}^c(r_{ik})G(\cos(\theta_{ijk}))e^{\lambda_{ijk}} + P_{ij}(N_i^C, N_i^H)]^{-1/2} \tag{4.49}$$

As in the previous equations, the subscript refer to the atom identity, and the function $f^c(r)$ ensures that the interactions include nearest neighbours only. The function P represents a bicubic spline and the quantities N_i^C and N_i^H represent the number of carbon and hydrogen atoms, respectively, that are neighbours of atom i. These are defined by the sums:

$$N_i^C = \sum_{k(\neq i,j)}^{carbon\ atoms} f_{ik}^c(r_{ik}) \tag{4.50}$$

and

$$N_i^H = \sum_{(\neq i,j)}^{hydrogen\ atoms} f_{il}^c(r_{il}) \tag{4.51}$$

For solid state carbon, values of λ and the function P are taken to be zero. The function P can be envisioned as correction to the solid-state analytic bond order function that are needed to accurately model molecular bond energies. An identical expression is given for $B_{ji}^{\sigma-\pi}$ by swapping i- and j-indices in Eq. (4.49).

The form of the function $G(\cos(\theta_{ijk}))$ is obtained using sixth-order polynomial splines for the available data points. These data points are obtained from the bond energy informations of diamond lattice and graphitic sheets. The function is plotted in Fig. 4.1. By analysing the energy of small ring hydrocarbons, Brenner found that the values of $G(\cos(\theta_{ijk}))$ are too large for undercoordinated carbon atoms. To allow for both overcoordinated and undercoordinated atoms, a second spline $\gamma_C(\cos(\theta))$ was determined that was coupled to $G(\cos(\theta_{ijk}))$ through the local coordination. The revised angular function is given by:

$$g_C = G_C(\cos(\theta)) + Q(N_i^t)[\gamma_C(\cos(\theta)) - G_C(\cos(\theta))] \tag{4.52}$$

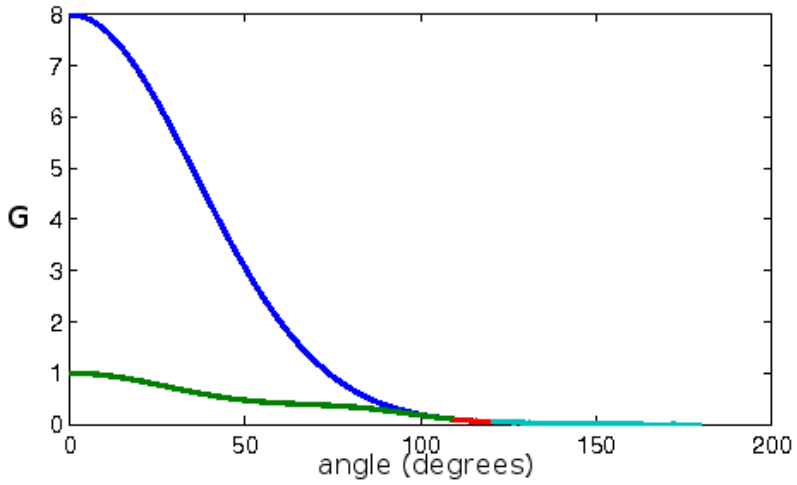

Figure 4.1: The angular contribution, $G(\cos(\theta_{ijk}))$, to the bond order term. The blue line shows the actual spline fit to the data and the green line is the modified form of the angular function for low-coordination structures.

where the function Q is defined by:

$$Q_i(N_i^t) = \begin{cases} 1, \ N_i^t \leq 3.2 \\ \frac{1}{2} + \frac{1}{2}\cos[2\pi(N_i^t - 3.2)], \ 3.2 < N_i^t \leq 3.7 \\ 0, \ N_i^t > 3.7, \end{cases} \tag{4.53}$$

The quantity N_i^t is the coordination of atom i which is given by,

$$N_i^t = N_i^C + N_i^H \tag{4.54}$$

where N_i^C and N_i^H are defined by equations Eq. (4.50) and (4.51), respectively.

The term Π_{ij}^{RC} in Eq. (4.45) represents the influence of radical energetics and π-bond conjugation on the bond energies. This term is necessary to correctly describe radical structures such as the vacancy formation energy in diamond, and to account for non-local conjugation effects such as those govern the different properties of the carbon-carbon in graphite and benzene.

This function is taken as a tricubic spline F that depends on the total number of neighbours of bonded atoms i and j as well as a function N_{ij}^{conj} which depends on local conjugation.

$$\Pi_{ij}^{RC} = F_{ij}(N_i^t, N_j^t, N_{ij}^{conj}) \tag{4.55}$$

To calculate whether a bond is part of a conjugated system, the value of N_{ij}^{conj} in Eq. (4.55) is given by the function:

$$N_{ij}^{conj} = 1 + [\sum_{k(\neq i,j)}^{carbon} f_{ik}^c(r_{ik})F(X_{ik})]^2 + [\sum_{l(\neq i,j)}^{carbon} f_{jl}^c(r_{jl})F(X_{jl})]^2 \tag{4.56}$$

where

$$F(X_{ik}) = \begin{cases} 1, \ x_{ik} \leq 2 \\ \frac{1}{2} + \frac{1}{2}\cos[\pi(x_{ik} - 2)], \ 2 < x_{ik} \leq 3 \\ 0, \ x_{ik} > 3, \end{cases} \tag{4.57}$$

and

$$x_{ik} = N_k^t - f_{ik}^c(r_{ik}) \tag{4.58}$$

If all of the carbon atoms that are bonded to a pair of carbon atoms i and j have four or more neighbours, equations (4.56)-(4.58) yield a value of one for N_{ij}^{conj}, and the bond between these atoms is not considered to be part of a conjugate system. As the coordination numbers of the neighbouring atoms decrease, N_{ij}^{conj} becomes greater than one, indicating a conjugated bonding configuration. Furthermore, the form of equations (4.56)-(4.58) distinguishes between different configurations that can lead to conjugation. For example, the value of N_{ij}^{conj} for a carbon carbon bond in graphite is nine, while that for a bond in benzene is three. This difference yields considerable extra flexibility for fitting the energies of conjugated systems. These equations provide a straightforward way of incorporating conjugation effects into a classical potential energy function without having to diagonalize a matrix or go be-

yond nearest neighbour interactions. Furthermore, changes in conjugation as bonds break and from are smoothly accounted for. This approach considerably reduces computational time while still including conjugation to a first approximation.

Discrete values for the function defined by equation (4.55) are chosen to fit the energies of static structures and tricubic splines are used to interpolate between these values.

B_1 (eV)	B_2 (eV)	B_3 (eV)	β_1 (Å^{-1})	β_2 (Å^{-1})	β_3 (Å^{-1})
12388.792	17.567	30.715	4.720	1.433	1.383
λ (Å^{-1})	A (eV)	Q (Å)	α (Å^{-1})	D_{min}	D_{max}
0.0	10953.544	0.313	4.747	1.7	2.0

Table 4.2: Parameters of the Brenner potential used in the calculations [159].

The term B_{ij}^{DH} in Eq. (4.45) is given by:

$$B_{ij}^{DH} = T_{ij}(N_i^t, N_j^t, N_{ij}^{conj})[\sum_{k(\neq i,j)}\sum_{l(\neq i,j)}(1-\cos^2(\Theta_{ijkl}))f_{ik}^c(r_{ik})f_{jl}^c(r_{jl})] \quad (4.59)$$

where

$$\Theta_{ijkl} = \mathbf{e}_{jik}\mathbf{e}_{ijl}. \quad (4.60)$$

The function $T_{ij}(N_i^t, N_j^t, N_{ij}^{conj})$ is a tricubic spline, and the functions e_{jik} and e_{ijl} are unit vectors in the direction of the cross products $\mathbf{R}_{ji} \times \mathbf{R}_{ik}$ and $\mathbf{R}_{ij} \times \mathbf{R}_{jl}$, respectively, where the $\mathbf{R}$ are vectors connecting the subscripted atoms. These equations incorporate a standard method for describing forces for rotation about dihedral angles for carbon-carbon double bonds into the analytic bond order. The value of this function is zero for a planar system, and one for angles of 90°. Therefore the function T_{CC} determines the barrier for rotation about these bonds,. This function was parametrised such that for carbon-carbon bonds that are not double bonds, this contribution to the bond order is zero. The value for T_{CC} for non-conjugated carbon-carbon

bonds was fitted to the barrier for rotation about ethene. The value for T_{CC} for conjugated double bonds was fitted such that for all dihedral angles of 90° , the minimum-energy bond length is 1.45Å. This value was chosen because it is the average bond length for hypothetical structure analysed theoretically by Liu *et al.* Like graphite this structure contains all threefold-coordinated atoms, but with each dihedral angle equal to 90° rather than 9°.

The entire parameter-fitting scheme described above was made considerably easier by assuming only nearest-neighbour interactions. The way to best define this for a continuous function, however, is problematic. The approach used here to handle this is same as that used by Tersoff, i.e., using a limiting function $f^c(r)$ defined by Eq. (4.48). The parameters of Brenner potential are compiled in Tab.4.2.

4.3 Necessity and importance of physical models

As discussed in the previous sections, researchers had already been used various theoretical methods for the study of the energetics of carbon nanotubes including DFT calculations and molecular dynamics simulations. Each of these methods have their own advantages and disadvantages and the relevance of a particular method depends on which aspect of the nanotube is under interrogation. First principle DFT calculations have the serious limitation of being computationally expensive and hence they could not be applied for the study of nanotubes with reasonably large number of atoms. In such situations, methods based on molecular dynamics plays the role of a potential substitute but even they have limitations on the size of the system to be investigated. For example, studying a nanotube with millions of atoms using molecular dynamics simulation is also computationally demanding.

Hence, one reaches a stage that demands the introduction of a simple and computationally less expensive approach to study the theoretical aspects of

carbon nanotubes. In this regard, physical models which take into account all the important necessary details of the system could serve as an effective tool for studying the energetics of nanosystems. Every model is based on a set of parameters which makes them simple and computationally much less expensive. The parameters of a model could be obtained from first principle calculations or calculations with classical methods for small nanotubes and once they are obtained they can directly used for nanotubes of any size.

In this thesis we propose such a model for calculating the binding energy of single-walled carbon nanotubes of arbitrary chirality and we call this model as liquid surface model. Liquid surface model can provide the energy of any nanotube once its chirality and total number of atoms are known. The number of parameters of the model varies depending on whether the nanotube is open or capped. Liquid surface model assumes that the total energy of a single-walled nanotube can be written as a sum of surface, curvature, and edge energy terms. The motivation behind this model came from similar models which were used for the studies of a variety of systems like charged droplets, nuclei and clusters for more than a century ago [184–192]. Following section contains a brief introduction to such models used for the studies of various systems.

4.3.1 Motivation behind liquid surface model

In 1882 Lord Rayleigh proposed a model called liquid drop model in his studies on the stability and fission of charged droplets where a classical charged drop deforms through elongated shapes to form separate droplets. [184]. He predicted for an incompressible charged liquid droplet that the quadrupole oscillation becomes unstable as soon as the disruptive Coulomb force is equal to the attractive cohesive force or, in terms of energies, when the Coulomb energy E_c corresponds to twice the surface energy E_s. Furthermore, Rayleigh claimed that for high charges higher multipole oscillations will become un-

stable and will provoke the emission of highly charged liquid in the form of fine jets.

The fissility parameter $X = E_c/2E_s$ characterises the relative contribution of repulsive (Coulomb) and cohesive (surface) energies to the fission barrier, separating between the bound initial states and the fission products. For $X < 1$, thermally activated fission over the barrier prevails. At the Rayleigh instability limit of $X = 1$, the barrier height is zero. Although many features of nuclear and metal cluster fission go beyond the physics of a classical liquid droplet and require the incorporation of quantum shell structure and dynamics, it is successfully applied to explain some of the main characteristics of such systems.

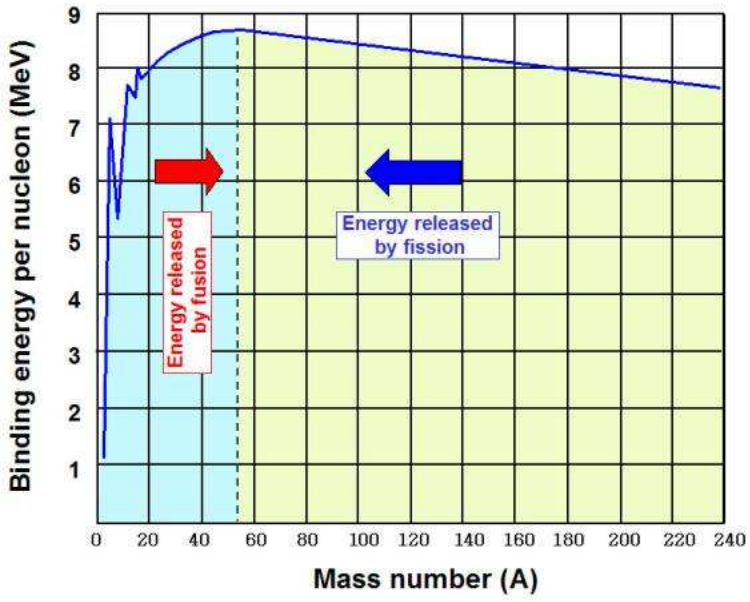

Figure 4.2: Curve showing the binding energy of nucleus as a function of number of nucleons [193].

Half a century after Lord Rayleighs publication, Bohr and Wheeler extended the model to explain the discovery of nuclear fission [185] in terms of a classical charged droplet where they assumed that the charge is distributed uniformly through out the volume. For their studies, they treated

the nucleus as a drop of incompressible nuclear fluid which implies that the nucleons are imagined to interact strongly with each other, like the molecules in a drop of liquid. This is a crude model that does not explain all the properties of nuclei, but does explain the spherical shape of most nuclei. It also helps to predict the binding energy of the nucleus which is given in Fig.4.3.1. Mathematical analysis of the theory delivers an equation which attempts to predict the binding energy of a nucleus in terms of the numbers of protons and neutrons it contains.

Bohr proposed that if one consider the total energy of a nucleus as the sum of a volume energy, surface energy and Coulomb energy, then the picture of a nucleus as a drop of liquid accounts for the observed variation of binding energy per nucleon with mass number. Because each bond energy is shared by two nucleons, each has a binding energy of one-half bond energy. When an assembly of spheres of the same size is packed together into the smallest volume, as we suppose is the case of nucleons within a nucleus, each interior sphere has 12 other spheres in contact with it. So, this energy is proportional to the volume and hence it is called volume energy. A nucleon at the surface of a nucleus interacts with fewer other nucleons than that one in the interior of the nucleus and hence its binding energy is less. The surface energy takes that into account and is therefore negative. The electric repulsion between each pair of protons in a nucleus also contributes toward decreasing its binding energy. The Coulomb energy of a nucleus is equal to the work that must be done to bring together the protons from infinity into a spherical aggregate the size of the nucleus. The Coulomb energy is negative because it arises from an effect that opposes nuclear stability.

Although a model like this could explain the features of the nuclear binding energy curve fairly well, it can be improved by taking into account two other energies that do not fit into the simple liquid-drop model but which are readily explainable in terms of a model that provides for nuclear energy lev-

els. They are asymmetry energy, an energy needed as a correction when the number of neutrons is greater than the number of protons and pairing energy, an energy which is a correction term that arises from the tendency of proton pairs and neutron pairs to occur (an even number of particles is more stable than an odd number). Including all these terms results in an equation for the nuclear binding energy which has five terms on its right hand side. These correspond to the cohesive binding of all the nucleons by the strong nuclear force, a surface energy term as explained above, the electrostatic mutual repulsion of the protons, an asymmetry term (derivable from the protons and neutrons occupying independent quantum momentum states) and a pairing term (partly derivable from the protons and neutrons occupying independent quantum spin states). If A is the total number of nucleons, Z the number of protons and N the number of neutrons, the binding energy of the nucleus is given by:

$$E_b = a_V A - a_S A^{2/3} - a_C \frac{Z(Z-1)}{A^{1/3}} - a_A \frac{(A-2Z)^2}{A} + \delta(A,Z) \qquad (4.61)$$

where a_V, a_S, a_C, a_A and δ are the parameters of the model. The nuclear droplet deforms through elongated shapes passing a barrier, ultimately develop into two separated fragments. When the fissility ratio $X = E_c/2E_s$ becomes 1 the barrier is zero. This is the Rayleigh limit. It was immediately understood that neutron induced fission would occur for fissilities smaller than 1 through the thermal activation of the barrier.

In analogy to atomic nuclei, metal clusters can be described as quantum liquid drops. The onset of instabilities of charged metal clusters has been studied by many groups both experimentally and theoretically [188–192] and the Rayleigh model has proven to be powerful to explain their instabilities. Most often the fission of charged metal clusters has been observed and studied

for $X < 1$ as a thermally activated process.

We developed a similar model to calculate the binding energy of both open ended and capped single-walled carbon nanotubes. The model is named liquid surface model because of the similarity of the suggested model to that used in the study of liquid droplets, nuclei, and atomic clusters. Similar models were already discussed for nanotubes [181, 182, 194–197] but the studies were limited only to specific types of nanotubes, namely zigzag and armchair. Contrary to the earlier studies, our model can be applied to nanotubes of arbitrary chirality and length. The major difference between liquid drop model and liquid surface model is that for single-walled nanotubes, the liquid surface model does not contain a volume energy part. The volume energy appears in the liquid surface model in the case of multiwalled nanotubes.

Liquid surface model, derivation of its parameters and the results which could be obtained with such a model are described in detail in the next chapter.

5

Liquid Surface Model

5.1 Introduction

This chapter gives a detailed description of liquid surface model and the results which are obtained using this model. The model is developed for two types of carbon nanotubes, namely, open-end nanotubes and capped nanotubes. First section of this chapter deals with open-end nanotubes. The parameters of liquid surface model for this kind of nanotubes are developed here and using these parameters the binding energy characteristics of open-end nanotubes are analysed.

The second section deals with a more realistic type of nanotubes, i.e, capped nanotubes. Derivation of the parameters for the capped nanotubes are described in detail and analysis of the binding energy characteristics are performed. The binding energies calculated using Brenner potential are compared with that obtained from the liquid surface model. The model is used to get some insights into the mechanism of growth of carbon nanotubes by considering the effect of catalyst particle on the binding energy of carbon nanotubes. Further, the elastic constants of carbon nanotubes are obtained using liquid surface model and it is compared with the known values.

5.2 Liquid surface model: Open-end nanotubes

Let us consider an open-end nanotube as shown in Fig. 5.1. According to the liquid surface model, the total energy of such a nanotube can be expressed as

a sum of three terms which are determined by the geometry of the nanotube, namely, the surface area, curvature of the surface, and the shape of the edge.

$$E = E_s + E_c + E_e. \tag{5.1}$$

In order to understand the origin of these three different energy contributions, consider a graphene sheet as shown in Fig. 2.2 in page 13.

The energy of this plane graphene sheet depends on the total number of atoms in it. For a graphene sheet of finite size, there are two kinds of carbon atoms: Atoms within the sheet and atoms at the edge of the sheet. Hence, the energy of the sheet depends on two quantities: Its surface area and the number of atoms at the edge. The extra energy of the edge arises from the dangling bonds of the carbon atoms at the edge. When the graphene sheet is rolled up to form a nanotube, two edges of the sheet meet each other resulting in closing of dangling bonds along those edges. This leads to a decrease of the edge energy in the nanotube compared to that in the corresponding graphene sheet. But at the same time, the rolling up of the graphene sheet causes an increase of the strain energy in a nanotube, i.e., elastic energy needed to roll a planar sheet up into a cylinder. The edge energy is directly proportional to the number of dangling bonds at the edge, which in the case of a nanotube is equal to the number of carbon atoms at the edge. For a nanotube of chirality (n, m), the number of carbon atoms at the edge is given by $n + m$.

In order to derive explicit expressions for the energy contributions, we define that an open-end nanotube consists of two parts: Two edges of length ΔX and an inner part of length L (see Fig. 5.1). ΔX is defined in such a manner that all carbon atoms with less than three bonds are part of it.

If N_i is the total number of carbon atoms in the inner part of the nanotube and N_e is that at one edge, the total number of atoms in the nanotube can

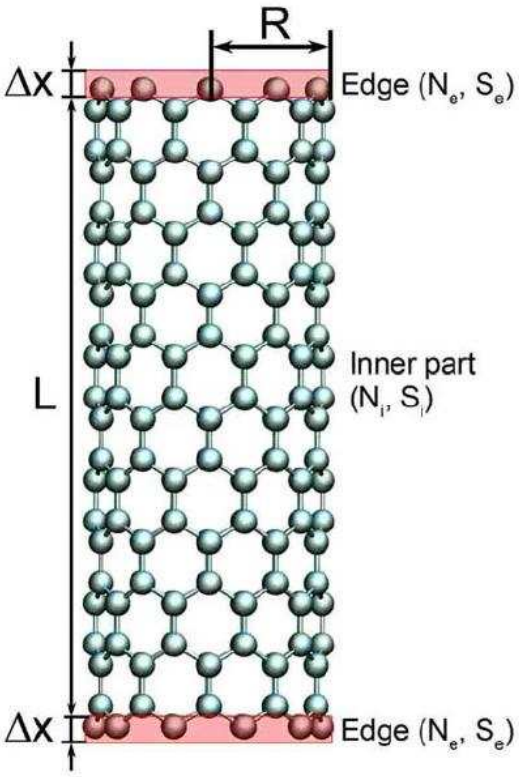

Figure 5.1: Different parts of an open-end carbon nanotube considered in the liquid surface model. ΔX is the width of the edge region of the nanotube which is marked by pink colour, N_e and S_e are the number of atoms in the edge region and the area of this region, respectively. N_i and S_i are the number of atoms in the inner region and its surface area. L and R are the length and radius of the nanotube [16].

be written as:

$$N = N_i + 2N_e \tag{5.2}$$

Let ρ_i be the area per atom in the inner region. Then the surface area of the inner region of the nanotube can be written as

$$S_i = 2\pi RL = \rho_i N_i = \rho_i N - 2\rho_i N_e. \tag{5.3}$$

Here, R is the radius of the nanotube and L is its length, as illustrated in Fig. 5.1. If σ is the surface energy density, σ_c is the curvature energy density

and ρ_e is the area per atom at the edge of the nanotube, then the surface, edge, and curvature energy terms can be written as follows:

$$E_s = \int_{S_i} \sigma \, dS = \sigma S_i \tag{5.4}$$

$$E_c = \int_0^{L+2\Delta \mathrm{X}} \sigma_c \frac{1}{R} dr = \sigma_c \frac{1}{R}(L + 2\Delta \mathrm{X}) = \epsilon_\mathrm{c} \frac{\mathrm{S_i} + 2\mathrm{S_e}}{\mathrm{R}^2} \tag{5.5}$$

$$E_e = 2\sigma \Delta \mathrm{X}(2\pi \mathrm{R}) = 2\sigma \rho_\mathrm{e} \mathrm{N_e} \tag{5.6}$$

Here, S_e is the area of one edge of the nanotube and ϵ_c is related to the specific curvature energy of a nanotube by the relation $\epsilon_c = \sigma_c/2\pi$. In deriving Eq. (5.5), we used the relation that $2\pi R(L + 2\Delta \mathrm{X}) = \mathrm{S_i} + 2\mathrm{S_e}$. Also, we assumed that the surface energy density, σ, is same throughout the nanotube. Substituting Eqs. (5.4), (5.5), (5.6) into Eq. (5.1), one derives:

$$E = \sigma S_i + \epsilon_c \frac{S_i + 2S_e}{R^2} + 2\sigma \rho_e N_e. \tag{5.7}$$

Substituting S_i from Eq. (5.3), one obtains:

$$E = \sigma \rho_i [N - 2N_e] + \epsilon_c \frac{\rho_i N - 2\rho_i N_e + 2\rho_e N_e}{R^2} + 2\sigma \rho_e N_e, \tag{5.8}$$

Rearranging the terms,

$$E = (\sigma \rho_i + \frac{\epsilon_c \rho_i}{R^2}) N + 2(\sigma \rho_e - \sigma \rho_i - \frac{\epsilon_c \rho_i}{R^2} + \frac{\epsilon_c \rho_e}{R^2}) N_e. \tag{5.9}$$

where $N_e = n + m$. The radius of the nanotube is determined by the chiral indices n and m,

$$R = \frac{\sqrt{3}\langle a \rangle}{2\pi} \sqrt{n^2 + m^2 + nm}. \tag{5.10}$$

where $\langle a \rangle$ is the average interatomic distance in the nanotube. The area

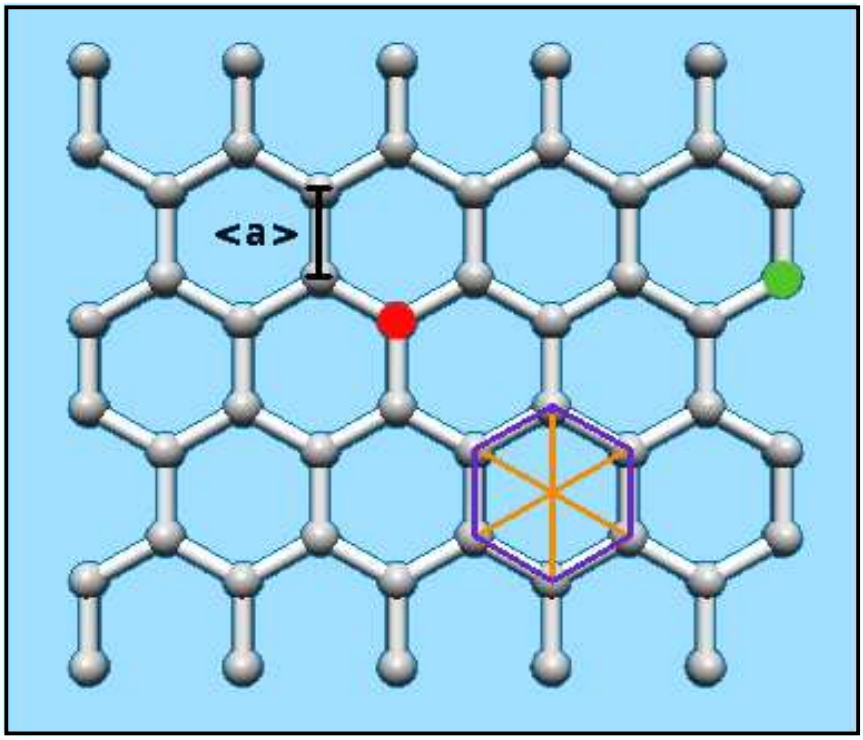

Figure 5.2: Area per atom in the inner and edge regions of a nanotube. The atom marked with red colour indicates an inner atom and that marked with green is an atom at the edge. $\langle a \rangle$ indicates the average bond length in a nanotube.

per atom in the inner region of a nanotube can be calculated as shown in Fig. 5.2. Each hexagonal ring contains 6 equilateral triangles whose area can be obtained by the formula:

$$A = \frac{1}{2}\langle a \rangle \frac{\sqrt{3}}{2}\langle a \rangle = \frac{\sqrt{3}}{4}\langle a \rangle^2 \tag{5.11}$$

Hence, the area of the hexagon becomes:

$$A_{hex} = 6\frac{\sqrt{3}}{4}\langle a \rangle^2 = \frac{3\sqrt{3}}{2}\langle a \rangle^2 \tag{5.12}$$

Each hexagon is shared by 6 atoms and each atom has 3 neighbouring

hexagons. Hence the area associated with an atom in the inner side of the nanotube becomes:

$$\rho_i = \frac{1}{6} \times 3 \times \frac{3\sqrt{3}}{2}\langle a\rangle^2 = \frac{3\sqrt{3}}{4}\langle a\rangle^2. \tag{5.13}$$

The area per atom at the edge of a nanotube is smaller and can be written as:

$$\rho_e = \alpha\rho_i, \tag{5.14}$$

where $\alpha \in [0...1]$ is a dimensionless parameter. Substituting Eqs. (5.10), (5.13), (5.14) into Eq. (5.9) and clubbing all constants, one obtains:

$$E = \sqrt{3}(\frac{3\langle a\rangle^2\sigma}{4} + \frac{\pi^2\epsilon_c}{n^2+m^2+nm})[N + 2(\alpha-1)(n+m)]. \tag{5.15}$$

As follows from Eq.(5.15), the total energy of an open-end nanotube depends on three parameters: The surface energy density σ, the specific curvature energy ϵ_c, and α, which defines the ratio of the area per edge atom to the area per atom in the inner region of a nanotube. These parameters are the same for all the nanotubes. If the total number of atoms and the chirality of a nanotube are known, the total energy and the binding energy per atom can be calculated using Eq.(5.15), once the parameters are known. The details of obtaining the parameters and the binding energy characteristics are described in the following subsections.

5.2.1 Parameters of the model

In order to determine the parameters σ, ϵ_c and α, we calculated the energies of open-end nanotubes with chiralities ranging from $n = 5$ to $n = 10$, where for each n, $0 \leq m \leq 5$ and total number of atoms lies in the range $N = 50 - 450$. These calculations are performed with both Tersoff and Brenner potentials. The packages used were MBN-explorer [198] and GULP [199]. By fitting

the numerically calculated values of energy with Eq. (5.15), we derived the values for the parameters σ, ϵ_c and α. The detailes of the procedure goes as follows:
Eq. (5.15) can be rewritten as:

$$\begin{aligned} E &= \sqrt{3}(\frac{3\langle a\rangle^2\sigma}{4} + \frac{\pi^2\epsilon_c}{n^2+m^2+nm})N \\ &\quad +2(\alpha-1)(n+m)\sqrt{3}(\frac{3\langle a\rangle^2\sigma}{4} + \frac{\pi^2\epsilon_c}{n^2+m^2+nm}). \end{aligned} \tag{5.16}$$

This is of the form of an equation for a straight line:

$$E = a(n,m)N + b(n,m), \tag{5.17}$$

where,

$$a(n,m) = \sqrt{3}(\frac{3\langle a\rangle^2\sigma}{4} + \frac{\pi^2\epsilon_c}{n^2+m^2+nm}) \tag{5.18}$$

$$b(n,m) = 2(\alpha-1)(n+m)\sqrt{3}(\frac{3\langle a\rangle^2\sigma}{4} + \frac{\pi^2\epsilon_c}{n^2+m^2+nm}). \tag{5.19}$$

Fig.5.3 shows this linear relationship between total energy and the total number of atoms N for a nanotube of chirality $n = 8, m = 3$. The slope of this curve gives the value of $a(n,m)$ and the y-intercept gives the value of $b(n,m)$.

The total energy is calculated using Tersoff and Brenner potentials and for each chirality the values of $a(n,m)$ and $b(n,m)$ are obtained by fitting the total energy with Eq. (5.17). Once $a(n,m)$ and $b(n,m)$ are obtained, the parameters of the liquid surface model are calculated by fitting the calculated values of $a(n,m)$ and $b(n,m)$ with the functions defined in Eqs. (5.18)-(5.19). Once these parameters are obtained, Eqs. (5.18)-(5.19) can be used to calculate the values of $a(n,m)$ and $b(n,m)$ for arbitrary values of n and m. These

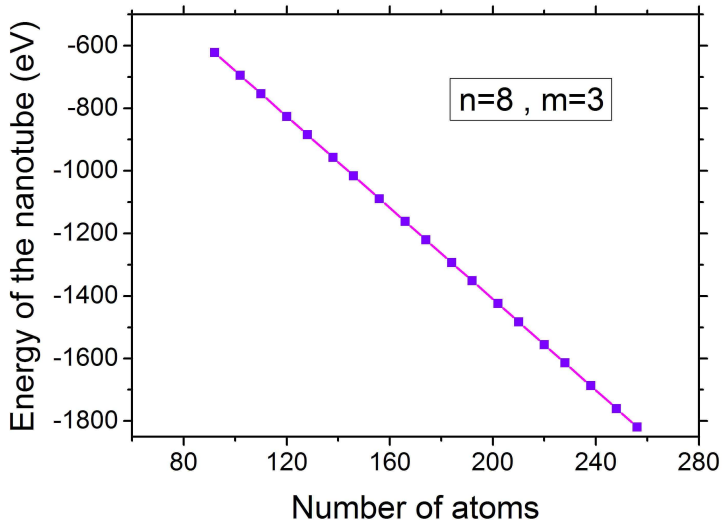

Figure 5.3: Linear relationship between total energy of the nanotube and the total number of atoms N, shown for a nanotube of chirality $n = 8, m = 3$. The slope of this curve gives the value of $a(n, m)$ and the y-intercept gives the value of $b(n, m)$.

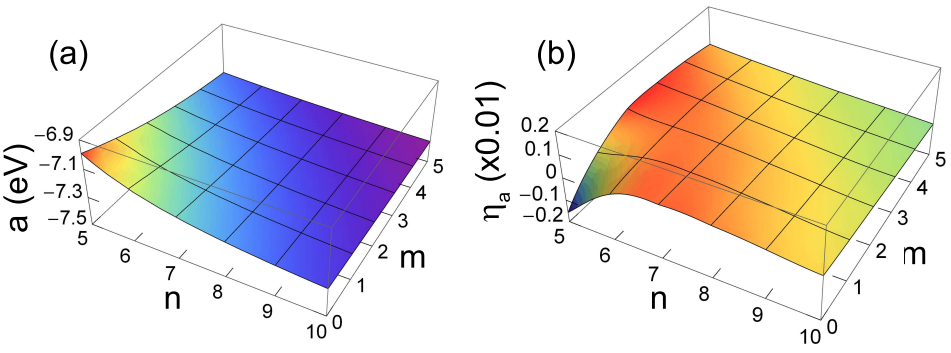

Figure 5.4: (a) Parameter a as a function of n and m. (b) Relative deviation of $a(n, m)$ from the liquid surface model prediction $a(n, m)^{fit}$. The relative deviation η_a is defined in Eq. (5.20)

values are denoted as $a(n, m)^{fit}$ and $b(n, m)^{fit}$. In order to check the accuracy of the fitting, we have calculated the relative deviation of $a(n, m)$ and $b(n, m)$ from the corresponding values $a(n, m)^{fit}$ and $b(n, m)^{fit}$. The relative

deviations of $a(n,m)$ and $b(n,m)$ read as follows:

$$\eta_a = \frac{a(n,m) - a(n,m)^{fit}}{a(n,m)} \tag{5.20}$$

$$\eta_b = \frac{b(n,m) - b(n,m)^{fit}}{b(n,m)} \tag{5.21}$$

Figures 5.4 and 5.5 show the dependencies of $a(n,m)$ and $b(n,m)$ on n and m as well as their relative deviations from the liquid surface model predictions.

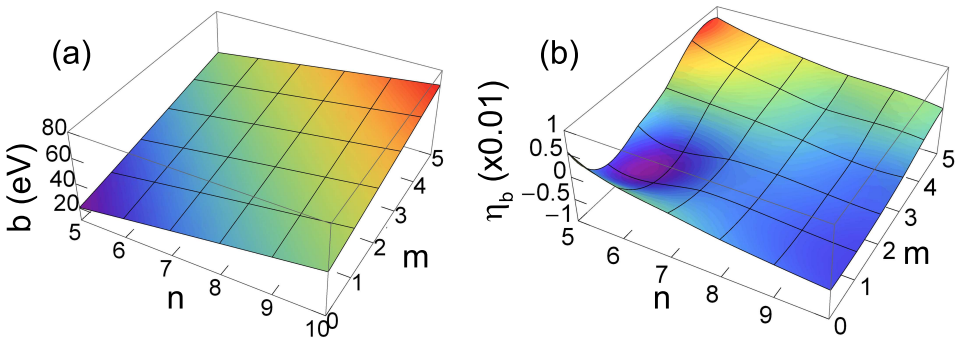

Figure 5.5: (a) Parameter b as a function of n and m. (b) Relative deviation of $b(n,m)$ from the liquid surface model prediction $b(n,m)^{fit}$. The relative deviation η_b is defined in Eq. (5.21)

Figure 5.4(a) shows that $a(n,m)$ behaves monotonously with n and m and its value approaches the limiting value, as n and m increases. Figure 5.4(b) shows the relative deviation of $a(n,m)$ from the value predicted by the liquid surface model, which appear to be less than 0.2%. This is important because it shows that the liquid surface model reproduces correctly the major contribution to the energy of the system. It is also worth noting that at larger chiralities (e.g. $n = 10$, $m = 5$), the relative deviation converges to zero, indicating that the liquid surface model should be well applicable for nanotubes with large chiral numbers. Figure 5.5(a) shows that $b(n,m)$ changes smoothly with n and m and its behaviour is almost planar. Fig-

ure 5.5(b) shows that the relative deviation in the value of $b(n, m)$ from the value predicted by the liquid surface model, Eq. (5.21), is less than 1.0%.

The values of the parameters σ, ϵ_c and α obtained for open-end nanotubes are compiled along with the parameters for capped nanotubes in Table 5.2 in page 108.

5.2.2 Binding energy per atom

As predicted by the liquid surface model the total binding energy of an open-end carbon nanotube is given by Eq. (5.15). The binding energy per atom reads as:

$$\epsilon = \frac{E}{N} \tag{5.22}$$

where E is the total energy of a nanotube and N is the total number of atoms in it. The result of comparison of the binding energy per atom predicted by the liquid surface model and that calculated using the Tersoff potential for the open-end nanotubes is illustrated in Fig. 5.6 and Fig. 5.7, which shows the dependence of the binding energy on the total number of atoms in the system.

Different symbols in Fig. 5.6 and Fig. 5.7 represent the values calculated using the Tersoff potential and the lines near the corresponding symbols show the predictions of the liquid surface model.

Figure. 5.6 and Fig. 5.7 show that nanotubes become more stable as their length increases. This happens because of the nanotube's edge. If L is the length of a nanotube and R is its radius, one can introduce a parameter to characterise the effect of the edge of a nanotube as follows:

$$\zeta = \frac{2\pi R}{L} \tag{5.23}$$

If $\zeta \simeq 1$, the edge has a major influence on the nanotube energetics because

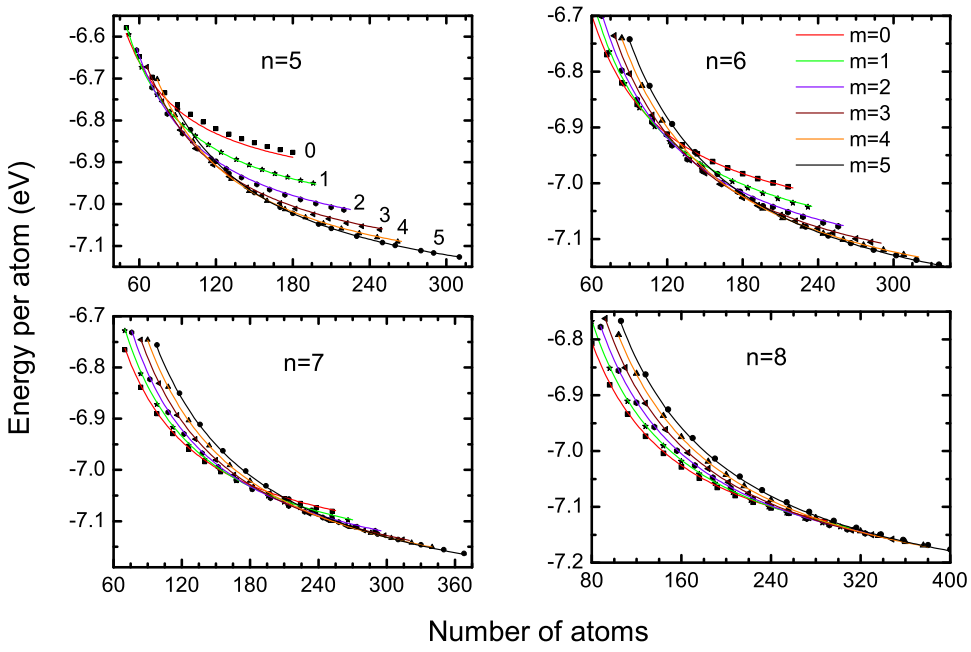

Figure 5.6: Comparison of the binding energy per atom calculated using the Tersoff potential and that obtained from the liquid surface model for the open-end nanotubes. The curves show the values predicted by the model and different symbols correspond to the calculated values. The plots are shown for $n = 5 - 8$. Each curve in one plot corresponds to a different m value [16].

in this case the size of the edge becomes comparable with the size of the inner part of the nanotube. As the nanotube grows in length, the parameter ζ, Eq. (5.23), decreases and in the limiting case (infinitely long nanotube) it reaches zero, reflecting the fact that influence of the edge diminishes.

Another important feature shown in Fig. 5.6 and Fig. 5.7 is that the energetically favourable chirality of a nanotube depends on the total number of carbon atoms in it. As the total number of atoms increases, nanotubes with larger chiralities (higher radii) become energetically more favourable, whereas nanotubes of smaller radii are energetically favourable at smaller

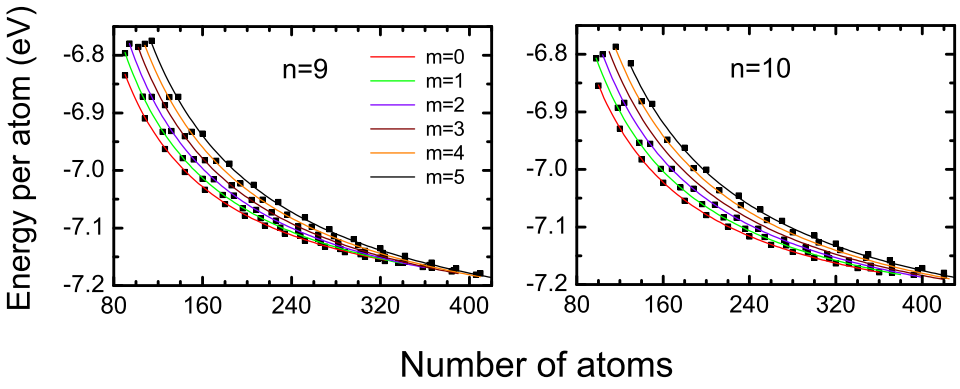

Figure 5.7: Comparison of the binding energy per atom calculated using the Tersoff potential and that obtained from the liquid surface model for the open-end nanotubes. The curves show the values predicted by the model and the squares correspond to the calculated values. The plots are shown for $n = 9 - 10$. Each curve in one plot corresponds to a different m value [16].

lengths. See, for example, top right plot in Fig: 5.6 where this fact is clearly seen for nanotubes with $n = 6$. When the total number of atoms in this example is less than 100, the binding energy per atom decreases with increase of m, while an opposite behaviour is observed when the total number of atoms in the nanotube exceeds 180. This fact has a simple explanation. For a given number of atoms the length of a nanotube decreases if the radius of nanotube grows. Therefore, for nanotubes with smaller number of atoms (e.g., less than 100 for the $n = 6$ case), smaller value of the chirality number m are energetically more favourable, because the edge to length ratio ζ, Eq. (5.23) is smaller than in the case of nanotubes with larger m value. If $L \gg R$, then the edge of a nanotube has minor influence on its energetics. Therefore, nanotubes of larger radius should become energetically more favourable, since the curvature energy in this case is smaller.

In order to conclude about the accuracy of the liquid surface model, we determined the relative deviation of the binding energy per atom predicted

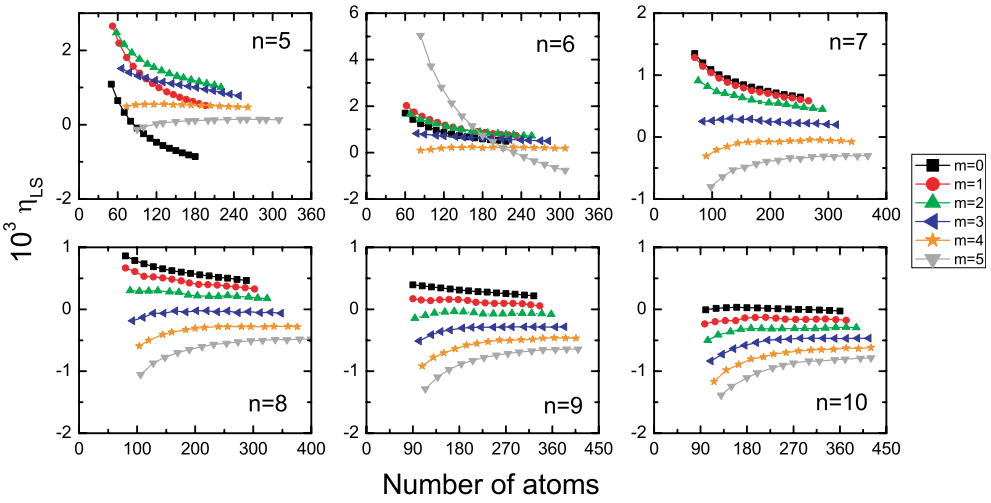

Figure 5.8: Relative deviation of the liquid surface model predictions of the binding energy per atom from that calculated using the Tersoff potential, Eq. (5.24), for the open-end nanotubes. Plots are shown for $n = 5 - 10$. Each curve in one plot corresponds to different m values [16].

by the liquid surface model from the binding energy per atom calculated using the Tersoff potential, which is defined as follows:

$$\eta_{LS} = \frac{\epsilon - \epsilon_{LS}}{\epsilon_{LS}} \tag{5.24}$$

where ϵ_{LS} and ϵ are the binding energy per atom obtained from the liquid surface model and from calculations using the Tersoff potential respectively.

Figure. 5.8 shows the relative deviation, η_{LS}, for nanotubes of different chiralities. In each plot, different curves correspond to different m values. The maximum relative deviation is found to be $\sim 0.6\%$. This illustrates that the liquid surface model is successful and can be used for predicting the energy of nanotubes.

The discussed model neglects the van der Waals energy between the atoms of a nanotube. In order to understand how the van der Waals interaction affects the energetics of the nanotube, we have calculated the van der Waals

energy per atom for nanotubes with $n = 5$ to $n = 10$ for arbitrarily selected m values. The parameters of the van der Waals interaction are taken from Ref [200]. The van der Waals interaction between carbon atoms was parametrised with the Lennard-Jones potential with the equilibrium distance equal to 3 Å and the minimum energy 0.52 meV, as suggested in Ref [200] for fullerenes. The van der Waals interaction was calculated between all non-neighboring atoms, which were defined as atoms being more than 1.6 Å away from each other.

It has been observed that the van der Waals energy per atom is $\sim 17 - 43$ meV for all nanotubes, while the binding energy per atom is $\sim 6.6 - 7.2$ eV. Therefore, the van der Waals energy in nanotubes is almost negligible and we neglect it in our model.

5.3 Comparison with DFT calculations

Tersoff potential is a many body phenomenological potential with 13 parameters. In our calculations, we used the parameters for carbon systems from Ref. [177]. In order to establish the accuracy of the Tersoff potential the binding energies per carbon atom calculated using the Tersoff potential are compared with those obtained from *ab initio* DFT calculations for nanotubes of different chiralities. The definition of the binding energy per carbon atom calculated using the Tersoff potential is different from that calculated within the framework of the DFT. To calculate the energy of a nanotube using DFT, extra hydrogen atoms should be added at both edges of the nanotube in order to fulfill the valency requirement, otherwise DFT calculations become impossible because convergence problems arise while solving the self consistent field equations. The binding energy per carbon atom calculated within the framework of the DFT is defined as:

$$\epsilon_{B3LYP} = \frac{E_{B3LYP} - [E_C N_C + E_H N_H + E_{CH} N_{CH}]}{N_C}, \tag{5.25}$$

where E_{B3LYP} is the total energy of the nanotube. E_C, E_H and E_{CH} are the energies of a single carbon atom, hydrogen atom and a single carbon-hydrogen bond respectively, whereas N_C, N_H and N_{CH} are the total numbers of carbon atoms, hydrogen atoms and carbon-hydrogen bonds. Since the carbon and hydrogen atoms are bound via single bonds, $N_H = N_{CH}$. The energies of a single carbon and hydrogen atoms are obtained from *ab initio* calculations using the B3LYP density functional combined with the standard 6-31G(d) basis set [201]. The energy of a carbon-hydrogen bond is calculated from the energies of the benzene molecule (C_6H_6) and a benzene molecule with one hydrogen atom removed (C_6H_5). If $E_{C_6H_6}$ is the total energy of the benzene molecule and $E_{C_6H_5}$ is that of the benzene molecule with only five hydrogen atoms, the energy of a carbon-hydrogen bond can be obtained as:

$$E_{CH} = E_{C_6H_6} - (E_{C_6H_5} + E_H). \tag{5.26}$$

E_C (a.u.)	E_H (a.u.)	$E_{C_6H_6}$ (a.u.)	$E_{C_6H_5}$ (a.u.)	E_{CH} (a.u.)
-37.77601	-0.50027	-232.24865	-231.56128	-0.187098

Table 5.1: Energies of the C, H atoms, C_6H_6, C_6H_5 molecules and $C-H$ bond, calculated with the use of the B3LYP density functional.

The energy values E_C, E_H, $E_{C_6H_6}$, $E_{C_6H_5}$ and E_{CH} are compiled in Tab. 5.1.

To establish accuracy of the Tersoff potential, we have calculated the energy with this potential for several nanotubes, which were initially optimized with the use of the B3LYP method. For the Tersoff potential calculations the additional hydrogen atoms at the edges of the nanotubes were removed. Therefore the binding energy per carbon atom calculated with this method

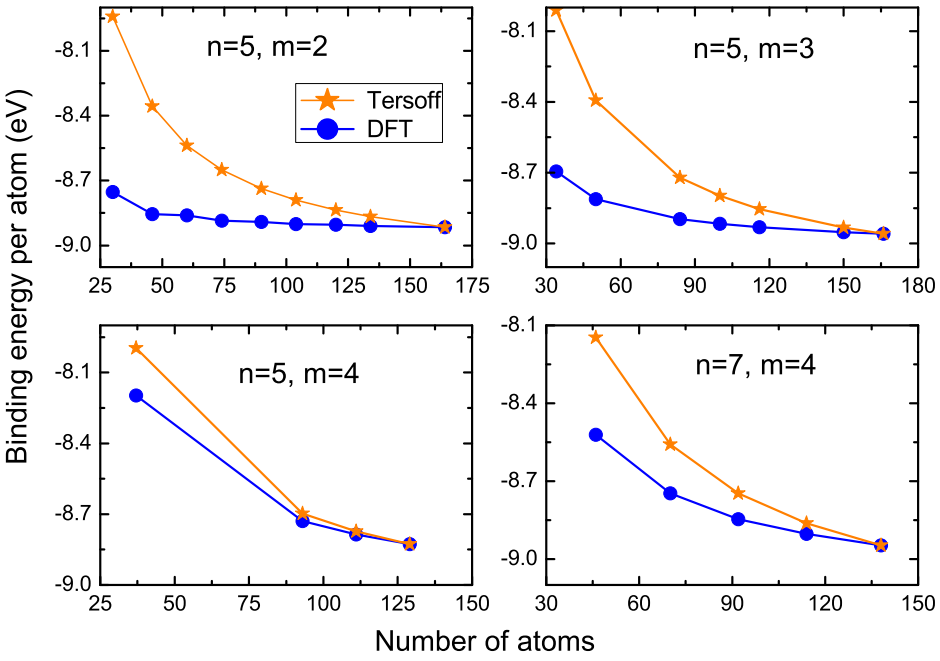

Figure 5.9: Comparison of binding energy per carbon atom for nanotubes of different chiralities obtained from DFT calculations, Eq. (5.25), and calculation using Tersoff potential, Eq. (5.27). The stars show values obtained using the Tersoff potential shifted by a constant value and the dots show the values obtained from DFT calculations.

is defined as:

$$\epsilon_{tersoff} = \frac{E_{tersoff}}{N_C}, \tag{5.27}$$

where $E_{tersoff}$ is the total energy calculated using the Tersoff potential. The binding energies per carbon atom calculated within the framework of the DFT and using the Tersoff potential are shown in Fig. 5.9. For the sake of comparison, the binding energies obtained using the Tersoff potential are shifted such that the binding energies of the largest nanotubes calculated in both methods coincide. From Fig. 5.9, it is clear that for a nanotube of a given chirality, the deviation between the energies calculated using the Tersoff

potential and that calculated using DFT methods reduces as the number of atoms in the nanotube grows. This arises as a result of the effect of edge.

The effect of the edge can be characterised by the parameter ζ, Eq. (5.23). If $\zeta \simeq 1$, the edge has a major influence on the nanotube energetics because in this case the size of the edge becomes comparable with the size of the inner part of the nanotube. As the length of the nanotube increases, the edge effect becomes smaller and ζ decreases. To illustrate this point, consider the nanotube with $n = 5$ and $m = 2$ (first plot in Fig. 5.9). The radius of this nanotube calculated according to Eq. (5.10) is 2.367 Å. The length of this nanotube varies from 5.0 Å till 27 Å and the corresponding value of ζ changes from 2.973 to 0.551.

Another important feature observed in Fig. 5.9 is that as the radius of the nanotube increases the results of the DFT and the Tersoff potential calculations approach each other. This feature can be explained as follows. In a graphene sheet, the bonds between carbon atoms have purely sp^2 hybridization. As a nanotube is formed from a graphene sheet, the curvature of the tube causes the bonds to deviate from being purely sp^2 in nature.

DFT calculations take this fact into account but the Tersoff potential is not capable of describing this effect correctly, since it is parameterised for pure sp^2 and sp^3 hybridised systems. This suggests that the Tersoff potential gives more accurate results for nanotubes of higher radii than those of smaller radii.

5.4 Liquid surface model: Capped nanotubes

The liquid surface model can also be applied to the study of capped nanotubes. In this case, the total energy of a nanotube reads as:

$$E = E_s^{tube} + E_c^{tube} + E_s^{cap} + E_c^{cap} + E_e, \tag{5.28}$$

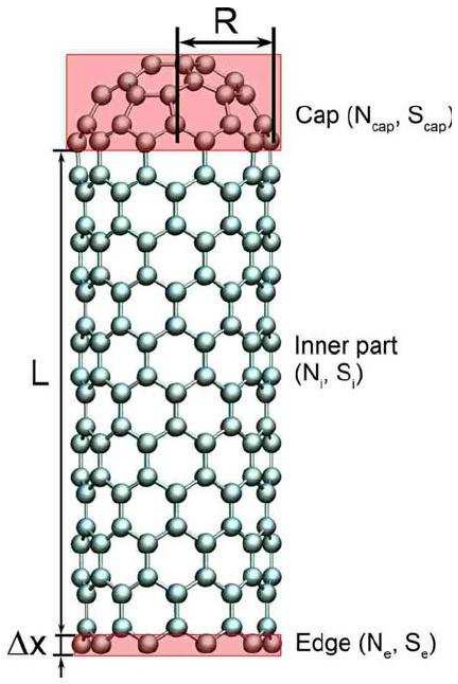

Figure 5.10: Different parts of a capped carbon nanotube considered in the liquid surface model. ΔX is the width of the edge region of the nanotube which is marked by pink colour, N_e and S_e are the number of atoms in the edge region and the area of this region, respectively. N_i and S_i are the number of atoms in the inner region and its surface area. L and R are the length and radius of the nanotube. N_{cap} and S_{cap} are the number of atoms in the cap and its surface area [16].

where E_s, E_c and E_e are the energies of the surface, curvature, and the edge, respectively. Superscripts "tube" and "cap" refer to the cylindrical and cap parts of the nanotube, respectively. The total number of atoms in a capped nanotube can be written as:

$$N = N_i + N_e + N_{cap}, \tag{5.29}$$

where N_i, N_e and N_{cap} are the number of carbon atoms in the inner part of the nanotube, at the edge and in the cap. The number of carbon atoms in

the cap reads as:

$$N_{cap} = \frac{S_{cap}}{\rho_{cap}} = \frac{2\pi R^2}{\rho_{cap}}. \tag{5.30}$$

Here S_{cap} is the surface area of the cap and ρ_{cap} is the area per atom in the cap. The surface energy term of a nanotube with a cap can thus be written as:

$$E_s^{tube} = \sigma\rho_i N_i = \sigma\rho_i(N - N_{cap} - N_e) = \sigma\rho_i(N - \frac{2\pi R^2}{\rho_{cap}} - N_e). \tag{5.31}$$

Since a capped nanotube has only one edge, the curvature energy term reads as:

$$\begin{aligned} E_c^{tube} &= \sigma_c \int_0^{L+\Delta \mathrm{X}} \frac{1}{R} dr = \sigma_c \frac{1}{R} \frac{S_i + S_e}{2\pi R} \\ &= \frac{\epsilon_c \rho_i}{R^2} N + \frac{\epsilon_c(\rho_e - \rho_i)}{R^2} N_e - \frac{2\pi\epsilon_c\rho_i}{\rho_{cap}}. \end{aligned} \tag{5.32}$$

In deriving Eq. (5.32), we used the following two relations:

$$2\pi R(L + \Delta \mathrm{X}) = S_i + S_e \tag{5.33}$$

$$\epsilon_c = \frac{\sigma_c}{2\pi} \tag{5.34}$$

The edge energy term in Eq. (5.28) is defined as:

$$E_e = \sigma \Delta \mathrm{X}(2\pi \mathrm{R}) = \sigma \rho_{\mathrm{e}} \mathrm{N_e}. \tag{5.35}$$

Fig. 5.11 illustrates how to obtain the surface and curvature energies of the cap in Eq. (5.28). Here, the cap is assumed to be a semisphere of radius R, which is the radius of the nanotube.

$$E_s^{cap} = \int_{S_{cap}} \sigma dS = \sigma S_{cap} = 2\pi\sigma R^2, \tag{5.36}$$

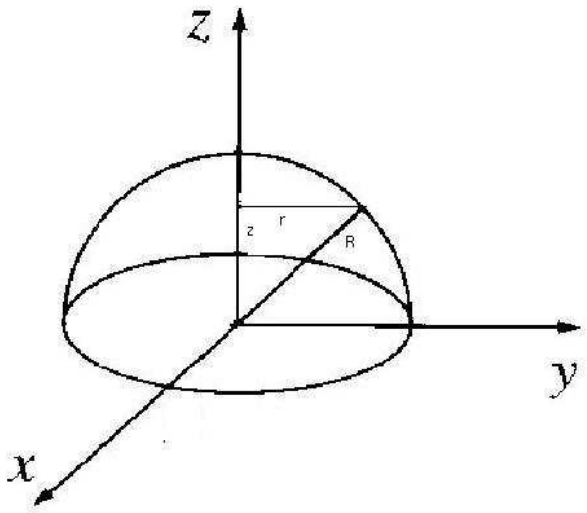

Figure 5.11: Obtaining the surface and curvature energies of the cap of a nanotube, which is assumed to be a semi-sphere of radius R. In order to get the curvature of the cap, the integration is performed along the Z-axis from z=0 to z=R.

$$E_c^{cap} = \int_0^R \sigma_c^{cap} \frac{1}{r} dz = \sigma_c^{cap} \int_0^R \frac{1}{\sqrt{R^2 - z^2}} dz = \epsilon_c^{cap}. \tag{5.37}$$

where $\epsilon_c^{cap} = \frac{\pi}{2}\sigma_c^{cap}$. Substituting Eqs. (5.31)–(5.32) and Eqs. (5.35)–(5.37) into Eq. (5.28), one derives

$$\begin{aligned} E = (\sigma\rho_i + \frac{\epsilon_c\rho_i}{R^2})N &+ (\sigma(\rho_e - \rho_i) + \frac{\epsilon_c(\rho_e - \rho_i)}{R^2})N_e \\ &+ \frac{2\pi\sigma}{\rho_{cap}}(\rho_{cap} - \rho_i)R + 2\pi\epsilon_c^{cap} - \frac{2\pi\epsilon_c\rho_i}{\rho_{cap}}. \end{aligned} \tag{5.38}$$

The area per atom in the inner part of the nanotube can be related with the area per atom in the cap as follows:

$$\rho_i = \gamma\rho_{cap}. \tag{5.39}$$

Substituting Eq. (5.10), (5.13), (5.14) and Eq. (5.39) into Eq. (5.38) and clubbing all constants, one obtains

$$E = \sqrt{3}(\frac{3\langle a\rangle^2\sigma}{4} + \frac{\pi^2\epsilon_c}{n^2+m^2+nm})[N + (\alpha-1)(n+m)] \\ + \frac{3\langle a\rangle^2\sigma}{2\pi}(1-\gamma)(n^2+m^2+nm) + 2\pi(\epsilon_c^{cap} - \epsilon_c\gamma). \quad (5.40)$$

The last two terms in Eq. (5.40) account for the structure of the nanotube cap, while the first term corresponds to the energy of an open-end nanotube with one edge. Thus the energy of a capped nanotube is determined by the five parameters: Surface energy density σ, the specific curvature energies ϵ_c and ϵ_c^{cap}, as well as parameters α and $1/\gamma$ defining the ratio of the area per edge atom and the area of an atom in the cap to the area per atom in the inner region of a nanotube.

5.4.1 Parameters of the model

Parameters of the capped nanotubes are obtained exactly the same way as that is obtained for open-end nanotubes in section 5.2.1. The only difference between a capped nanotube and an open-end nanotube is the additional two parameters which are used to obtain the energies of the cap. The addition of a cap brings in some difficulty for the construction of a nanotube. Hence, we have used the following procedure for the nanotube cap construction. A nanotube of chirality (n, m) has $n+m$ atoms at the edge which should form bonds with the cap. The cap should be one-half of a fullerene with the radius equal to the radius of the nanotube. The construction of the fullerene starts either from a hexagon or a pentagon and is continued by adding hexagons and pentagons sequentially row by row around the initial one. This procedure has been well described, e.g., in Ref. [202]. For the C_{60} family of fullerenes (e.g., C_{60}, C_{240}, C_{720}), only certain radii are possible and therefore only some chiralities can be capped with an ideal semifullerene. To construct a cap for

Nanotube	Potential	σ (eV/Å)	ϵ_c (eV)	ϵ_c^{cap} (eV)	α	γ
Open-end	Tersoff	-2.8669	0.5879		0.6925	
Open-end	Brenner	-2.8563	0.3553		0.6902	
Capped	Brenner	-2.8564	0.3550	0.6624	0.6900	0.9998

Table 5.2: Values for the parameters σ, ϵ_c, ϵ_c^{cap}, α and γ used in the liquid surface model for open-end and capped nanotubes [16].

arbitrary chirality one needs to introduce one or several defects (for example, to place a pentagonal ring instead of a hexagonal one) in the cap structure. In the present thesis we demonstrate this on several examples.

To calculate parameters of the liquid surface model for capped nanotubes we considered structures with chiralities (5,0); (6,0); (5,5); (9,0); (10,0); (6,6); (12,3); (10,10); (15,15); (19,0); (11,11); (23,0); (16,16); (28,0), containing $N = 50 - 3000$ atoms.

The calculated values of the parameters of liquid surface model are compiled in Table 5.2 for both open-end $(\sigma, \epsilon_c, \alpha)$ and capped $(\sigma, \epsilon_c, \epsilon_c^{cap}, \alpha, \gamma)$ nanotubes. For the calculation of the open-end nanotubes we used both Tersoff and Brenner potentials, while the capped nanotubes were studied with the use of the Brenner potential only.

Parameters σ, ϵ_c and α should be the same for the open-end and capped nanotubes. From Table 5.2, it follows that for both cases parameters σ, α and ϵ_c are very close to each other in the case of calculations with Brenner potential.

It is also worth noting that parameter γ is very close to unity, indicating that the area per atom in the inner part of a nanotube is almost the same as the area per atom in the cap as follows from Eq. (5.39).

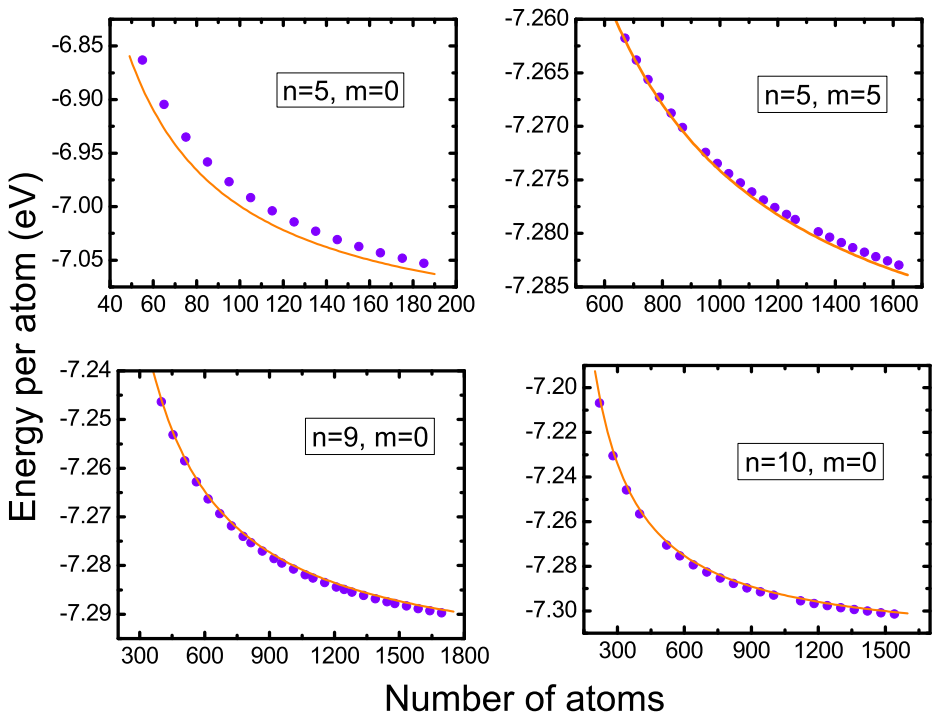

Figure 5.12: Comparison of the binding energy per atom calculated using the Brenner potential and that obtained from the liquid surface model for the capped nanotubes. The curves show the values predicted by the model and dots correspond to the calculated values. The chirality of the nanotubes is indicated in the inset to the plots [16].

5.4.2 Binding energy per atom

Figure. 5.12–5.14 show the dependence of the binding energy per atom on the nanotube size calculated for the capped nanotubes with the use of the Brenner potential. In Figure. 5.16, the relative deviation of the binding energy per atom predicted by the liquid surface model from the corresponding values calculated with the use of the Brenner potential is illustrated.

Figure. 5.12–5.14 show that the binding energy per atom for the capped

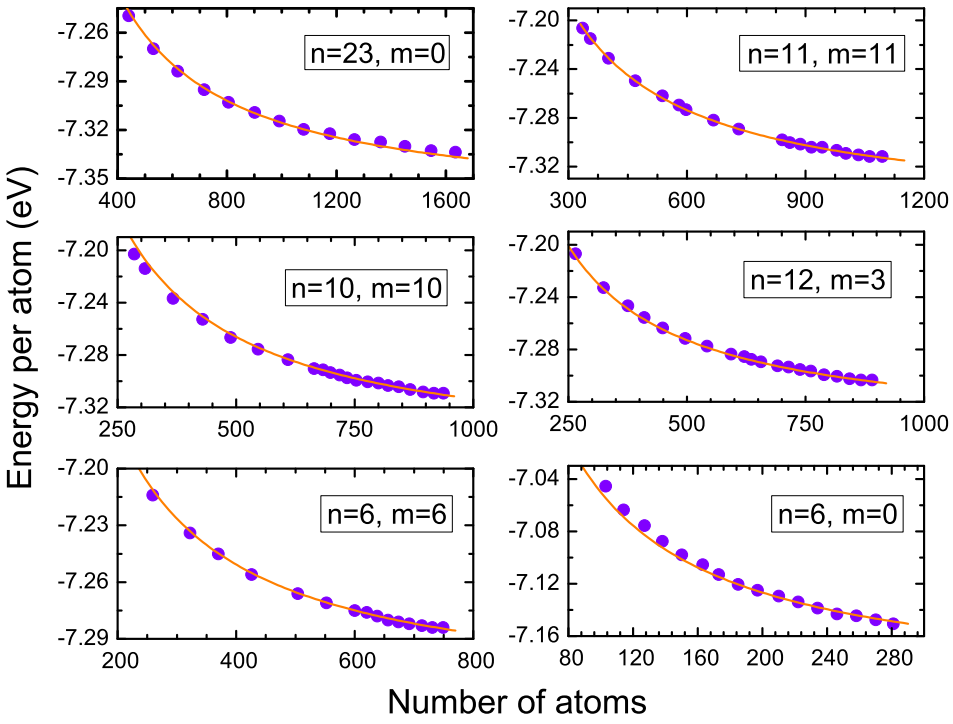

Figure 5.13: Comparison of the binding energy per atom calculated using the Brenner potential and that obtained from the liquid surface model for the capped nanotubes. The curves show the values predicted by the model and dots correspond to the calculated values. The chirality of the nanotubes is indicated in the inset to the plots [16].

nanotubes decreases with the increase of the nanotube length demonstrating the fact that longer nanotubes are energetically more favourable than the shorter ones. The reason behind this is the edge effect which is described in detail in the case of open-end nanotubes (see Sec.5.2.2). The relative deviation η_{LS}, Eq. (5.24), for the capped nanotubes, shown in Fig. 5.16 is below 0.3%, corresponding to the absolute energy difference of less than 0.01 eV= 116 K. This energy difference is much below the energy of thermal vibrations in the system because the typical nanotube growth temperature

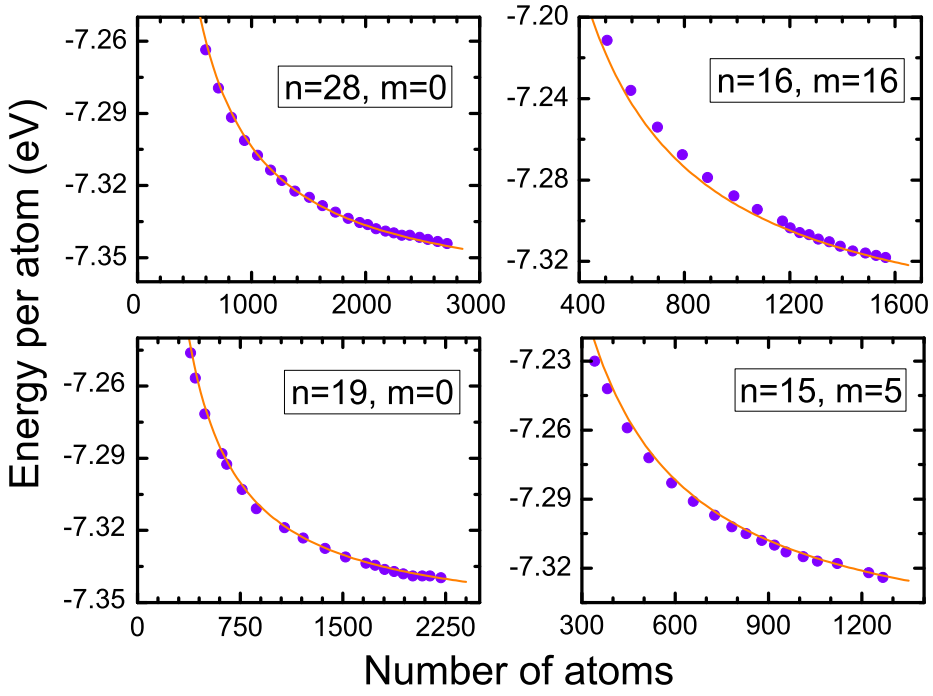

Figure 5.14: Comparison of the binding energy per atom calculated using the Brenner potential and that obtained from the liquid surface model for the capped nanotubes. The curves show the values predicted by the model and dots correspond to the calculated values. The chirality of the nanotubes is indicated in the inset to the plots [16].

is about $700 - 1200$ K (see, e.g., Refs. [37, 203, 204]).

From Fig. 5.16, it can be noted that the relative deviation of energy is larger for shorter nanotubes. This happens because we neglect the cap deviation from a semisphere. Indeed, for shorter nanotubes the cap has a stronger impact on the binding energy per atom and therefore accounting for its deformation in this case becomes much more important.

Fig. 5.15 compares the binding energies per atom calculated for the capped and open-end nanotubes of close sizes with chiralities (5,0) and (28,0).

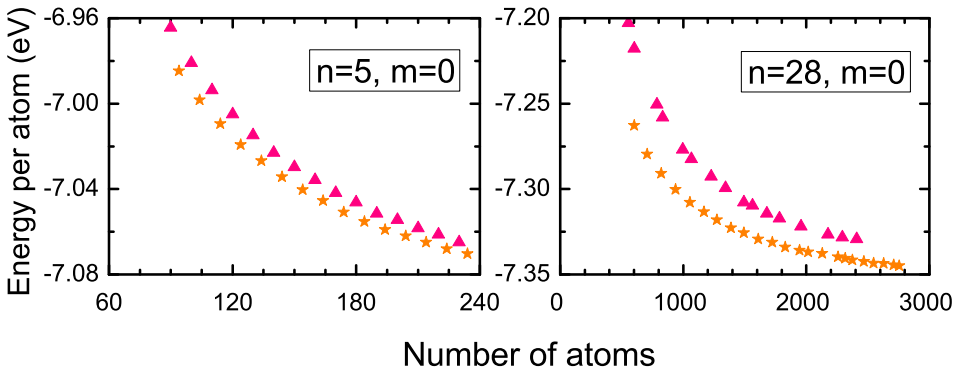

Figure 5.15: Binding energy per atom calculated for capped (stars) and open-end (triangles) nanotubes of close sizes with chiralities (5,0) and (28,0). The chirality of the nanotubes is indicated in the inset to the plots [16].

The comparison shows that the binding energy per atom for the open-end nanotubes is higher than the binding energy per atom for the capped nanotubes because open-end nanotubes have more dangling bonds at the edge and therefore energetically less favourable. The differences in energies of open-end and capped nanotubes arise only for nanotubes of finite length where the edge atoms play an important role, while for infinitely long structures the binding energies per atom are identical. This behaviour is seen in Fig. 5.15, where the difference between the binding energy per atom for the open-end and capped nanotubes is higher for shorter nanotubes than for the longer ones.

5.5 Comparison of Tersoff and Brenner potentials

It is believed that Brenner potential accounts more accurately for the π-bondings in the system, and therefore is better for the description of carbon nanotubes [159, 205, 206]. To stress the differences between the Tersoff and Brenner potentials, in Fig. 5.17 we compare the binding energy per atom

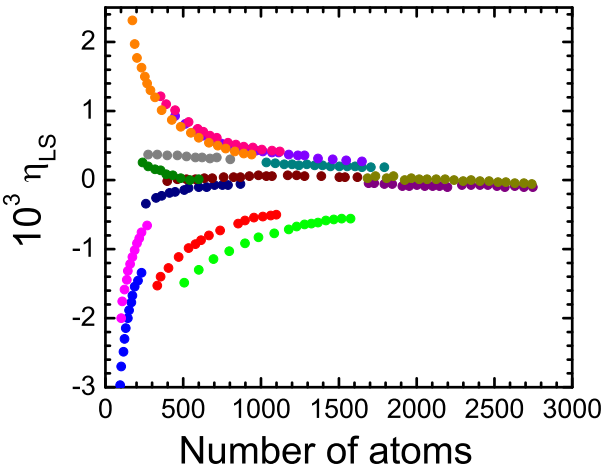

Figure 5.16: Relative deviation of the liquid surface model predictions of the binding energy per atom from that calculated using the Brenner potential, Eq. (5.24), for the capped nanotubes. Each colour in the plot corresponds to a certain nanotube of a given chirality [16].

with the use of both methods for capped nanotubes of several chiralities. Fig. 5.17 shows that the binding energy per atom calculated with the use of Tersoff potential is lower than binding energy per atom calculated with the use of Brenner potential. The energy difference is decreasing with the radius of the nanotube and is approximately equal to 0.13 eV, 0.08 eV, 0.03 eV, and 0.02 eV for nanotubes with chiralities (5,0), (6,0), (5,5) and (9,0), respectively, being less than 1 % of the absolute value of the binding energy per atom in the nanotube.

The comparison in Fig. 5.17 demonstrates that the difference between the energies calculated with the use of Brenner and Tersoff potentials decreases with the nanotube radius leading to a conclusion that for nanotubes of higher radii (i.e., with chirality (19,0) or (28,0)) it should be almost negligible and both potentials become equivalent. However on the basis of the calculated differences of the binding energies it is impossible to judge which

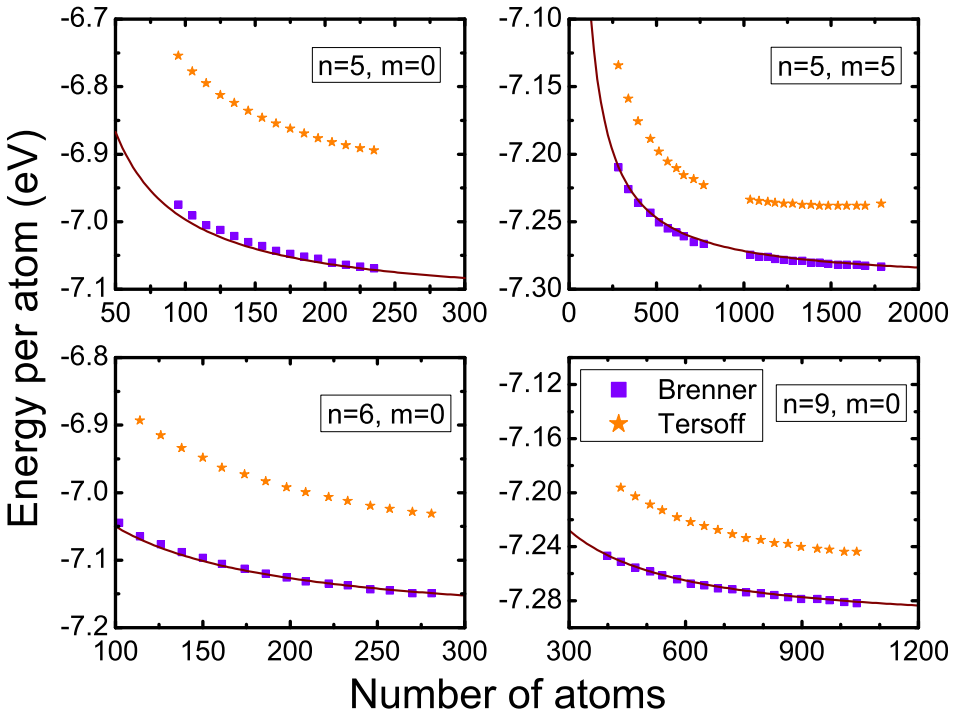

Figure 5.17: Comparison of the binding energy per atom calculated using Brenner (squares) and Tersoff (stars) potentials for capped nanotubes with chirality (5,0); (5,5); (6,0); (9,0). The line shows the binding energy per atom calculated using the liquid surface model [16].

potential describes nanotubes more accurately because the asymptotic of the potentials depends on the form of the parametrisation. In order to make the judgement on the quality of Brenner and Tersoff potentials we have used the calculated energies to determine the curvature constant and Young modulus for single-wall carbon nanotubes and compared the obtained values with available experimental data and results of earlier calculations.

5.6 Elastic properties from liquid surface model

To relate the calculated energies to elastic properties of nanotubes let us consider a graphene sheet which can bend to form a nanotube of radius R. Within the framework of a continuum elastic model the curvature energy of the sheet can be written as follows [74, 77, 207–209]

$$E_c = \frac{\pi E L d^3}{12R}, \tag{5.41}$$

where E is the Young modulus of the graphene sheet, d is its thickness, and L is the length of the nanotube. The length of the nanotube can be expressed via the total number of atoms N as follows:

$$L = \frac{S_i}{2\pi R} = \frac{\rho_i (N - N_e - N_{cap})}{2\pi R}, \tag{5.42}$$

where S_i is the surface area of the tubular part of the nanotube, N_e is the number of atoms at the edge, and N_{cap} is the number of atoms in the cap (see Fig. 5.10). Substituting Eq. (5.42) into Eq. (5.41) one obtains

$$E_c = \frac{E d^3 \rho_i}{24R^2} N - \frac{E d^3 \rho_i}{24R^2} N_e - \frac{\pi E d^3 \rho_i}{12 \rho_{cap}}. \tag{5.43}$$

The first term in Eq. (5.43) corresponds to the curvature energy of the tubular part of the nanotube which is equal to the second term in the large parentheses in Eq. (5.15). Thus,

$$\frac{C}{R^2} = \frac{E d^3 \rho_i}{24R^2} = \frac{\sqrt{3}\pi^2 \epsilon_c}{n^2 + m^2 + nm} \tag{5.44}$$

Here C is the curvature constant,

$$C = \frac{3\sqrt{3}\langle a\rangle^2}{4}\epsilon_c = \rho_i \epsilon_c. \tag{5.45}$$

Substituting the curvature constant, Eq. (5.45), into Eq. (5.44) one obtains,

$$E = \frac{24\epsilon_c}{d^3}. \tag{5.46}$$

The curvature constant C has been a subject of many investigations [77, 207, 209–216]. With $\langle a\rangle = 1.41$Å and Eq. (5.45) one obtains $C_{\rm ters} = 1.5183$ eVÅ^2 for the Tersoff potential calculations and $C_{\rm bren} = 0.9168$ eVÅ^2 for the Brenner potential calculations. $C_{\rm ters}$ is very close to the value 1.57 eVÅ^2 extracted from the measured phonon spectrum of graphite [215] and is in agreement with 1.44 eVÅ^2, 1.34 eVÅ^2, and 1.53 eVÅ^2, which were calculated in Refs. [210, 212, 216] These values were calculated with the use of empirical potentials and using the tight-binding model. *Ab initio* density functional theory calculations lead to a somewhat higher value of the curvature constant. Thus the values 2.0 eVÅ^2, 2.9 eVÅ^2, and 2.14 eVÅ^2 were reported in Refs. [209, 211, 213].

The curvature constants reported earlier are in better agreement with the result obtained for the open-end nanotubes using the Tersoff potential than with the value $C_{\rm bren}$ calculated using Brenner potential. This fact shows that the Tersoff potential describes elastic properties of the nanotubes more accurately.

Young modulus is another important characteristic of the nanotubes. Researchers have reported widely varying Young's modulus values for carbon nanotubes in the range 0.32-5.5 TPa [85, 89, 207, 210, 211, 215, 217–219]. The large scatter of these values is apparently due to different measurement techniques, simulation methods, and dimensions (diameter, thickness and configuration). As seen from Eq. (5.46) the Young modulus depends on the

effective thickness of the graphene layer d. In Ref. [218] and Ref. [210] it has been suggested that the thickness of a graphene sheet is equal to 0.66 Å and 0.74 Å, respectively, being radius of a single carbon atom. In Refs. [77, 219], the thickness 3.4 Å was used, which is equal to the interplane distance in graphite. For our estimates we use $d = 1.5$Å which is approximately equal to the inter carbon distance in graphene. This value corresponds to the thickness of a fullerene shell [220] as reported by Rüdel *et al.* [221]. Thus we obtain $E_{\text{ters}} = 0.670$ TPa and $E_{\text{bren}} = 0.404$ TPa. Both values are within the ranges reported earlier indicating that the Tersoff and the Brenner potentials adequately describe the elastic properties of the nanotubes.

Despite the differences in results obtained using the Brenner and the Tersoff potentials, the liquid surface model is a universal tool. Differences between the potentials can always be accounted for by the parameters without changing the general framework of the model. Thus, it is feasible to derive the liquid surface model parameters from the comparison of its predictions with the results of *ab initio* calculations being based on LDA approximation or the Hartree-Fock theory.

5.7 Effect of catalytic nanoparticle on the binding energy

It is experimentally known that when capped nanotubes grow from a catalytic nanoparticle [37, 222, 223], they have no open edges. The noncapped edge of a nanotube is embedded in the catalytic particle, which changes the interaction energy of the atoms in the vicinity of the contact.

In order to understand how the interaction of a nanotube with the catalytic nanoparticle influence the stability of a nanotube we use the model developed in Ref. [190] for calculating the interaction of a deposited cluster with a substrate. The catalytic nanoparticle is typically composed of Ni, Co

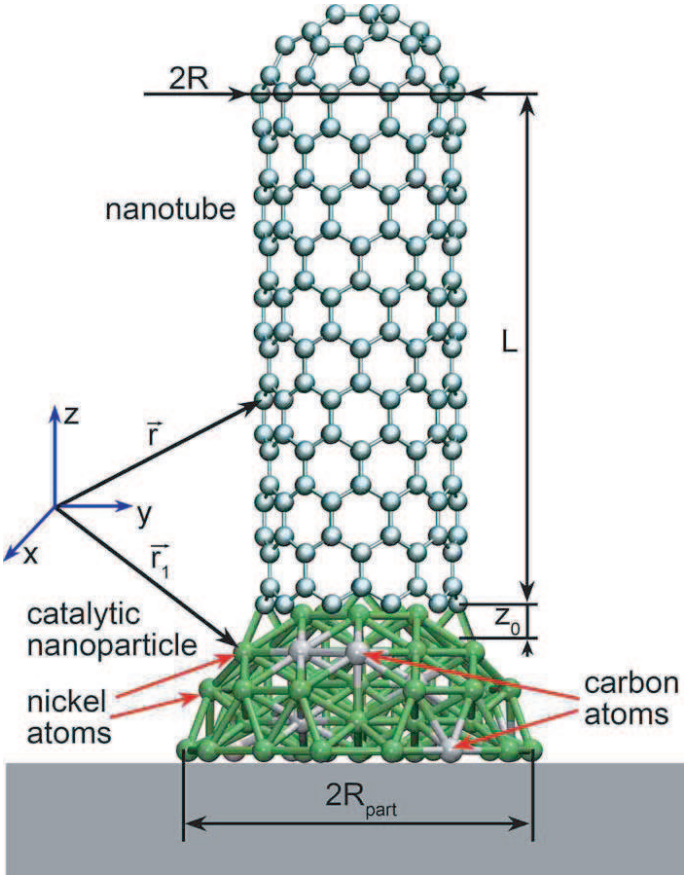

Figure 5.18: Single-wall carbon nanotube on top of a catalytic nickel nanoparticle, z_0 is the distance between the nanotube and the catalytic nanoparticle, L is the length of the nanotube, R is the nanotube radius, and R_{part} is the radius of the nanoparticle [16].

or Fe atoms and the carbon atoms from feedstock molecules diffuse inside from the catalytic region towards the growth region [37, 224, 225]. Thus in the following discussion we consider the catalytic nanoparticle being composed of a mixture of nickel and carbon atoms, as schematically illustrated in Fig.5.18. The atoms of the catalytic nanoparticle interact with the carbon atoms of the nanotube via the Morse potential,

$$U_k(r) = \varepsilon_k(\{1 - \exp[-\rho_k(r - r_{0_k})]\}^2 - 1). \tag{5.47}$$

Here r is the distance between an atom of the nanotube and an atom of the catalytic particle, ε_k, ρ_k, and r_{0_k} are parameters of the potential. Index k denotes either carbon-carbon (C) or carbon-nickel (Ni) interaction.

The Morse potential parameters ρ and r_0 are 2.625 Å^{-1} and 1.39 Å for the C-C interaction [93], while for the C-Ni interaction these parameters are 1.9213 Å^{-1} and 1.7518 Å, respectively [226]. The parameter ε is varied in different papers by more than an order of magnitude. For example in Ref. [226], it is 2.4781 eV for the C-Ni interaction, while in Ref. [227], it is 0.1 eV. The parameter ϵ for the C-C interaction is usually taken as 3.7-3.8 eV [93, 228].

With the use of formalism developed in Ref. [190] the interaction energy of a nanotube with the catalytic nanoparticle can be estimated as

$$\begin{aligned} E_{int} &= \frac{2\pi R n_{\mathrm{C}}}{S_0} \int_{V_n} \int_{z_0}^{L+z_0} U_{\mathrm{C}}(|\mathbf{r} - \mathbf{r_1}|) dV_1 dz \\ &+ \frac{2\pi R n_{\mathrm{Ni}}}{S_0} \int_{V_n} \int_{z_0}^{L+z_0} U_{\mathrm{Ni}}(|\mathbf{r} - \mathbf{r_1}|) dV_1 dz \end{aligned} \tag{5.48}$$

where $n_{\mathrm{C}} = N_{\mathrm{C}}/V_n$ and $n_{\mathrm{Ni}} = N_{\mathrm{Ni}}/V_n$ are the concentrations of carbon and nickel in the catalytic nanoparticle, V_n is the volume of the nanoparticle, S_0 is the cross-section area of a single carbon atom, and z_0 is the distance between the catalytic particle and the nanotube (see Fig. 5.18). $\mathbf{r} = \mathbf{i}x + \mathbf{j}y + \mathbf{k}z$ is the vector describing an atom in the nanotube ($\mathbf{i}, \mathbf{j}$ and $\mathbf{k}$ are the unit basis vectors), while $\mathbf{r_1}$ is the vector which describes an atom in the catalytic nanoparticle(see Fig. 5.18). Equation (5.48) can be written as follows:

$$E_{int} = -\varepsilon_{\mathrm{C}}.N_{\mathrm{C}}.\alpha_{\mathrm{C}}(z_0, R_{part}, R) - \varepsilon_{\mathrm{Ni}}.N_{\mathrm{Ni}}.\alpha_{\mathrm{Ni}}(z_0, R_{part}, R) \tag{5.49}$$

where $\alpha_{\rm C}$, $\alpha_{\rm Ni}$ are dimensionless functions defining interactions determined by the size and topology of the catalytic nanoparticle defined by the integrals in Eq. (5.48) as follows:

$$\alpha_k = \frac{2\pi R}{V_n S_0} \int_{V_n} \int_{z_0}^{L+z_0} [(1 - e^{-\rho_k(|\mathbf{r}-\mathbf{r_1}|-r_{0_k})})^2 - 1] dV_1 dz. \tag{5.50}$$

Let us consider the binding energy per atom for a nanotube of chirality $(28, 0)$ accounting for the interaction with catalytic nanoparticle. According to Eq. (5.10) the radius of this nanotube is equal to $R_{28\times0} = 10.88\mathring{A}$. We assume the catalytic nanoparticle to be a sphere of radius $R_{part} = 2R_{28\times0}$ (see Fig. 5.18), thus the total number of atoms in the catalytic nanoparticle can be estimated as $N_{total} \approx V_n/V_{\rm Ni}$, where $V_{\rm Ni} = 4/3\pi R_{\rm Ni}^3$ is the effective volume of a single nickel atom. With $R_{\rm Ni} \approx 1.245\mathring{A}$ one obtains $N_{\rm total} \approx 5340$.

Let us assume the fraction of carbon atoms in the catalytic nanoparticle to be 0.1, resulting in $N_{\rm C} = 534$ and $N_{\rm Ni} = 4806$. The distance between the nanotube and the nanoparticle, $z_0 \approx 0.9$Å, being the distance at which the interaction energy of a single carbon atom with an infinite crystal of nickel atoms has a minimum. Substituting the numbers into Eq. (5.50) and calculating S_0 from Eq. (5.13) one obtains $\alpha_{\rm C} = 0.0033$ and $\alpha_{\rm Ni} = 0.0122$. Substituting $\alpha_{\rm C}, \alpha_{\rm Ni}, N_{\rm C}$ and $N_{\rm Ni}$ into Eq. (5.49) $[S_0 = \rho_i]$ one obtains the correction to the total energy of a nanotube as a function of potential well depth for C-C and C-Ni interactions $\varepsilon_{\rm C}$ and $\varepsilon_{\rm Ni}$. Since the parameters $\varepsilon_{\rm C}$ and $\varepsilon_{\rm Ni}$ vary in different papers significantly we assume $\varepsilon_{\rm C} = \varepsilon_{\rm Ni} = \varepsilon$. We have varied ε in order to illustrate the influence of the catalytic nanoparticle on the nanotube stability.

In Fig. 5.19, we show the binding energy per atom calculated using the Brenner potential for the capped nanotube of chirality (28,0). Different lines show the binding energy per atom calculated using the liquid surface model with accounting for the interaction with the catalytic nanoparticle and

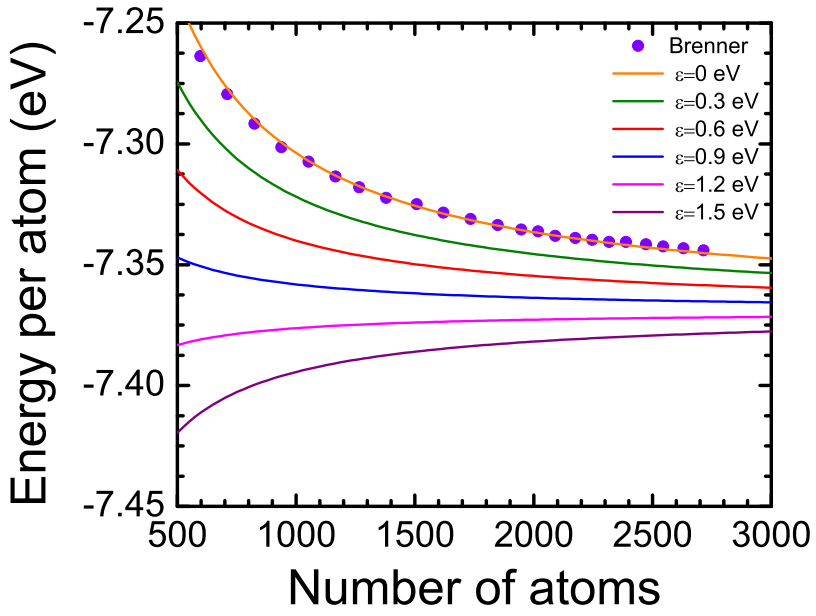

Figure 5.19: Binding energy per atom calculated using the Brenner potential (dots) for a capped nanotube of chirality (28,0). Different lines show the binding energy per atom calculated using the liquid surface model with accounting for the interaction with the catalytic nanoparticle and correspond to the different values of the parameter ε which describes the interatomic interaction. The corresponding values of ε are indicated in the inset [16].

correspond to the different values of parameter ε. the corresponding values of ε are given in the inset. From Fig. 5.19 it is clear that the catalytic nanoparticle changes the energetics of the nanotube dramatically. If the interaction of a nanotube with the catalytic nanoparticle is weak (i.e., the well depth of the interatomic potential is $\lesssim 1$ eV) than longer nanotubes are energetically more favourable, because the binding energy per atom decreases and the following condition is fulfilled:

$$E_{N+1} - E_N - E_1 < 0. \tag{5.51}$$

Here E_{N+1} and E_N are the energies of nanotubes with $N+1$ and N atoms, respectively, while $E_1 = 0$ is the energy of a single atom. If the condition Eq. (5.51) holds then attachment of additional atoms to the nanotube is energetically favourable resulting in its growth. Figure shows that if the catalytic nanoparticle-nanotube interaction is strong (see curves calculated with $\varepsilon = 1.2$ eV and $\varepsilon = 1.5$ eV in Fig. 5.19) than the trend of the binding energy per atoms changes and it becomes energetically more favourable for the nanotube to collapse.

5.8 Summary

In this chapter, we have developed a simple, classical model which is capable of predicting the binding energies of single-walled carbon nanotubes, once the chirality and the total number of atoms are known. Even with empirical potentials, like Tersoff potential, there are limitations on the size of nanotubes whose energy can be calculated. Hence, the developed liquid surface model serves as a potential candidate for the binding energy calculation of very large nanotubes. The major achievements of this chapter are presented below.

- Liquid surface model is used for the study of the binding energy of carbon nanotubes and it was shown that this model can predict the binding energy per atom for nanotubes with a reasonable accuracy compared to that calculated with Brenner and Tersoff potentials. The relative error is found to be below 0.3%, corresponding to the absolute energy difference being less than 0.01 eV.

- Our studies show that the presence of a catalytic nanoparticle can change the binding energy per atom dramatically and it is demonstrated that if the interaction of a nanotube with the catalytic nanoparticle is weak (i.e., $\lesssim 1$ eV) then attachment of an additional atom to a nanotube is an energetically favourable process. Further, it is shown

that if this interaction is strong (i.e., $\gtrsim 1$ eV), it becomes energetically more favourable for the nanotube to collapse.

- With the use of the paremeters of liquid surface model, the Young modulus and the curvature constant for single-walled carbon nanotubes are calculated. The obtained values are in agreement with the values reported earlier, which affirms the validity of our model for the study of the energetics of carbon nanotubes.

6

Conclusions and Prospects

6.1 Present conclusions

The thesis has achieved its main objective, namely, developing a simple and computationally inexpensive model which could explain the energetics of carbon nanotubes irrespective of their sizes and chiralities. After giving a detailed description of various methods used for the theoretical study of carbon nanotubes, the limitations of such methods are elaborated. The importance of developing alternate methods which takes into account all necessary features of the system but at the same time remains simple and computationally inexpensive are emphasised and a model named liquid surface model is developed. The model serves as an efficient tool to calculate the binding energies of very large nanotubes provided their chirality and total number of atoms are known.

The liquid surface model was suggested for open-end and capped nanotubes. It was shown that the energy of capped nanotubes is determined by five physical parameters, while for the open-end nanotubes three parameters are sufficient. The parameters of the liquid surface model were determined from the calculations performed with the use of empirical Tersoff and Brenner potentials and the accuracy of the model was analysed. It was shown that the liquid surface model can predict the binding energy per atom for capped nanotubes with relative error below 0.3% compared to Brenner potential calculations, corresponding to the absolute energy difference being less than 0.01 eV.

The influence of the catalytic nanoparticle, atop which a nanotube grows, on the nanotube energetics was also discussed. It was demonstrated that the catalytic nanoparticle changes the binding energy per atom dramatically. In particular, it was shown that if the interaction of a nanotube with the catalytic nanoparticle is weak (i.e., $\lesssim 1$ eV) then attachment of an additional atom to a nanotube is an energetically favourable process, while if the catalytic nanoparticle nanotube interaction is strong (i.e., $\gtrsim 1$ eV), it becomes energetically more favourable for the nanotube to collapse. The suggested model gives an important insight in the energetics and stability of nanotubes of different chiralities and is an important step towards the understanding of the growth mechanism of nanotubes.

We have also analysed elastic properties of nanotubes and have performed a comparison with available experimental measurements and earlier theoretical predictions. Namely, we have calculated the Young modulus and the curvature constant for single-walled carbon nanotubes from the paremeters of the liquid surface model and demonstrated that the obtained values are in agreement with the values reported earlier. The calculated Young modulus and the curvature constant were used to conclude about the accuracy of the Tersoff and Brenner potentials. The elastic properties were derived from the parameters of the liquid surface model obtained from the Tersoff and Brenner potential calculations and therefore correspond to the values calculated within the framework of the Tersoff and the Brenner potentials, respectively. It was shown that the obtained values of the Young modulus and the curvature constant are within the ranges of values reported earlier for both potentials indicating that the Tersoff and the Brenner potentials adequately describe the elastic properties of nanotubes.

6.2 Future prospects

Although, in this thesis liquid surface model is developed for the simplest case of nondeformed single-wall nanotubes, it can be applied to a variety of systems especially to deformed nanotubes and multiwalled nanotubes. Deformed nanotubes, such as toroidal or helical, are getting wider attention nowadays because of the observation that one can change the electrical properties of nanotubes by deforming them. Study of the energetics and mechanical properties of such systems using liquid surface model requires inclusion of additional energy terms which take into account the extra energies of these structures. For example, the study of multiwalled nanotubes using liquid surface model needs the addition of an extra volume energy term corresponding to the interaction between different walls of the multiwalled nanotube.

Another important property which can be studied using liquid surface model is the energetics of interacting nanotubes, such as, for example, nanotubes in a crystalline array. When nanotubes are grown using different experimental techniques, they are normally grown in bundles or forests. Individual nanotubes are separated from this bundle of nanotubes using different purification methods. It is obvious that the interaction of nanotubes in an array plays a major role in the growth of the total system. This can be investigated using liquid surface model.

Using liquid surface model, we have studied the elastic properties (curvature constant and Young modulus) of single-walled nanotubes in this thesis. This study can be extended to many more systems like multiwalled nanotubes, nanoropes and nanotube bundles which are already recognised as potential candidates for high strength materials. A better understanding of the elastic properties of such systems would help to produce more lighter and stronger materials, a feature which the industry is always looking for.

Growth mechanism of carbon nanotubes is still a widely discussed issue in the research circle and there are many contradictory claims. In fact, one of the major issues the nanotube experimentalists are facing currently is the production of nanotubes with desired chirality. Although a lot of progress is achieved in this direction, this issue remains unsolved. Liquid surface model could provide some insights on this topic by analysing the behaviour of the binding energy of nanotubes of different chiralities. Our studies showed that the interaction of the nanoparticles on top of which the nanotubes grow has a great influence on the energetics and hence on the growth mechanism of the nanotubes. The study can be extended by using better potentials for this interaction. Further, in order to get a proper understanding of the growth mechanism of carbon nanotubes, one needs to consider the interaction of the nanotube and the catalytic particle with the substrate, which is left open for future considerations and analysis.

Acknowledgements

First of all, I would like to thank my advisor and supervisor Prof. Andrey V. Solov'yov for guiding me through this work, providing me with advice and help throughout my Ph.D. He did it with enthusiasm and patience that made my work much more exciting and rewarding.

Secondly, thanks to Dr. Ilia A. Solov'yov, without whom this thesis would not have been possible. He closely worked with me throughout the better part of my Ph.D., provided me with insights, and helped me to make my work more concrete.

Special thanks to Dr. Emanuele Scifoni for those fruitful discussions which paved the way to this thesis in its current shape. I Gratefully remember Ms. Sophie Nahrwold and Ms. Lisha Naduvilezhathu for their invaluable helps in preparing the Zusammenfassung.

There are many friends and colleagues who, through their support and fruitful discussions, made this work more pleasant to go through. Of them, I thankfully remember Dr. Oleg Obolensky, Dr. Andrey Lyalin, Dr. Elsa Henriques Ms.Adilah Hussien, Ms. Stephanie Lo and all the members of MBN group at FIAS.

Special thanks to my office mates Ms. Hasnaa Fatehi, Mr. Jenja Jitsev and Ms. Cristina Savin for all the invaluable helps. I thankfully acknowledge the helps and support I got from Pro. Jochen Triesch, Prof. Christoph von der Malsburg, Prof. Michael Huth, Prof. Harald Jeschke and Prof. Dirk H. Rischke during my PhD period.

Many thanks to my beloved teachers Dr. Devadhasan, Ms. Sandhya and to my friends Mr. Dileep and Ms. Leema for their incessant encouragement which always helped me to get along with the difficult situations.

Most importantly, none of this would have been possible without the love and patience of my family. My parents Mathew and Mary were always there to listen and encourage me along with my brother Majesh and sister Manjusha. My family has been a constant source of love, concern, support and strength all these years. I would like to express my heart-felt gratitude to my family.

Finally, thanks to all my dear friends who helped me in many ways during these three years of my stay in Frankfurt and made my days beautiful and exciting.

Bibliography

[1] Iijima, S. 1991. Helical microtubules of graphitic carbon. *Nature.* 354:56–58.

[2] Frieden, E. 1972. The chemical elements of life. *Scientific American.* 63:52–60.

[3] Kroto, H. W., J. R. Heath, S. C. O'Brien, R. F. Curl, and R. E. Smalley. 1985. C_{60}: Buckminsterfullerene. *Nature.* 318:162–163.

[4] Nasibulin, A. G., A. S. Anisimov, P. V. Pikhitsa, H. Jiang, D. P. Brown, M. Choi, and E. I. Kauppinen. 2007. Investigations of nanobud formation. *Chem. Phys. Lett.* 446:109–114.

[5] Vieira, R., M. J. Ledoux, and C. Pham-Huu. 2004. Synthesis and characterisation of carbon nanofibres with macroscopic shaping formed by catalytic decomposition of C_2H_6/H_2 over nickel catalyst. *Appl. Cata. A.* 274:1–8.

[6] Dubrovinskaia, N., L. Dubrovinsky, W. Crichton, F. Langenhorst, and A. Richter. 2005. Aggregated diamond nanorods, the densest and least compressible form of carbon. *Appl. Phys. Lett.* 87:083106–(1–3).

[7] Frondel, C. and U. B. Marvin. 1967. Lonsdaleite, a hexagonal polymorph of diamond. *Nature.* 214:587–589.

[8] Harris, P. J. F. 2004. Fullerene-related structure of commercial glassy carbons. *Philo. Mag.* 84:3159 – 3167.

[9] Rode, A. V., S. T. Hyde, E. G. Gamaly, R. G. Elliman, D. R. McKenzie, and S. Bulcock. 1999. Structural analysis of a carbon foam formed by high pulse-rate laser ablation. *Appl. Phys. A.* 69:S755–S758.

[10] Ströck, M. 2006. *http://commons.wikimedia.org/wiki/.*

[11] Oberlin, A., M. Endo, and T. Koyama. 1976. Filamentous growth of carbon through benzene decomposition. *J. Cry. Grow.* 32:335–349.

[12] Chernozatonskii, L. A. 1992. Barrelenes/tubelenes - a new class of cage carbon molecules and its solids. *Phys. Lett. A.* 166:55–60.

[13] Monthioux, M. and V. L. Kuznetsov. 2006. Who should be given the credit for the discovery of carbon nanotubes. *Carbon.* 44:1621–1623.

[14] Nanotube and Nanodevice Laboratory, School of Electrical Engineering and Department of Micro/Nano Systems, Korea University. 2005. *http://nanotube.korea.ac.kr.*

[15] White, C. T. and J. W. Mintmire. 2005. Fundamental properties of single-wall carbon nanotubes. *J. Phys. Chem. B.* 109:52–65.

[16] Solov'yov, I. A., M. Mathew, A. V. Solov'yov, and W. Greiner. 2008. Liquid surface model for carbon nanotube energetics. *Phys. Rev. E.* 78:051601 (1–13).

[17] Dresselhaus, M. S., G. Dresselhaus, and R. Saito. 1995. Physics of carbon nanotubes. *Carbon.* 33:883–891.

[18] Saito, R., G. Dresselhaus, and M. S. Dresselhaus. 1999. *Physical properties of carbon nanotubes.* Imperial College Press.

[19] UDaily. 2004. *http://www.udel.edu/PR/UDaily/2004/nanotubes092603.html.* University of Delaware, USA.

[20] Baughman, R. H., A. A. Zakhidov, and W. A. de Heer. 2002. Carbon nanotubes - the route toward applications. *Science.* 297:787–792.

[21] Murakami, Y., Y. Miyauchi, S. Chiashi, and S. Maruyama. 2003. Characterization of single-walled carbon nanotubes catalytically synthesized from alcohol. *Chem. Phys. Lett.* 374:53–58.

[22] Noda, S., K. Hasegawa, H. Sugime, K. Kakehi, Z. Zhang, S. Maruyama, and Y. Yamaguchi. 2007. Millimeter-thick-single-walled carbon nanotube forests: Hidden roles of catalyst support. *Jpn. J. Appl. Phys.* 46:L399–401.

[23] Zhang, G., D. Mann, L. Zhang, A. Javey, Y. Li, E. Yenilmez, Q. Wang, J. P. McVittie, Y. Nishi, J. Gibbons, and H. Dai. 2005. Ultra-high-

yield growth of vertical single-walled carbon nanotubes: Hidden roles of hydrogen and oxygen. *Proc. Nat. Acad. Sci.* 102:16141–16145.

[24] Zhong, G. F., T. Iwasaki, K. Honda, Y. Furukawa, I. Ohdomari, and H. Kawarada. 2005. Very high yield growth of vertically aligned single-walled carbon nanotubes by point-arc microwave plasma cvd. *Chem. Vap. Dep.* 11:127–130.

[25] Eres, G., A. A. Kinkhabwala, H. Cui, D. B. Geohegan, A. A. Puretzky, and D. H. Lowndes. 2005. Molecular beam-controlled nucleation and growth of vertically aligned single-wall carbon nanotube arrays. *J. Phys. Chem. B.* 109:16684–16694.

[26] Xu, Y. Q., E. Flor, M. J. Kim, B. Hamadani, H. Schmidt, R. E. Smalley, and R. H. Hauge. 2006. Vertical array growth of small diameter single-walled carbon nanotubes. *J. Am. Chem. Soc.* 128:6560–6561.

[27] Zhao, H. P., Y. D. He, X. H. Kong, and W. Gao. 2007. Carbon nanotubes and diamond-like carbon films produced by cathodic micro-arc discharge in aqueous solutions. *Mat. Lett.* 61:4916–4919.

[28] Iijima, S. and T. Ichihashi. 1993. Single-shell carbon nanotubes of 1-nm diameter. *Nature.* 363:603–605.

[29] Bethune, D. S., C. H. Kiang, M. S. de Vries, G. Gorman, R. Savoy, J. Vazquez, and R. Beyers. 1993. Cobalt-catalysed growth of carbon nanotubes with single-atomic-layer walls. *Nature.* 363:605–607.

[30] Radhakrishnan, G., P. M. Adams, and L. S. Bernstein. 2007. Plasma characterization and room temperature growth of carbon nanotubes and nano-onions by excimer laser ablation. *Appl. Surf. Sci.* 253:7651–7655.

[31] Thess, A., R. Lee, P. Nikolaev, H. Dai, P. Petit, J. Robert, C. Xu, Y. H. Lee, S. G. Kim, A. G. Rinzler, D. T. Colbert, G. E. Scuseria, D. Tománek, J. E. Fischer, and R. E. Smalley. 1996. Crystalline ropes of metallic carbon nanotubes. *Science.* 273:483–487.

[32] Zhang, Y. and S. Iijima. 1999. Formation of single-wall carbon nanotubes by laser ablation of fullerenes at low temperature. *Appl. Phys. Lett.* 75:3087–3089.

[33] Zhang, H., Y. Ding, C. Wu, Y. Chen, Y. Zhu, Y. He, and S. Zhong. 2003. The effect of laser power on the formation of carbon nanotubes prepared in CO_2 continuous wave laser ablation at room temperature. *Physica B.* 325:224–229.

[34] Tamir, S. and Y. Drezner. 2006. New aspects on pulsed laser deposition of aligned carbon nanotubes. *Appl. Surf. Sci.* 252:4819–4823.

[35] Sugai, T., H. Yoshida, T. Shimada, T. Okazaki, H. Shinohara, and S. Bandow. 2003. New synthesis of high-quality double-walled carbon nanotubes by high-temperature pulsed arc discharge. *Nano Lett.* 3:769–773.

[36] Hofmann, S., R. Sharma, C. Ducati, G. Du, C. Mattevi, C. Cepek, M. Cantoro, S. Pisana, A. Parvez, F. Cervantes-Sodi, A. C. Ferrari, R. Dunin-Borkowski, S. Lizzit, L. Petaccia, A. Goldoni, and J. Robertson. 2007. In situ observations of catalyst dynamics during surface-bound carbon nanotube nucleation. *Nano Lett.* 7:602–608.

[37] Geng, J., C. Singh, D. S. Shephard, M. S. P. Shaffer, B. F. G. Johnson, and A. H. Windle. 2002. Synthesis of high purity single-walled carbon nanotubes in high yield. *Chem. Commun.* 10:2666–2667.

[38] Kong, J., H. T. Soh, A. M. Cassell, C. F. Quate, and H. Dai. 1998. Synthesis of individual single-walled carbon nanotubes on patterned silicon wafers. *Nature.* 395:878–881.

[39] Tans, S. J., M. H. Devoret, H. Dai, A. Thess, R. E. Smalley, L. J. Geerlings, and C. Dekker. 1997. Individual single-wall carbon nanotubes as quantum wires. *Nature.* 386:474–477.

[40] Bladh, K., L. K. L. Falk, and F. Rohmund. 2000. On the iron-catalysed growth of single-walled carbon nanotubes and encapsulated metal particles in the gas phase. *Appl. Phys. A.* 70:317–322.

[41] Li, Y.-L., I. A. Kinloch, M. S. P. Shaffer, J. Geng, B. Johnson, and A. H. Windle. 2004. Synthesis of single-walled carbon nanotubes by fluidized-bed method. *Chem. Phys. Lett.* 384:98–102.

[42] Dai, H., A. G. Rinzler, P. Nikolaev, A. Thess, D. T. Colbert, and R. E. Smalley. 1996. Single-wall nanotubes produced by metal catalyzed disproportionation of carbon monoxide. *Chem. Phys. Lett.* 260:471–475.

[43] Saito, Y. 1995. Nanoparticles and filled nanocapsules. *Carbon.* 33:979–988.

[44] *http://www.nanoelectronics.engr.scu.edu/nanotechnology.*

[45] Yakobson, B. and R. Smalley. 1997. Fullerene nanotubes: $C_{1,000,000}$ and beyond. *American Scientist.* 85:324–337.

[46] Ren, Z. F., Z. P. Huang, J. W. Xu, J. H. Wang, P. Bush, M. P. Siegal, and P. N. Provencio. 1998. Synthesis of large arrays of well-aligned carbon nanotubes on glass. *Science.* 282:1105–1107.

[47] Nasibulin, A. G., A. Moisala, D. P. Brown, H. Jiang, and E. I. Kauppinen. 2005. A novel aerosol method for single walled carbon nanotube synthesis. *Chem. Phys. Lett.* 402:227–232.

[48] Ding, F., K. Bolten, and A. Rosén. 2004. Nucleation and growth of single-walled carbon nanotubes: A molecular dynamics study. *J. Phys. Chem. B.* 108:17369–17377.

[49] Predebon, J. C., F. M. Florio, and R. T. Basting. 2006. Use of CV-DentUS diamond tips for ultrasound in cavity preparation. *The Jour. Cont. Dent. Pract.* 7:50–59.

[50] Meyyappan, M., L. Delzeit, A. Cassell, and D. Hash. 2003. Carbon nanotube growth by PECVD: a revies. *Pla. Sourc. Sci. Tech.* 12:205–216.

[51] Li, J., R. Stevens, L. Delzeit, H. T. Ng, A. Cassell, J. Han, and M. Meyyappan. 2002. Electronic properties of multiwalled carbon nanotubes in an embedded vertical array. *Appl. Phys. Lett.* 81:910–912.

[52] Nerushev, O. A., M. Sveningsson, L. K. L. Falk, and F. Rohmund. 2001. Carbon nanotube films obtained by thermal chemical varpour deposition. *J. Mater. Chem.* 11:1122–1132.

[53] Bachtold, A., P. Hadley, T. Nakanishi, and C. Dekker. 2001. Logic circuits with carbon nanotube transistors. *Science.* 294:1317–1320.

[54] Baughman, R. H., C. X. Cui, A. A. Zakhidov, Z. Iqbal, J. N. Barisci, G. M. Spinks, G. G. Wallace, A. Mazzoldi, D. D. Rossi, A. G. Rinzler, O. Jaschinski, S. Roth, and M. Kertesz. 1999. Carbon nanotube actuators. *Science.* 284:1340–1344.

[55] Biercuk, M. J., M. C. Llaguno, M. Radosavljevic, J. K. Hyun, A. T. Johnson, and J. E. Fischer. 2002. Carbon nanotue composites for thermal management. *Appl. Phys. Lett.* 80:2767–2769.

[56] Choi, W. B., D. S. Chung, J. H. Kang, H. Y. Kim, Y. W. Jin, I. T. Han, Y. H. Lee, J. E. Jung, N. S. Lee, G. S. Park, and J. M. Kim. 1999. Fully sealed, high-brightness carbon-nanotube field emission display. *Appl. Phys. Lett.* 75:3129–3131.

[57] Fuhrer, M. S., J. Nygard, L. shih, M. Forero, Y. G. Yoon, M. S. C. Mazzoni, H. J. Choi, J. Ihm, S. G. Louie, A. Zettl, and P. L. McEuen. 2000. Crossed nanotube junctions. *Science.* 288:494–497.

[58] Hafner, J. H., C. L. Cheung, and C. M. Lieber. 1999. Growth of nanotube for probe microscopy tips. *Nature.* 398:761–762.

[59] Hirscher, M., M. Becher, M. Haluska, A. Quintel, V. Skakalova, Y. M. Choi, U. Dettlaff-Weglikowska, S. Roth, I. Stepanek, P. Bernier, A. Leonhardt, and J. Fink. 2002. Hydrogen storage in carbon nanostructures. *J. Alloys and Compd.* 330:654–658.

[60] Milne, W. I., K. B. K. Teo, G. A. J. Amaratunga, P. Legagneux, L. Gangloff, J. P. Schnell, V. Semet, V. T. Binh, and O. Groening. 2004. Carbon nanotubes as field emission sources. *J. Mat. Chem.* 14:933–943.

[61] Rueckes, T., K. Kim, E. Joselevich, G. Y. Tseng, C. L. Cheung, and C. M. Lieber. 2000. Carbon nanotube-based nonvolatile random access memory for molecular computing. *Science.* 289:94–97.

[62] Tibbetts, G. G., G. P. Meisner, and C. H. Olk. 2001. Hydrogen storage capacity of carbon nanotube, filaments, and vapor-grown fibers. *Carbon.* 39:2291–2301.

[63] Wong, E. W., P. E. Sheehan, and C. M. Lieber. 1997. Nanobeam mechanics: Elasticity, strength and toughness of nanorods and nanotubes. *Science.* 277:1971–1975.

[64] Zandonella, C. 2001. Is it all just a pipe dream? *Nature.* 410:734–735.

[65] Chen, L., C. Cheung, P. D. Ashby, and C. M. Lieber. 2004. Single-walled carbon nanotube AFM probes: Optimal imaging resolution of nanoclusters and biomolecules in ambient and fluid environments. *Nano Lett.* 4:1725–1731.

[66] Collins, P. G., M. S. Arnold, and P. Avouris. 2001. Engineering carbon nanotube and nanotube circuits using electrical breakdown. *Science.* 292:706–709.

[67] Dalton, A. B., S. Collins, E. Muñoz, J. M. Razal, V. H. Ebron, J. P. Ferraris, J. N. Coleman, B. G. Kim, and R. H. Baughman. 2003. Super-tough carbon-nanotube fibres. *Nature.* 423:703–703.

[68] Cadek, M., J. N. Coleman, V. Barron, K. Hedicke, and W. J. Blau. 2002. Morphological and mechanical properties of carbon-nanotube-reinforced semicrystalline and amorphous polymer composites. *Appl. Phy. Lett.* 81:5123–5125.

[69] Barber, A. H., S. R. Cohen, and H. D. Wagner. 2003. Measurement of carbon nanotube-polymer interfacial strength. *Appl. Phy. Lett.* 82:4140–4142.

[70] Ni, B., S. B. Sinnott, P. T. Mikulski, and J. A. Harrison. 2002. Compression of carbon nanotubes filled with C_{60}, CH_4 or Ne: Predictions from molecular dynamics simulations. *Phy. Rev. Lett.* 88:205505–(1–4).

[71] Tsiolkovski, K. E. 1895. *Speculations of earth and sky, and On Vesta.* Izd-vo AN SSR.

[72] Pearson, J. 1975. The orbital tower: a spacecraft launcher using the Earth's rotational energy. *Acta Astronautica.* 2:785–799.

[73] Laidler, K. J. 1993. *The world of physical chemistry.* Oxford University Press.

[74] Landau, L. D., A. M. Kosevich, and E. M. Lifshitz. 1986. *Theory of elasticity.* Butterworth, Heinemann.

[75] Yakobson, B. I., C. J. Brabec, and J. Bernholc. 1996. Nanomechanics of carbon tubes: Instabilities beyond linear response. *Phy. Rev. Lett.* 76:2511–2514.

[76] Tibbetts, G. G. 1983. Carbon fibers produced by pyrolysis of natural gas in stainless steel tubes. *Appl. Phys. Lett.* 42:666–668.

[77] Robertson, D. H., D. W. Brenner, and J. W. Mintmire. 1992. Energetics of nanoscale graphitic tubules. *Phys. Rev. B.* 45:12592–12595.

[78] Ruoff, R. S. and D. C. Lorents. 1995. Mechanical and thermal properties of carbon nanotubes. *Carbon.* 33:925–930.

[79] Treacy, M. M. J., T. W. Ebbensen, and J. M. Gibson. 1996. Exceptionally high Young's modulus observed for individual carbon nanotubes. *Nature.* 381:678–680.

[80] Lu, J. P. 1997. Elastic properties of carbon nanotubes and nanoropes. *Phys. Rev. Lett.* 79:1297–1300.

[81] Cai, J., R. F. Bie, X. M. Tan, and C. Lu. 2004. Application of the tight-binding method to the elastic modulus of C60 and carbon nanotube. *Physica B.* 344:99–102.

[82] Poncharal, P., Z. L. Wang, D. Ugarte, and W. A. de Heer. 1999. Electrostatic deflections and electromechanical resonances of carbon nanotubes. *Science.* 283:1513–1516.

[83] Krishnan, A., E. Dujardin, T. W. Ebbesen, P. N. Yianilos, and M. M. J. Treacy. 1998. Young's modulus of single-walled nanotubes. *Phys. Rev. B.* 58:14013–14019.

[84] Salvetat, J. P., A. J. Kulik, J. M. Bonard, G. A. D. Briggs, T. Stockli, K. Motonier, S. Bonnamy, and F. Boguin. 1999. Elastic modulus of ordered and disordered multiwalled carbon nanotubes. *Adv. Mater.* 11:161–165.

[85] Hernández, E., C. Goze, P. Bernier, and A. Rubio. 1998. Elastic properties of C and $B_xC_yN_z$ composite nanotubes. *Phy. Rev. Lett.* 80:4502–4505.

[86] Sammalkorpi, M., A. V. Krasheninnikov, A. Kuronen, K. Nordlund, and K. Kaski. 2004. Mechanical properties of carbon nanotubes with vacancies and related defects. *Phys. Rev. B.* 70:245416–(1–8).

[87] Yu, M. F., O. Lourie, M. J. Dyer, K. Moloni, T. F. Kelly, and R. S. Ruoff. 2000. Strength and breaking mechanism of multiwalled carbon nanotubes under tensile load. *Science.* 287:637–640.

[88] Li, F., H. M. Cheng, S. Bai, G. Su, and M. S. Dresselhaus. 2000. Tensile strength of single-walled carbon nanotubes directly measured from their macroscopic ropes. *Appl. Phy. Lett.* 77:3161–3163.

[89] Yu, M. F., B. S. Files, S. Arepalli, and R. S. Ruoff. 2000. Tensile loading of ropes of single wall carbon nanotubes and their mechanical properties. *Phy. Rev. Lett.* 84:5552–5555.

[90] Walters, D. A., L. M. Ericson, M. J. Casavant, J. Liu, D. T. Colbert, K. A. Smith, and R. E. Smalley. 1999. Elastic strain of freely suspended single-wall carbon nanotube ropes. *Appl. Phy. Lett.* 74:3803–3805.

[91] NASA. *http://science.nasa.gov/headlines/y2002/16sep_rightstuff.htm.*

[92] Wei, C., K. Cho, and D. Srivastava. 2003. Tensile yielding of multiwall carbon nanotubes. *Appl. Phy. Lett.* 82:2512–2515.

[93] Belytschko, T., S. P. Xiao, G. C. Shchatz, and R. S. Ruoff. 2002. Atomistic simulations of nanotube fracture. *Phys. Rev. B.* 65:235430–(1–8).

[94] Yakobson, B. I., M. P. Campbell, C. J. Brabec, and J. Bernholc. 1997. High strain rate fracture and C-chain unraveling in carbon nanotubes. *Comp. Mat. Science.* 8:341–348.

[95] Wei, C., K. Cho, and D. Srivastava. 2003. Tensile strength of carbon nanotubes under realistic temperature and strain rate. *Phys. Rev. B.* 67:115407–(1–6).

[96] *http://nanopedia.case.edu/NWPage.php?page=nanotube.strength.*

[97] Cornwell, C. F. and L. T. Wille. 1997. Elastic properties of single-walled carbon nanotubes in compression. *Solid State Comm.* 101:555–558.

[98] Liang-Chen, C., W. Li-Jun, T. Dong-Sheng, X. Si-Shen, and J. Chang-Qing. 2001. X-ray diffraction study of carbon nanotubes under high pressure. *Chin. Phys. Lett.* 18:577–578.

[99] Karmakar, S., S. M. Sharma, P. V. Teredesai, and A. K. Sood. 2004. Pressure-induced phase transitions in iron-filled carbon nanotubes: X-ray diffraction studies. *Phys. Rev. B.* 69:165414–(1–5).

[100] Peters, M. J., L. E. McNeil, J. P. Lu, and D. Kahn. 2000. Structural phase transitions in carbon nanotube bundles under pressure. *Phys. Rev. B.* 61:5939–5944.

[101] Mylvaganam, K. and L. C. Zhang. 2007. Ballistic resistance capacity of carbon nanotubes. *Nanotechnology.* 18:475701–(1–4).

[102] Tang, J., L. C. Qin, T. Sasaki, M. Yudasaka, A. Matsushita, and S. Iijima. 2000. Compressibility and polygonization of single-walled carbon nanotubes under hydrostatic pressure. *Phy. Rev. Lett.* 85:1887–1889.

[103] Sharma, S. M., S. Karmakar, S. K. Sikka, P. V. Teredesai, A. K. Sood, A. Govindaraj, and C. N. R. Rao. 2001. Pressure-induced phase transformation and structural resilience of single-wall carbon nanotube bundles. *Phys. Rev. B.* 63:205417–(1–5).

[104] Girifalco, L. A., M. Hodak, and R. S. Lee. 2000. Carbon nanotubes, buckyballs, ropes and a universal graphitic potential. *Phys. Rev. B.* 62:13104–13110.

[105] Venkateswaran, U. D., A. M. Rao, E. Richter, M. Menon, A. Rinzler, R. E. Smalley, and P. C. Eklund. 1999. Probing the single-wall carbon nanotube bundle: Raman scattering under high pressure. *Phys. Rev. B.* 59:10928–10934.

[106] Kahn, D. and J. P. Lu. 1999. Vibrational modes of carbon nanotubes and nanoropes. *Phys. Rev. B.* 60:6535–6540.

[107] Yildirim, T., O. Gülseren, Ç. Kiliç, and S. Ciraci. 2000. Pressure-induced interlinking of carbon nanotubes. *Phys. Rev. B.* 62:12648–12651.

[108] Okada, S., A. Oshiyama, and S. Saito. 2001. Pressure and orientation effects on the electronic structure of carbon nanotube bundles. *J. Phys. Soc. Jpn.* 70:2345–2352.

[109] Sluiter, M. H. F., V. Kumar, and Y. Kawazoe. 2002. Symmetry-driven phase transformations in single-wall caron-nanotube bundles under hydrostatic pressure. *Phys. Rev. B.* 65:161402–(1–4).

[110] Reich, S., C. Thomsen, and P. Ordejón. 2003. Elastic properties and pressure induced phase transitions of single-walled carbon nanotubes. *Phys. Stat. Sol.(b).* 235:354–359.

[111] Terrones, M. *http://www.ch.ic.ac.uk/motm/spiral.html.* Sussex University.

[112] Iijima, S., C. Brabec, A. Maiti, and J. Bernholc. 1996. Structural flexibility of carbon nanotubes. *J. Chem. Phys.* 104:2089–2092.

[113] Minot, E. D., Y. Yaish, V. Sazonova, J.-Y. Park, M. Brink, and P. L. McEuen. 2003. Tuning carbon nanotube band gaps with strain. *Phy. Rev. Lett.* 90:156401–(1–4).

[114] Dresselhaus, M. S., G. Dresselhaus, and P. C. Ecklund. 1996. *Science of fullerenes and carbon nanotubes.* Academic Press, San Diego.

[115] Kolmogorov, A. N. and V. H. Crespi. 2000. Smoothest bearings: Interlayer sliding in multiwalled carbon nanotubes. *Phy. Rev. Lett.* 85:4727–4730.

[116] Legoas, S. B., V. R. Coluci, S. F. Braga, P. Z. Coura, S. O. Dantas, and D. S. Galvão. 2003. Molecular-dynamics simulations of carbon nanotubes as gigahertz oscillators. *Phy. Rev. Lett.* 90:055504–(1–4).

[117] Zheng, Q. and Q. Jiang. 2002. Multiwalled carbon nanotubes as gigahertz oscillators. *Phy. Rev. Lett.* 88:045503–(1–3).

[118] Zheng, Q., J. Z. Liu, and Q. Jiang. 2002. Excess van der Waals interaction energy of a multiwalled carbon nanotube with an extruded core and the induced core oscillation. *Phys. Rev. B.* 65:245409–(1–6).

[119] Guo, W., Y. Guo, H. Gao, Q. Zheng, and W. Zhong. 2003. Energy dissipation in gigahertz oscillators from multiwalled carbon nanotubes. *Phy. Rev. Lett.* 91:125501–(1–4).

[120] Akita, S. and Y. Nakayama. 2003. Interlayer sliding force of individual multiwall carbon nanotubes. *Jpn. J. Appl. Phys.* 42:4830–4833.

[121] Cummings, J. and A. Zettl. 2000. Low-friction nanoscale linear bearing realized from multiwall carbon nanotubes. *Science.* 289:602–604.

[122] Yu, M. F., B. I. Yakobson, and R. S. Ruoff. 2000. Controlled sliding and pullout of nested shells in individual multiwalled carbon nanotubes. *J. Phys. Chem. B.* 104:8764–8767.

[123] Dresselhaus, M. S., G. Dresselhaus, and P. Avouris. 2001. *Carbon nanotubes, synthesis, structure, properties and applicaions.* Springer , Berlin.

[124] Fennimore, A. M., T. D. Yuzvinsky, W. Q. Han, M. S. Fuhrer, J. Cumings, and A. Zettl. 2003. Rotational actuators based on carbon nanotubes. *Nature.* 424:408–410.

[125] Zhang, G., X. Jiang, and E. Wang. 2003. Tubular graphite cones. *Science.* 300:472–474.

[126] McClure, J. W. 1964. Energy band structure of graphite. *IBM Journal of Research and Development.* 8:255–261.

[127] Kittel, C. 1986. *Introduction to solid state physics.* John Wiley & Sons Inc.

[128] Zhou, C., J. Kong, and H. Dai. 2000. Electrical measurements of individual semiconducting single-walled carbon nanotubes of various diameters. *Appl. Phy. Lett.* 76:1597–1599.

[129] Gong, Q.-M., Z. Li, Y. Wang, B. Wu, Z. Zhang, and J. Liang. 2007. The effect of high-temperature annealing on the structure and electrical properties of well- aligned carbon nanotubes. *Mat. Res. Bull.* 42:474–481.

[130] Song, W., M. Ni, J. Lu, Z. Gao, S. Nagase, D. Yu, H. Ye, and X. Zhang. 2005. Electronic structures of semiconducting double-walled carbon nanotubes: Important effect of interlay interaction. *Chem. Phys. Lett.* 414:429–433.

[131] Dai, H., E. W. Wong, and C. M. Lieber. 1996. Probing electrical transport in nanomaterials: Conductivity of individual carbon nanotubes. *Science.* 272:523–526.

[132] Ebbesen, T. W., H. J. Lezec, H. Hiura, J. W. Bennett, H. F. Ghaemi, and T. Thio. 1996. Electrical conductivity of individual carbon nanotubes. *Nature.* 382:54–56.

[133] Langer, L., V. Bayot, E. Grivei, J.-P. Issi, J. P. Heremans, C. H. Olk, L. Stockman, C. V. Haesendonck, and Y. Bruynseraede. 1996. Quantum transport in multiwalled carbon nanotube. *Phys. Rev. Lett.* 76:479–482.

[134] Benedict, L. X., V. H. Crespi, S. G. Louie, and M. L. Cohen. 1995. Static conductivity and superconductivity of carbon nanotubes: Relations between tubes and sheets. *Phys. Rev. B.* 52:14935–14940.

[135] Baierle, R. J., S. B. Fagan, R. Mota, A. J. R. da Silva, and A. Fazzio. 2001. Electronic and structural properties of silicon-doped carbon nanotubes. *Phys. Rev. B.* 64:085413–(1–4).

[136] Wei, B., R. Spolenak, P. Kohler-Redlich, M. Rühle, and E. Arzt. 1999. Electrical transport in pure and boron-doped carbon nanotubes. *Appl. Phys. Lett.* 74:3149–3151.

[137] Ayala, P., F. L. Freire Jr., L. Gu, D. J. Smith, I. G. Solórzano, D. W. Macedo, J. B. V. Sande, H. Terrones, J. Rodriguez-Manzo, and M. Terrones. 2006. Decorating carbon nanotubes with nanostructured nickel particles via chemical methods. *Chem. Phys. Lett.* 431:104–109.

[138] Rana, R. K., X. N. Xu, Y. Yeshurun, and A. Gedanken. 2002. Preparation, texture and magnetic properties of carbon nanotubes/nanoparticles doped with cobalt. *J. Phys. Chem. B.* 106:4079–4084.

[139] Wu, X., Y. Tao, C. Mao, L. Wen, and J. Zhu. 2007. Synthesis of nitrogen-doped horn shaped carbon nanotubes by reduction of pentachloropyridine with metallic sodium. *Carbon.* 45:2253–2259.

[140] Saito, R., M. Fujita, G. Dresselhaus, and M. S. Dresselhaus. 1992. Electronic structure of chiral graphene tubules. *Appl. Phys. Lett.* 60:2204–2206.

[141] Hamada, N., S. Sawada, and A. Oshiyama. 1992. New one-dimensional conductors: Graphitic microtubules. *Phy. Rev. Lett.* 68:1579–1581.

[142] Li, Z. M., Z. K. Tang, H. J. Liu, N. Wang, C. T. Chan, R. Saito, S. Okada, G. D. Li, J. S. Chen, N. Nagasawa, and S. Tsuda. 2001. Polarized absorption spectra of single-walled 4 Å carbon nanotubes aligned in channels of an $AlPO_4$-5 single crystal. *Phy. Rev. Lett.* 87:127401–(1–4).

[143] Tanaka, K., K. Okahara, M. Okada, and T. Yamabe. 1992. Electronic properties of bucky-tube model. *Chem. Phys. Lett.* 191:469–472.

[144] Wildöer, J. W. G., L. C. Venema, A. G. Rinzler, R. E. Smalley, and C. Dekker. 1998. Electronic structure of atomically resolved carbon nanotubes. *Nature.* 391:59–62.

[145] Lee, C. H., Y. H. Ho, R. B. Chen, T. S. Li, and M. F. Lin. 2007. Electronic structures of finite doulbe-walled carbon nanotubes. *Phys. Stat. Sol. (C).* 4:509–511.

[146] Berber, S., Y.-K. Kwon, and D. Tománek. 2000. Unusually high thermal conductivity of carbon nanotubes. *Phy. Rev. Lett.* 84:4613–4616.

[147] Hone, J., M. Whitney, C. Piskoti, and A. Zettl. 1999. Thermal conductivity of single-walled carbon nanotubes. *Phys. Rev. B.* 59:R2514–2516.

[148] Che, J., T. Çağin, and W. A. Goddard-lll. 2000. Thermal conductivity of carbon nanotbes. *Nanotechnology.* 11:65–69.

[149] Huhtala, M., A. V. Krasheninnikov, J. Aittoniemi, S. J. Stuart, K. Nordlund, and K. Kaski. 2004. Improved mechanical load transfer between shells of multi-walled carbon nanotubes. *Phys. Rev. B.* 70:045404–(1–8).

[150] Sammalkorpi, M., A. V. Krasheninnikov, A. Kuronen, K. NOrdlund, and K. Kaski. 2005. Irradiation-induced stiffening of carbon nanotube bundles. *Nucl. Instr. Meth. Phys. B.* 228:142–145.

[151] Maiti, A., A. Svizhenko, and M. P. Anantram. 2002. Electronic transport through carbon nanotubes: Effects of structural deformation and tube chirality. *Phy. Rev. Lett.* 88:126805–(1–4).

[152] Orlikowsi, D., M. B. Nardelli, J. Bernholc, and C. Roland. 2000. Theoretical STM signatures and transport properties of native defects in carbon nanotubes. *Phys. Rev. B.* 61:14194–14203.

[153] Bockrath, M., W. Liang, D. Bozovic, J. H. Hafner, C. M. Lieber, M. Tinkham, and H. Park. 2001. Resonant electron scattering by defects in single-walled carbon nanotubes. *Science.* 291:283–285.

[154] Crespi, V. H. *http://www.phys.psu.edu/ crespi/images/junction-80:71.gif.* Pen State University.

[155] Ishibashi, K., D. Tsuya, M. Suzuki, and Y. Aoyagi. 2003. Fabrication of a single-electron inverter in multiwall carbon nanotubes. *Appl. Phy. Lett.* 82:3307–3309.

[156] Bozovic, D., M. Bockrath, J. H. Hafner, C. M. Lieber, H. Park, and M. Tinkham. 2001. Electronic properties of mechanically induced kinks in single-walled carbon nanotubes. *Appl. Phy. Lett.* 78:3693–3695.

[157] Postma, H. W., T. Teepen, Z. Yao, M. Grifoni, and C. Dekker. 2001. Carbon nanotube single-electron transistors at room temperature. *Science.* 293:76–79.

[158] Tersoff, J. 1988. New empirical approach for the structure and energy of covalent systems. *Phys. Rev. B.* 37:6991–7000.

[159] Brenner, D. W. 1990. Empirical potential for hydrocarbons for use in simulating the chemical vapor deposition of diamond films. *Phys. Rev. B.* 42:9458–9471.

[160] Ascroft, N. W. and N. D. Mermin. 1976. *Solid state physics.* Saunders, USA.

[161] Hohenberg, P. and W. Kohn. 1964. Inhomogeneous electron gas. *Phys. Rev.* 136:B864–B871.

[162] Kohn, W. and L. J. Sham. 1965. Self-consistent equations including exchange and correlation effects. *Phys. Rev.* 140:A1133–A1138.

[163] Cramer, C. J. 2002. *Essentials of computational chemistry.* John Wiley & Sons, Inc., USA.

[164] Goringe, C. M., D. R. Bowler, and E. Hernández. 1997. Tight-binding modelling of materials. *Rep. Prog. Phys.* 60:1447–1512.

[165] Rapaport, D. C. 1995. *The art of molecular dynamics simulation.* Cambridge University Press, UK.

[166] Allen, M. P. and D. J. Tildesley. 1987. *Computer simulation of liquids.* Clarendon, UK.

[167] Tersoff, J. 1986. New empirical model for the structural properties of silicon. *Phy. Rev. Lett.* 56:632–635.

[168] Tersoff, J. 1989. Modeling solid-state chemistry: Interatomic potentials for multicomponent systems. *Phys. Rev. B.* 39:5566–5568.

[169] Stuart, S. J., A. B. Tutein, and J. A. Harrison. 2000. A reactive potential for hydrocarbons with intermolecular interactions. *J. Chem. Phys.* 112:6472–6486.

[170] Allen, M. P. and D. J. Tildesley. 1987. *Computer simulation of liquids.* Oxford.

[171] Haile, J. M. 1992. *Molecular dynamics simulation.* Wiley.

[172] Verlet, L. 1967. Computer "experiments" on classical fluids. i. thermodynamical properties of lennard-jones molecules. *Phys. Rev.* 159:98–103.

[173] Verlet, L. 1968. Computer "experiments" on classical fluids. ii. equilibrium correlation functions. *Phys. Rev.* 165:201–214.

[174] Rahman, A. 1964. Correlations in the motion of atoms in liquid argon. *Phys. Rev.* 136:A405–A411.

[175] Abell, G. C. 1985. Empirical chemical pseudopotential theory of molecular and metallic bonding. *Phys. Rev. B.* 31:6184–6196.

[176] Rose, J. H., J. R. Smith, and J. Ferrante. 1983. Universal features of bonding in metals. *Phys. Rev. B.* 28:1835–1845.

[177] Tersoff, J. 1988. Empirical interatomic potential for carbon, with applications to amorphous carbon. *Phys. Rev. Lett.* 61:2879–2882.

[178] Shen, H. 2006. The compressive mechanical properties of C-60 and endohedral M@C60(M=Si, Ge) fullerene molecules. *Mat. Lett.* 60:2050–2054.

[179] Chancey, R. T., L. Oddershede, F. E. Harris, and J. R. Sabin. 2003. Fragmentation of fullerenes. *Phys. Rev. A.* 67:043203–(1–7).

[180] Marcos, P. A., J. A. Alonso, A. Rubio, and M. J. López. 1999. Simulating the thermal stability and phase changes of small carbon clusters and fullerenes. *Eur. Phys. J. D.* 6:221–233.

[181] López, M. J., I. Cabria, N. H. March, and J. A. Alonso. 2005. Structural and thermal stability of narrow and short carbon nanotubes and nanostrips. *Carbon.* 43:1371–1377.

[182] Ş. Erkoç and S. Özkaymak. 1998. Energetics of carbon nanotubes. *Eur. Phys. J. D.* 4:331–333.

[183] López, M. J., A. Rubio, J. A. Alonso, L.-C. Quin, and S. Iijima. 2001. Novel polygonized single-wall carbon nanotube bundles. *Phys. Rev. Lett.* 86:3056–3059.

[184] Rayleigh, L. L. 1882. On the equilibrium of liquid conducting masses charged with electricity. *Philo. Mag.* 14:184–186.

[185] Bohr, N. and J. A. Wheeler. 1939. The mechanism of nuclear fission. *Phys. Rev.* 56:426–450.

[186] Meitner, L. and O. R. Frisch. 1939. Disintegration of uranium by neutrons: A new type of nuclear reaction. *Nature.* 143:239–240.

[187] Last, I., Y. Levy, and J. Jortner. 2002. Beyond the Rayleigh instability limit for multicharged finite systems: From fission to coulomb explosion. *Proc. Nat. Acad. Sci.* 99:9107–9112.

[188] Solov'yov, I. A., A. V. Solov'yov, and W. Greiner. 2004. Fusion process of Lennard-Jones clusters: global minima and magic numbers formation. *Int. J. Mod. Phys. E.* 13:697–736.

[189] Solov'yov, I. A., A. V. Solov'yov, W. Greiner, A. Koshelev, and A. Shutovich. 2003. Cluster growing process and a sequence of magic numbers. *Phys. Rev. Lett.* 90:053401–(1–4).

[190] Semenikhina, V., A. Lyalin, A. Solov'yov, and W. Greiner. 2008. Droplet model of an atomic cluster at a solid surface. *Jour. Exp. Theor. Phys.* 106:678–689.

[191] Poenaru, D., R. Gherghescu, I. Plonski, A. Solov'yov, and W. Greiner. 2008. Macroscopic-microscopic theory of semi-spheroidal atomic cluster. *Eur. Phys. J. D.* 47:379–393.

[192] Poenaru, D., R. Georgescu, A. Solov'yov, and W. Greiner. 2007. Liquid-drop stability of a superdeformed prolate semi-spheroidal atomic cluster. *Europhys. Lett.* 79:63001–(1–5).

[193] Beiser, A. 1987. *Concepts of modern physics.* McGraw-Hill, Inc. New York.

[194] Jiang, H., P. Zhang, B. Liu, Y. Huang, P. H. Geubelle, H. Gao, and K. C. Hwang. 2003. The effect of nanotube radius on the constitutive model for carbon nanotubes. *Comp. Mat. Sci.* 28:429–442.

[195] Sun, X. and W. Zhao. 2005. Prediction of stiffness and strength of single-walled carbon nanotubes by molecular-mechanics based finite element approach. *Mat. Sci. Eng. A.* 390:366–371.

[196] Kanamitsu, K. and S. Saito. 2002. Geometries, electronic properties and energetics of isolated single walled carbon nanotubes. *Jour. Phys. Soc. Japan.* 71:483–486.

[197] Budyka, M. F., T. S. Zyubina, A. G. Ryabenko, S. H. Lin, and A. M. Mebel. 2005. Bond lengths and diameters of armchair single wall carbon nanotubes. *Chem. Phys. Lett.* 407:266–271.

[198] Solov'yov, I., O. Obolensky, V. Semenikhina, A. Yakubovich, A. Lyalin, and A. Solov'yov. 2008. *Explorer 1.0.0.* MBNS Group at FIAS, Frankfurt am Main.

[199] Gale, J. D. 1997. GULP - a computer program for the symmetry adapted simulation of solids. *JCS Faraday Trans.* 93:629–638.

[200] Hussien, A., A. Yakubovich, A. Solov'yov, and W. Greiner. Phase transitions in fullerenes: Fragmentation and reassembly of the carbon cage. *e-print arXiv:0807.4435v1.*

[201] Foresman, J. B. and A. Frisch. 1996. *Exploring Chemistry with Electronic Structure Methods.* Gaussian, Inc., Pittsburgh, PA.

[202] Fowler, P. W. and D. E. Manolopoulos. 2007. *An atlas of fullerenes.* Dover, New York.

[203] Pal, S. K., S. Talapatra, S. Kar, L. Ci, R. Vajtai, T. Borca-Tasciuc, L. Schadler, and P. Ajayan. 2008. Time and temperature dependence of multi-walled carbon nanotube growth on inconel 600. *Nanotechnology.* 19:045610–(1–5).

[204] Lee, C. J., J. Park, J. M. Kim, Y. Huh, J. Y. Lee, and K. S. No. 2000. Low-temperature growth of carbon nanotubes by thermal chemical vapor deposition using Pd, Cr, and Pt as co-catalyst. *Chem. Phys. Lett.* 327:277–283.

[205] Zhang, P., Y. Huang, P. H. Geubelle, P. A. Klein, and K. C. Hwang. 2002. The elastic modulus of single-wall carbon nanotubes: a continuum analysis incorporating interatomic potentials. *Int. J. Sol. Struct.* 39:3893–3906.

[206] Che, J., T. Çağin, and W. A. Goddard-lll. 1999. Studies of fullerenes and carbon nanotubes by an extended bond order potential. *Nanotechnology.* 10:263–268.

[207] Gupta, S., K. Dharamvir, and V. K. Jindal. 2005. Elastic moduli of single-walled carbon nanotubes and their ropes. *Phys. Rev. B.* 72:165428–(1–16).

[208] Tibbetts, G. G. 1984. Why are carbon filaments tubular ? *J. Cryst. Growth.* 66:632–638.

[209] Gülseren, O., T. Yildirim, and S. Ciraci. 2002. Systematic *ab initio* study of curvature effects in carbon nanotubes. *Phys. Rev. B.* 65:153405–(1–4).

[210] Xin, Z., Z. Jianjun, and O.-Y. Zhong-can. 2000. Strain energy and Youngs modulus of single-wall carbon nanotubes calculated from electronic energy-band theory. *Phys. Rev. B.* 62:13692–13696.

[211] Sánchez-Portal, D., E. Artacho, J. M. Soler, A. Rubio, and P. Ordejón. 1999. *Ab initio* structural, elastic, and vibrational properties of carbon nanotubes. *Phys. Rev. B.* 59:12678–12688.

[212] Tersoff, J. 1992. Energies of fullerenes. *Phys. Rev. B.* 46:15546–15549.

[213] Li, L., S. Reich, and J. Robertson. 2006. Modelling the nucleation and chirality selection of carbon nanotubes. *J. Nanosci. Nanotechnol.* 6:1290–1297.

[214] Kudin, K. N., G. E. Scuseria, and B. I. Yakobson. 2001. C_2F, BN, and C nanoshell elasticity from ab initio computations. *Phys. Rev. B.* 64:235406–(1–10).

[215] Nicklow, R., N. Wakabayashi, and H. G. Smith. 1972. Lattice dynamics of pyrolytic graphite. *Phys. Rev. B.* 5:4951–4962.

[216] Zhong-can, O.-Y., Z.-B. Su, and C.-L. Wang. 1997. Coil formation in multishell carbon nanotubes: competition between curvature elasticity and interlayer adhesion. *Phy. Rev. Lett.* 78:4055–4058.

[217] Reddy, C., S. Rajendran, and K. M. Liew. 2006. Equilibrium configuration and continuum elastic properties of finite sized graphene. *Nanotechnology.* 17:864–870.

[218] Wang, L., Q. Zheng, J. Z. Liu, and Q. Jiang. 2005. Size dependence of the thin-shell model for carbon nanotubes. *Phy. Rev. Lett.* 95:105501–(1–4).

[219] Lier, G. V., C. V. Alsenoy, V. V. Doren, and P. Geerlings. 2000. *Ab initio* study of the elastic properties of single-walled carbon nanotubes and graphene. *Chem. Phys. Lett.* 326:181–185.

[220] Lo, S., A. Korol, and A. Solov'yov. 2007. Dynamical screening of an atom confined within a finite-width fullerene. *J. Phys. B.* 40:3973–3981.

[221] Rüdel, A., R. Hentges, U. Becker, H. S. Chakraborty, M. E. Madjet, and J. M. Rost. 2002. Imaging delocalized electron clouds: Photoionization of C_{60} in fourier reciprocal space. *Phy. Rev. Lett.* 89:125503–(1–4).

[222] Hofmann, S., G. Csányi, A. C. Ferrari, M. C. Payne, and J. Robertson. 2005. Surface diffusion: The low activation energy path for nanotube growth. *Phy. Rev. Lett.* 95:036101–(1–4).

[223] Louchev, O. A., Y. Sato, and H. Kanda. 2002. Morphological stabilization, destabilization, and open-end closure during carbon nanotube growth mediated by surface diffusion. *Phys. Rev. E.* 66:011601–(1–17).

[224] Zheng, B., C. Lu, G. Gu, A. Makarovski, G. Finkelstein, and J. Liu. 2002. Efficient CVD growth of single-walled carbon nanotubes on surfaces using carbon monoxide precursor. *Nano Lett.* 2:895–898.

[225] Dobkin, D. and M. Zuraw. 2003. *Principles of chemical vapor deposition*. Springer , Newyork.

[226] Shibuta, Y. and S. Maruyama. 2007. Bond-order potential for transition metal carbide cluster for the growth simulation of a single-walled carbon nanotube. *Comput. Mater. Sci.* 39:842–848.

[227] Lin, Z. C., J. C. Huang, and Y. R. Jeng. 2007. 3d nano-scale cutting model for nickel material. *J. Mater. Process. Technol.* 192-193:27–36.

[228] Xiao, Y., Z. M. Li, X. H. Yan, Y. Zhang, Y. L. Mao, and Y. R. Yang. 2005. Curvature effect on the radial breathing modes of single-walled carbon nanotubes. *Phys. Rev. B.* 71:233405–(1–4).